Title
High-Resolution Velocity Fields of Low-Mass Disk Galaxies

Author
Truong, Phuongmai

Publication Date
2017

Peer reviewed|Thesis/dissertation

High-Resolution Velocity Fields of Low-Mass Disk Galaxies

By

Phuongmai N. Truong

A dissertation submitted in partial satisfaction of the

requirements for the degree of

Doctor of Philosophy

in

Physics

in the

Graduate Division

of the

University of California, Berkeley

Committee in charge:

Professor Leo Blitz, Co-chair
Professor Adrian Lee, Co-chair
Professor Chung-Pei Ma
Professor Bernard Sadoulet

Spring 2017

High-Resolution Velocity Fields of Low-Mass Disk Galaxies

Abstract

High-Resolution Velocity Fields of Low-Mass Disk Galaxies

by

Phuongmai N. Truong

Doctor of Philosophy in Physics

University of California, Berkeley

Professor Leo Blitz, Co-chair

Professor Adrian Lee, Co-chair

This study aims to examine the relative distributions of dark and baryonic matter as a function of star formation history in a representative sample of low mass disk galaxies. In this study, we present the high-resolution ^{12}CO(J=1 $\rightarrow$ 0) interferometry for a sample of 26 nearby dwarf galaxies, which were obtained from the Combined Array for Research in Millimeter-wave Astronomy (CARMA). Among these 26 galaxies, 14 have good CO detections, including 6 galaxies previously detected in single-dish CO measurements and 8 newly detected ones. We find a linear correlation between the CO flux and the mid- and far-IR flux from the WISE and IRAS catalogs. Compared to the far-IR flux, the mid-IR flux may be a better indication of whether a galaxy contains sufficient CO for detection at the level of instrument sensitivity of CARMA. This correlation might prove to be useful in future studies to help choosing other CO targets for observation. The median molecular mass (including helium and H_2) of our galaxies is $2.8 \times 10^8 M_\odot$, which is consistent with past observations for dwarf galaxies. The molecular content is weakly correlated with the dynamical mass, r-band luminosity and size of the galaxies. The median ratios of molecular mass vs. dynamical mass and molecular mass vs. r-band luminosity are $M_{mol}/M_{dyn} \approx 0.035$ and $M_{mol}/L_r \approx 0.078 M_\odot/L_{r,\odot}$, respectively, which are also consistent with past observations for dwarf galaxies. In addition, we present the rotation curves of these 14 galaxies. To examine the dark matter distribution in their central regions, the reduced CO data were fitted with simple kinematic models using two different algorithms. For all 14 galaxies, despite inhomogeneous distribution of molecular gas in some of the sources, robust kinematic results were obtained for all sources. Most galaxies show approximately zero or small noncircular motions, particularly the ones with smooth spatial distributions of CO emission. Furthermore, consistent rotation curves are obtained using both algorithms. In general, the CO rotation curves are consistent with Hα rotation curves of the same galaxies. Using the CO rotation curves, along with information on the stellar distribution from optical and infrared imaging,

we model the velocity data including contributions from stars and the dark matter halo, which we parameterized using a generalized Navarro, Frenk & White profile. The results show that the inner power-law slope α of the density profile varies over a large range from below 0.38 (cored) to 1.76 (cuspy), with a mean value of 0.58 ± 0.45 (mean $\pm$ scatter) or 0.64 ± 0.49 if we assume the stellar distribution derived from r-band data or IRAC 4.5-micron data, respectively. The density profile slope is generally robust as the baryonic M/L is varied from minimum- to maximum-disk estimates. Our galaxies show low stellar mass-to-light ratios: $M_*/L = 0.10 \pm 0.02$ for IRAC channel-2 data and 0.49 ± 0.33 for r-band data. Considering our results in combination with recent studies from the literature, we find weak correlations between the dark matter profile inner slope, dynamical mass and distance of the galaxies, where more distant and more massive galaxies have steeper slopes. In addition, we find no statistically significant correlation between the slope and the stellar mass, which may suggest that baryonic feedback models alone cannot fully explain the flattening behavior of the inner profiles of dwarf galaxies.

To Mom and Dad.

Contents

List of Figures **iv**

List of Tables **x**

Acknowledgments **xi**

1 Introduction **1**
1.1 Science background . . . 1
1.2 Goal of our study . . . 2

2 Overview of dark-matter studies related to the core-cusp problem **5**
2.1 The presence of dark matter . . . 5
2.2 Simulations versus observations . . . 7

3 CO Data **13**
3.1 Target Selection . . . 13
3.2 Observations . . . 16
3.3 Data Reduction . . . 16
3.4 Results & Discussion . . . 20
3.4.1 Flux comparison . . . 23
3.4.2 Molecular gas content . . . 24

4 Data Analysis, CO Rotation Curves and Mass Modeling **34**
4.1 Data Analysis . . . 34
4.1.1 Fitting models . . . 35
4.1.2 DiskFit settings . . . 35
4.1.3 DiskFit vs. RingFit . . . 40
4.2 Rotation Curve Fitting Results . . . 42
4.3 Mass modeling . . . 53
4.4 Mass Modeling Results . . . 55
4.4.1 Average values and range of the parameters in our sample and comparison with literature values . . . 56
4.4.2 Dependence of the density profile slope on other parameters . . . 57

4.4.3 Further discussion on some specific galaxies and their effects on the robustness of the results . . . 59
4.5 Discussion . . . 60

5 Addition data from ALMA and preliminary results **69**
5.1 Data and rotation curves . . . 69
5.2 Preliminary mass modeling results and discussion . . . 70

6 Summary and Conclusions **80**

Bibliography **83**

List of Figures

2.1 Rotational velocities for 7 galaxies as a function of the distance from the nucleus. The curves were smoothed to remove velocity undulations across the arms and small differences between the major-axis velocities on each side of the nucleus. Early-type galaxies consistently have higher peaks than late-type ones. Figure and caption from Rubin, V. C. et al. (1978). 6

2.2 Left: Image and combined CO/Ha rotation curve extracted from 2-D velocity fields of NGC 2976 a nearby (d = 3.6 Mpc) dwarf disk galaxy from Simon et al. (2003). Right: The dynamics imply a DM density slope of $r \propto r^{-0.01}$ (shaded region indicates the 1σ uncertainty), which is much flatter than the canonical slope $r \propto r^{-1}$ expected for the cosmologically motivated CDM profile. Understanding the origin of the shallow DM density slopes and quantifying any correlation with the host galaxy properties is the primary goal of our study. 8

2.3 Current status of the dark-matter density slope in dwarf galaxies from high-resolution data (shaded; Simon, J.D. et al. (2005), Oh, S.-H. et al. (2011)). Most measurements indicate shallower slopes than an NFW profile ($\alpha = 1$) but a few are consistent with the cuspy profiles. We aim to better quantify this scatter with a significantly larger sample and search for its physical origin by correlating α with the host galaxy properties. For comparison, we overplot the DM slopes for brightest cluster galaxies by Newman, A. B. et al. (2013b) and Newman, A. B. et al. (2013a). These studies also indicate DM slopes with $\alpha < 1$. 9

2.4 The slope of the DM density profile α versus stellar mass for the halos in the simulations of Governato, F. et al. (2012) (left) and Chan, T. K. et al. (2015) (right). In the left panel, the slopes of the simulated galaxies were measured at $r = 0.5$ kpc and $z = 0$; the solid "DM-only" line is the slope predicted for the same CDM cosmological model assuming (i) the NFW concentration parameter trend of Macció et al. (2007) and (ii) the measured relation of stellar mass versus halo mass in the simulations to convert from halo masses. Large crosses: haloes resolved with more than 0.5×10^6 DM particles within the virial radius. Small crosses: more than 5×10^4 DM particles. The small squares represent 22 observational data points measured from galaxies from the THINGS and LITTLE THINGS surveys. In the right panel, the slopes of the simulated galaxies were measured at $r = 0.3 - 0.7$ kpc and $z = 0$. Images from Governato, F. et al. (2012) and Chan, T. K. et al. (2015). 11

3.1 Summary of various properties of the galaxies targeted with CARMA in our survey: (a) distance (measured in Mpc); (b) rotational velocity (km s^{-1}); (c) linear diameter (kpc), using the distances from (a) and major diameters (arcmin) from NED; (d) $\log_{10}$ of the dynamical mass ($M_\odot$), $M_{dyn} = v_{rot}^2 R/GM_\odot$, with v_{rot} from (b); (e) absolute blue magnitude; (f) WISE w4 mid-infrared magnitude. The black dotted lines in (d) and (e) indicate the appoximate values for the Milky Way. 18

3.2 Naturally weighted CO(1-0) intensity and velocity distribution maps without masking of the CO-detected dwarf galaxies in the sample. The color bars indicate the velocity in km s^{-1} (gradient in the horizontal direction) and flux level in Jy (gradient in the vertical direction). 27

3.3 Naturally weighted CO(1-0) intensity and velocity distribution maps with masking to enhance the SNR. For all galaxies, the RA offset is from +30" (left) to -30" (right), the Dec offset is from -30" (bottom) to +30" (top); except for NGC 1012 and NGC 4150, whose RA and Dec offsets are from +20" to -20" and -20" to +20", respectively. The color bar on the right side of each image shows the velocity gradient; the number at the top corner is the systemic velocity. 28

3.4 Contours of CO(1-0) intensity (CARMA data) on r-band imaging data, which were taken with SPICAM on the ARC 3.5m telescope at Apache Point Observatory. Exceptions: the r-band images of NGC 4150 and NGC4310 were obtained from the SDSS III archive. 29

3.5 Spectra of detected galaxies from the survey at the central pixel in the image. The horizontal dashed lines indicate the rms noise; the vertical lines show the positions of the LSR (dashed), radio (solid), optical (dotted), and CO-data-based systemic velocities (dash-dot). The LSR, radio and optical velcities were obtained from NED and hyperLEDA. The shaded region shows the HI line width W_{20}. Note that NGC 853 has a hole in the center, hence the lack of a signal at the central pixel, and NGC 4150 has a broad linewidth that covers the entire velocity bandwidth and leaves no baseline, which may be due to it being an elliptical galaxy instead of a thin disk. 31
3.6 Correlation between the total CO flux of each target (or 3σ upper limit in the case of non-detection) and its corresponding $F_{100\mu m}$ and WISE w4 flux density $F_{22\mu m}$. $F_{100\mu m}$ was obtained from NED, and $F_{22\mu m}$ was converted from the Vega magnitude in band 4, which was obtained from the WISE All-Sky source catalog. 32
3.7 Correlations between the molecular mass, radius, and dynamical mass (top) and r-band luminosity (bottom) of the targets in the survey. The CO-detected targets are shown with filled circles, and the CO non-detections are shown with empty dashed circles. For the CO non-detections, the molecular mass was calculated from the 3σ upper limit (Table 3.2). The dynamical mass was calculated from the HI-derived rotational velocity; the r-band luminosity was obtained from r-band imaging at Apache Point Observatory (Relatores et al., in preparation). The size of the bubbles corresponds to the radius in kpc, whose value is the number shown next to the bubble. To avoid over-cluttering the image, we do not show the numerical values of the radii of the non-detections, which can be found in Table 1. 33

4.1 Rotation curves and residuals from the CO data of NGC 1035 and NGC 6106 using DiskFit in 3 cases: $m = 0$ with no radial flow (black crosses connected by a black dashed line); $m = 0$ with radial flow (cyan; tangential velocity [circles] and radial velocity [triangles]); $m = 1$, i.e., lop-sided model (red; tangential velocity [circles] and radial velocity [triangles]). The error bars were computed using 100 bootstrap resamplings. 36
4.2 Rotation curves from CO data of NGC 1035 and NGC 6106 using DiskFit with three different ring widths: $\delta r = 1.5$ arcsec (black), 3 arcsec (cyan), and 4 arcsec (red). The model is $m = 0$ with radial flow. 38
4.3 Comparison between DiskFit (cyan) and RingFit (black) results of the rotation curves of 4 galaxies, including circular velocity (triangles) and radial velocity (circles). The error bars were estimated using bootstrap (DiskFit) and Monte Carlo (RingFit) resamplings. 40

4.4 Comparison between the geometric parameters derived from the CO data and those from photometric measurements (APO r-band data or IRAC channel-2 data) for the galaxies with CO detections. The parameters from the CO data were obtained from the rotation curve fitting using DiskFit, with either all fitting inputs from CO data (circle) or photometric centers as the inputs for the centers (triangle). The straight black line is the best fit line to show the correlation between photometric parameters and CO parameters; the dashed lines indicate the 1σ standard deviation from the best fit line. The bottom right plot shows the centers of the galaxies relative to the center pixel (0, 0) of their CO images; the CO centers (black) were obtained from DiskFit, and the photometric centers (red) were converted from the RA and Dec values obtained in APO r-band data or IRAC channel-2 data. The circles indicate the radii of 1 and 2 arcsec, where most of the galaxy centers are with respect to the centers of their CO images. . 47

4.5 Rotation curves of the galaxies in the survey as fitted by DiskFit. Left column: the corresponding (unmasked) moment-1 maps with overlaid rings, whose centers, PA and ellipticity were obtained from DiskFit results. The x and y coordinates of the maps are measured in pixels, corresponding to a coverage of $30'' \times 30''$; the color bars indicate the systemic velocity (km/s). The triangles and circles indicate the tangential and radial velocity components, respectively. The blue dotted line shows the Hα rotation curves (also obtained using DiskFit; the PA, ellipticity and center were also fixed for NGC 853). The black lines show the CO rotation curves with all CO data input (dot-dashed) and CO rotation curves with photometric center for the input (solid). Both NGC 853 and NGC 4150 were fitted using the $m = 0$ model with no radial flow; the input PA, ellipticity and center were fixed for NGC 853, whereas the input PA and ellipticity were fixed for NGC 4150. For NGC 1012 and NGC 5303, the center was fixed. All other galaxies were fit with the $m = 0$ radial-flow model and no fixed parameters 48

4.6 Example of gNFW fitting to CO data. The total rotation curve (magenta), which is fitted to the CO data (cyan) is the sum of two mass components in the gNFW model: stellar mass (green) and dark matter (blue). "Fix all", "Fix center", "Fix PA_and_eps" and "Fix none" indicate the fixed geometric parameters in the initialization of the fit to obtain the rotation curves; "Fix all" indicates that the PA, ellipticity (i.e., "eps") and center were fixed. The parameter constraints and covariances of the model were generated using the Markov Chain Monte Carlo (MCMC) method with the python-based software *emcee* (Foreman-Mackey, D. et al. (2013)), 100 walkers and 5000 steps. Five generated sets of parameters were randomly selected after the walkers began converging to plot the curves as shown. 63

4.7 Histogram of the posterior distributions of the dark-matter inner profile slope α of the galaxies, whose only the 95% confidence level upper limit values are obtained (see Table 4.3). 65

4.8 Comparison of the gNFW parameters for mass models constructed using different bands to trace the stellar component. The gNFW parameters are the virial mass ($\log M_{200}$), concentration (c_{200}), stellar mass-to-light ratio (M_*/L), density parameter ($\log \rho_0$), scale radius (r_s) and inner slope (α). The modeling is based on the CO kinematics with the stellar mass assumed to be proportional to the luminosity in either r-band data (horizontal axis) or IRAC channel-2 (denoted "Ch2") data (vertical axis). The parameters were fit for 3 models: minimum disk (black circles), maximum disk (cyan circles), and variable disk (red squares). The arrows indicate the upper and lower limits (the length of the arrow is only for visual purpose and is not related to any physical quantity). The plots show that all parameters except M_*/L are robust with respect to the choice of r-band or Ch2 data. 66

4.9 Values of the inner power-law slope α (top) and stellar mass-to-light ratios (bottom) of each galaxy in the sample for three fitting cases to the gNFW function: minimum disk (cross), variable disk (circle), and maximum disk (square). The parameters were obtained using either r-band data (black markers) or IRAC channel-2 ("Ch2") data (red markers) for the stellar mass. The arrows indicate the upper and lower limits (the length of the arrow is only for visual purpose and is not related to any physical quantity). 67

4.10 Correlations of the inner power-law slope α versus the virial mass, stellar mass-to-light ratios, dynamical mass, and distance of the galaxies in the sample. The survival analysis shows no statistically significant correlation between α and $\ln(M_*/L)$, but there are correlations between α and $\log M_{200}$, $\log M_{dyn}$, or distance. Our values are shown as red squares (r-band data) and black squares (IRAC channel-2 data), and the values from Adams, J.J. et al. (2014), Oh, S.-H. et al. (2011) and Oh, S.-H. et al. (2015) are shown as yellow circles, green stars and cyan circles, respectively. The arrows indicate the upper and lower limits (the length of the arrow is only for visual purpose and is not related to any physical quantity). Note that the Oh et al. studies measured α in a notably different way from our study. 68

5.1 Naturally weighted CO(1-0) intensity and velocity distribution maps with masking to enhance the SNR. The data are a combination of observations from CARMA and ALMA. For all galaxies, the RA offset is from +30" (left) to -30" (right), the Dec offset is from -30" (bottom) to +30" (top). The side bar indicates the velocity (in km/s) in the distribution, and the units of the image are pixels. 72

5.2 Rotation curves of the galaxies, obtained from fitting the ALMA and CARMA data using DiskFit in the radial mode with $m = 0$. The exception is NGC 4150, which was fit without the radial component due to the small CO extent. The solid line denotes the combination of ALMA and CARMA data, the black dashed line denotes the CARMA data, and the blue dotted line denotes the Hα data when available. 73

5.3 Example of gNFW fitting to the combination of ALMA and CARMA data. The stellar mass was fit using r-band data. The total rotation curve (magenta), which is fitted to the data (cyan) is the sum of two mass components in the gNFW model: stellar mass (green) and dark matter (blue). "Fix PA_and_eps" and "Fix none" indicate the fixed geometric parameters in the initialization of the fit to obtain the rotation curves. The parameter constraints and covariances of the model were generated using the Markov Chain Monte Carlo (MCMC) method with the python-based software *emcee* (Foreman-Mackey, D. et al. (2013)), 100 walkers and 5000 steps. Five generated sets of parameters were randomly selected after the walkers began converging to plot the curves as shown. 74

5.4 Comparison of the gNFW parameters for mass models constructed using different bands to trace the stellar component and different molecular gas datasets to trace the total matter distribution. The gNFW parameters are the virial mass ($\log M_{200}$), concentration (c_{200}), stellar mass-to-light ratio (M_*/L), density parameter ($\log \rho_0$), scale radius (r_s) and inner slope (α). The modeling is based on the CO kinematics, which is deduced from CARMA dataset (red circles) or a combination of CARMA and ALMA data (cyan circles), with the stellar mass assumed to be proportional to the luminosity in either r-band data (horizontal axis) or IRAC channel-2 (denoted "Ch2") data (vertical axis). The parameters were fit for variable disks (i.e., M_*/L was not fixed). The arrows indicate the upper and lower limits (the length of the arrow is only for visual purpose and is not related to any physical quantity). The plots show that all parameters except M_*/L are robust with respect to the choice of r-band or Ch2 data. 77

5.5 Values of the inner power-law slope α (top), stellar mass-to-light ratios (middle) and virial mass ($\log M_{200}$) of each galaxy in the sample to the gNFW function. The parameters were obtained using either r-band data (black markers) or IRAC channel-2 ("Ch2") data (red markers) for the stellar mass. The arrows indicate the upper and lower limits (the length of the arrow is only for visual purpose and is not related to any physical quantity). 78

List of Tables

1 List of dwarf galaxies with CO observations from CARMA 15
3.1 Integration time in each CARMA array configuration of the dwarf galaxies . . . 17
3.2 CO flux of the galaxies as measured at CARMA 21
3.3 NIR and IR flux of the galaxies to compare with the CO flux measured at CARMA 22

4.1 Best fitted parameters obtained from DiskFit using CO data and those obtained from photometric data 45
4.2 Constraints on the disk geometry from CO and optical imaging 46
4.3 Constraints on the mass distribution from models with a gNFW halo and variable disk 52

5.1 Constraints on the mass distribution from models with a gNFW halo and variable disk, using the combination of ALMA and CARMA data 71

Acknowledgments

This dissertation is the culmination of many years of work and would not have been possible without the help and support of an incredible number of people.

First, I would like to thank my research advisor, Professor Leo Blitz, who introduced me to the field of gas in galaxies, which forms the core of this work. As many former graduate students who have had the opportunity to work with Leo have said in their dissertations, not only has Leo's passion for astronomy been an inspiration to me, his guidance and understanding have also been invaluable in many ways.

I would also like to thank all of my co-authors for their contributions to this dissertation. Specifically, I would like to thank Drew Newman, Nicole Relatores, and Josh Simon for the technical knowledge and scientific insight that has been critical to the project, and for reviewing my works numerous times with careful attention. I also thank Drew for the observing trip to Palomar Observatory, I have learned so much from you, and Richard for the presence throughout the project, your light-hearted humor and stories make one aspired to be an astronomer. I further thank my thesis committee co-chair and members, especially Leo and Chung-Pei Ma, for helping to evaluate this project in its early stages, reviewing the results, and giving speedy approval towards completion.

The bulk of my work at UC Berkeley involved observations at radio wavelengths, and I cannot sufficiently express my gratitude for the community of radio astronomers and physicists at and from Berkeley and the associated observatories. First, I have to thank Dick Plambeck and Melvyn Wright for my introduction to radio astronomy at the CARMA Summer School and their continuous assistance over the past several years. Further thanks to Amber Bauermeister and Chat Hull for their patient help in the early days of my acquaintance with the radio astronomy, Garrett Keating for teaching me how to be an observer at the CARMA observatory, and Katey Alatalo for your technical help and emotional support both online and during the brief times that we met at Carnegie Observatories in Pasadena. Special thanks to Dyas Utomo, your friendship and answers to my questions about coding have contributed a huge part to the completion of this work.

I must also thank the former observers and staff at CARMA, the observatory that I have been a part of and where I have spent many memorable days. Without all of you, the work of this dissertation would not have been possible. At CARMA, I thank the entire staff for keeping it running for the time it did. Especially, I must thank Nikolas Volgenau for supporting the observers with incredible patience and reliability, John Carpenter for

teaching me much more than I thought I could know in such a short amount of time about flux calibration, and Cecil for feeding me so well and for all of our pleasant conversations.

Many sincere thanks to the advisors in the Physics and Astronomy department, especially Anne Takizawa and Dexter Stewart, who have always been there for my questions about procedures, funding, etc. I believe that I speak for all students in both departments that we would have been lost without your resourcefulness, kindness and patience.

Thanks to Jenna, Victoria, Kristen, Oanh, Cheryl, Maggie, Iris, Monatrice, and Grace (in chronological order of the first time we met, definitely not of how much I like you, for your friendships are special in incomparable ways. You have come into my life at different times and know different stages of me; while it is uncertain when we will meet again, I am sure that our times talking, laughing, studying, lamenting, reading, exploring, eating, cooking together are what I will always remember of grad school, and what I so strongly hope to share with you again in the future. Kristen, thank you for being my partner in crimes, you are the sister I have always wished to have.

Special thanks to Bryan for the cute animal pictures when I am stressed, for driving with me to CARMA, helping me with the qualification oral exam, introducing me to your loving family, and most importantly, for your constant support and words of encouragement throughout the years that we have known each other. Despite the distances, you have been there for me with unwavering trust, humor and positivity, which helped pulling me through existential crises (or is it just midlife crises?) and sleepless nights. I hope to do the same for you.

I would like to thank the cats at the Berkeley Humane Shelter as well as the staff and volunteers there. Beloved kitties, your companionship keep me sane in the last 6 months. You have given me a place of refuge where I can feel useful and content again, and you have shown me a new goal to reach. I wish you guys a whole lot of happiness with your new families because you guys deserve the best.

Looking back, I also wish to sincerely thank my professors at Texas A&M University, especially Prof. Dutta for his guidance in theoretical physics, Prof. Agnolet for his fatherly presence throughout my undergraduate years, and Prof. Fry for making the Physics department at A&M such a welcoming environment, which fortified my decision to pursue a Ph.D. degree in this field. I also thank Ms. Baker, not only my physics teacher in high school but also family in the past 13 years, without whom my interest in physics might not have flourished into a major in college in the first place, and I might have chosen chemistry instead. Thank you, Louise and Herb, for choosing me to be a part of your family, I will remember you always.

Finally, my gratitude goes to Mom and Dad. You are the principle reason that I get where I am today and in the future. I would have given up many times had you not been there, vocally, silently, in every word and action, caring for me with all your best. You set a wonderful example of overcoming the multitude of adversities, making the right choices and laying the foundations for future success. Thank you for being the home to which I can look forward to returning and that I can proudly treasure.

To everyone I have been able to encounter, thank you.

Chapter 1

Introduction

1.1 Science background

Cosmological simulations have shown that cold dark matter models (CDM and ΛCDM) give rise to a universal density profile for dark matter (DM) halos: NFW profiles (Navarro, J. F. et al. (1996)), where the density increases with decreasing radius in the central region ($\rho \propto r^{-\alpha}$, where $\alpha = 1$ for r smaller than the scale radius). In other words, these simulations suggest a central-cusp density profile for halos ranging from dwarf galaxies to galaxy clusters. However, observational studies of nearby dwarf galaxies have found density profiles in the central region spanning a wide range of distributions from constant-density cores to nearly cuspy profiles (e.g., de Blok, W. J. G. et al. (2001a), Borriello, A. & Salucci, P. (2001), Simon, J.D. et al. (2005), Oh, S.-H. et al. (2011), Adams, J.J. et al. (2014)). This inconsistency between simulations and observations at the inner parts of galaxies is known as the core-cusp problem in galactic-scale cosmology.

Over the past two decades, much theoretical work has been devoted to explaining the observed core-like DM distributions in some galaxies. The mechanisms to reduce the central density can be classified into three categories:

- structural features in real galaxies, such as clumps of mass or bars. The relative motion of the features transfers energy or angular momentum from baryons to DM, pushes DM outward and flattens the initial cusp (e.g., El-Zant, A. et al. (2001), Tonini, C. et al. (2006), Weinberg, M.D. & Katz, N. (2007a), Weinberg, M.D. & Katz, N. (2007b)). However, such features were not included in the N-body simulations of, e.g., Navarro, J. F. et al. (1996);

- non-CDM models (warm DM, self-interacting DM, dissipative DM, etc.) (e.g., Kaplinghat, M. (2005), Rocha, M. et al. (2013), Foot (2015));

- baryonic feedback, most notably the repeated expansion and contraction of the interstellar gas caused by supernovae (e.g., Pontzen, A. & Governato, F. (2012), Arraki, K. S. et al. (2014), Kato, K. et al. (2015), Chan, T. K. et al. (2015), etc.).

Although some of these simulations and models have been disputed (as explained in more detail in Adams, J.J. et al. (2014)), it is true that several theories exist to explain the shallow density profiles of dwarf galaxies. At larger masses, studies of galaxy clusters using kinematics and gravitational lensing to constrain the mass show that the inner regions ($\leq$ 30 kpc $\sim 0.003 - 0.03 r_{200}$) have shallower density profiles than the NFW profiles (Newman, A. B. et al. (2013b), Newman, A. B. et al. (2013a)). If the density profile measurements in the literature are accurate, it is unclear whether any single explanation can account for these observed profiles over many orders of magnitude in halo mass, or whether several mechanisms must act together over different mass scales.

On the observational side, there are many analyses of HI data (de Blok, W. J. G. et al. (1996), de Blok, W. J. G. & McGaugh, S. S. (1997), Oh, S.-H. et al. (2011), Oh, S.-H. et al. (2015)), optical long-slit spectroscopy data (van den Bosch, F.C. & Swaters, R.A. (2001), McGaugh, S. S. et al. (2001), de Blok, W. J. G. et al. (2001a), de Blok, W. J. G. et al. (2001b), de Blok, W. J. G. & Bosma, A. (2002), Swaters, R.A. et al. (2003a)), and integral field spectrograph (IFS) data (Swaters, R.A. et al. (2003b), Simon, J.D. et al. (2003), Simon, J.D. et al. (2005), Kuzio de Naray, R. et al. (2006), Kuzio de Naray, R. et al. (2008), Adams, J.J. et al. (2014)) on the subject. These data have shown that late-type dwarfs (e.g., spirals and irregulars) generally have rotation curves that rise more slowly than the NFW profile, although the highest-quality data do not prefer strongly cored profiles. However, the interpretation of long-slit spectra along the major axis of the galaxies could be subjected to various systematic errors, such as misalignment of the position angle of the slit with that of the galaxy, missing information on the asymmetries, or non-circular motions of the gas. IFU and interferometric maps are less susceptible to such systematic errors and can quantify non-circular motions over a range of azimuthal angles. However, improved resolution, sensitivity and analysis techniques have not removed the core-like DM profiles in HI data, suggesting that they are unlikely to be manifestation of observational uncertainties alone (Oh, S.-H. et al. (2011)). In recent years, three high-resolution surveys of dwarf galaxies have been undertaken to examine this core-cusp problem: 7 THINGS galaxies (Oh, S.-H. et al. (2011)), 26 LITTLE THINGS galaxies (Oh, S.-H. et al. (2015)) (note that the subset of THINGS and LITTLE THINGS galaxies that is useful for detailed mass modeling is much smaller than the full samples), and another 7 dwarfs in Adams, J.J. et al. (2014)), who used SDSS photometric data, archival HI data and IFU data from VIRUS-W. All three samples consistently show that the logarithmic inner slope of the DM density profiles with respect to radius is significantly lower than 1: the average value of α is 0.29 ± 0.07 (Oh, S.-H. et al. (2011)), 0.32 ± 0.24 (Oh, S.-H. et al. (2015)) and 0.58 ± 0.24 (Adams, J.J. et al. (2014)).

1.2 Goal of our study

In an attempt to increase the sample size, obtain better constrained rotation curves and resolve the long-standing discrepancy between simulations and observations, we have begun a new survey aimed at measuring the DM distribution in a large sample of dwarf galaxies

using high-resolution CO interferometry and Hα IFU spectroscopy. On one hand, the CO measurements help us probe near the center of the galaxies to obtain the least biased inner slope of the rotation curves. On the other hand, the Hα measurements let us observe the rotation curve further out than it is possible with CO, which enables us to better constrain the functional form of the rotation curves and consequently the DM distribution. In detail, the advantages of CO and HI interferometry are:

- improved spectral resolution: CO resolution is approximately 2.5 kms^{-1}; HI resolution $\approx$ 2.3 kms^{-1} (Oh, S.-H. et al. (2011)); IFU resolution $\approx$ 35 kms^{-1} (Adams, J.J. et al. (2014));
- unaffected by extinction;
- most molecular cloud emission is concentrated at the center of the galaxies, which is the region of interest;
- complete spectral imaging information to produce reliable rotation curves;
- better tracer of the gravitational potential near the center than Hα (ionized gas is subjected to "champagne flows"[1], which affects the Hα-derived velocity curve, whereas CO emission is from giant molecular clouds and does not exhibit this flow behavior). In addition, at least part of the Hα emission may be in a thick disk in some galaxies, the upper layers of which will have lower rotation velocities.

The CO interferometric data were obtained at CARMA (Combined Array for Research in Millimiter-wave Astronomy, California, US). The Hα integral field spectroscopy data are obtained using the Cosmic Web Imager (CWI) (Matuszewski, M. et al. (2010)) at Palomar Observatory (Relatores et al. in preparation). Together with the CO data, the Hα data give us a check on the systematic errors. For the CO data analysis, we use two different rotation curve fitting programs (DiskFit (Spekkens & Sellwood 2007) and RingFit (Simon et al. 2003)) to obtain the velocity profiles of the galaxies. Then, for the mass modeling, we first assume that the velocity profile of each galaxy receives contributions from five components: dark matter, molecular gas, atomic gas, stars, and dust. Assuming negligible dust, HI amd H_2 contributions, the velocity profile (and consequently, the density profile) of the dark matter component can be obtained from the CO rotation curves by subtracting the sum of baryonic contributions (measured from optical or near-IR imaging data) following the procedures of Simon et al. (2005). We will show in future work that adding the HI component (from archival HI data) and H_2 component (deduced from the obtained CO measurements) does not significantly change the results. The project, which we call the Dwarf Galaxy Dark Matter (DGDM) Survey, measures the radial distribution of DM at the scale of $\sim$ 100

[1]In the astrophysical event so-called "champagne flow", an HII region is created inside a molecular cloud from ionization because of a recently formed star and expands outward until it reaches the interstellar medium; then, the ionized hydrogen gas bursts outward like an uncorked champagne bottle. Tenorio-Tagle, G. (1979)

parsecs and helps correlate the DM properties with the baryonic mass, gas density, star formation history, age, and other properties of the galaxy sample.

To examine the mass distribution and star formation history of the galaxies in the sample, future studies will contain a presentation of the full Hα sample, including the rotation curves, photometry and mass modeling (Relatores et al., in preparation). By comparing and combining CO and Hα data, we will be able to draw conclusive results on the robustness of the DM slope, its distributions and scatter, and any correlations with galaxy properties.

In this dissertation, we present the CO data and our analysis in five chapters. First, Chapter 1 provides an overview of the research background and motivation of this study. Chapter 2 takes a step back to briefly describe dark matter, its presence in large-scale structure, historical and current theoretical models that attempt to explain its formation and distribution in galaxies, and observation evidences. In Chapter 3, section 3.1 describes our criteria to select galaxies for the survey in our study; section 3.2 describes the CARMA observation; section 3.3 describes the data reduction; section 3.4 presents the reduction results and discussion, which includes the comparisons between our CO flux and past observations (single-dish CO measurements and infrared measurements) and correlations between the molecular gas content and atomic gas content.Then, in Chapter 4, section 4.1 describes our data analysis using DiskFit and Ringfit, including the models to fit the rotation curves and fitting parameters; section 4.2 discusses the rotation curve fitting results; in section 4.3, we describe different mass models that we apply to the obtained rotation curves and the resulting density profiles in comparison with other studies in the literature; 4.5 discusses the important indications of the mass modeling results. Finally, Chapter 6 summarizes the study, provides the findings on the density profiles, and proposes the future steps.

The content of this dissertation has been submitted for publication in the Astrophysical Journal (2016) under the title of "High-resolution velocity fields of low-mass disk galaxies I: CO data", and another part of this dissertation is to be submitted to the Astrophysical Journal (2017) under the title of "High-resolution velocity fields of low-mass disk galaxies I: CO rotation curves and mass modelling".

Chapter 2

Overview of dark-matter studies related to the core-cusp problem

2.1 The presence of dark matter

In astronomy, there is overwhelming evidence that most of the mass in the universe is some nonluminous "dark matter" of yet unknown composition. The two most convincing evidences for the existence of dark matter are: the Bullet cluster, which shows the separation of dark matter from luminous matter (Clowe, D. et al. (2003), Markevitch, M. et al. (2003)), and the flat rotation curves of spiral galaxies at nuclear distances as great as 50 kpc (Rubin, V. C. et al. (1978) and Figure 2.1), which indicates that the density of luminous matter (e.g., stars and dust) is not large enough to account for the observed high rotation velocities in the outer parts of the galaxies; hence, another type of matter, so-called "dark matter", must be present. Furthermore, observational results such as those obtained from the Wilkinson Microwave Anisotropy Probe (WMAP) indicate that baryonic matter comprises only 4% of the universe, while 22% is composed of dark matter (Jarosik, N. et al. (2011)). Dark matter plays a central role in the current modeling of cosmic structure formation, galaxy formation and galaxy evolution, and on the explanations of observed anisotropies in the cosmic microwave background (CMB), which also shows that dark matter is universally present in all large-scale structures across the universe.

There are many candidates for the composition of dark matter, among which the most probable ones are nonbaryonic, that is, that they are some new elementary particles. Among the nonbaryonic candidates, an important categorization scheme is the "hot" versus "cold" classification. A dark matter candidate is called hot if it was moving at relativistic speeds at the time galaxies could just start to form, and it is called cold if it was moving nonrelativistically at the time and interacts very weakly with ordinary matter and electromagnetic radiation. Simulations of structure formation in a universe dominated by hot dark matter, however, do a poor job of reproducing the observed structure. The cold dark matter candidates are basically elementary particles that have not yet been discovered, such as weakly interacting massive particles (WIMPs) that arise in extension of the standard model of elec-

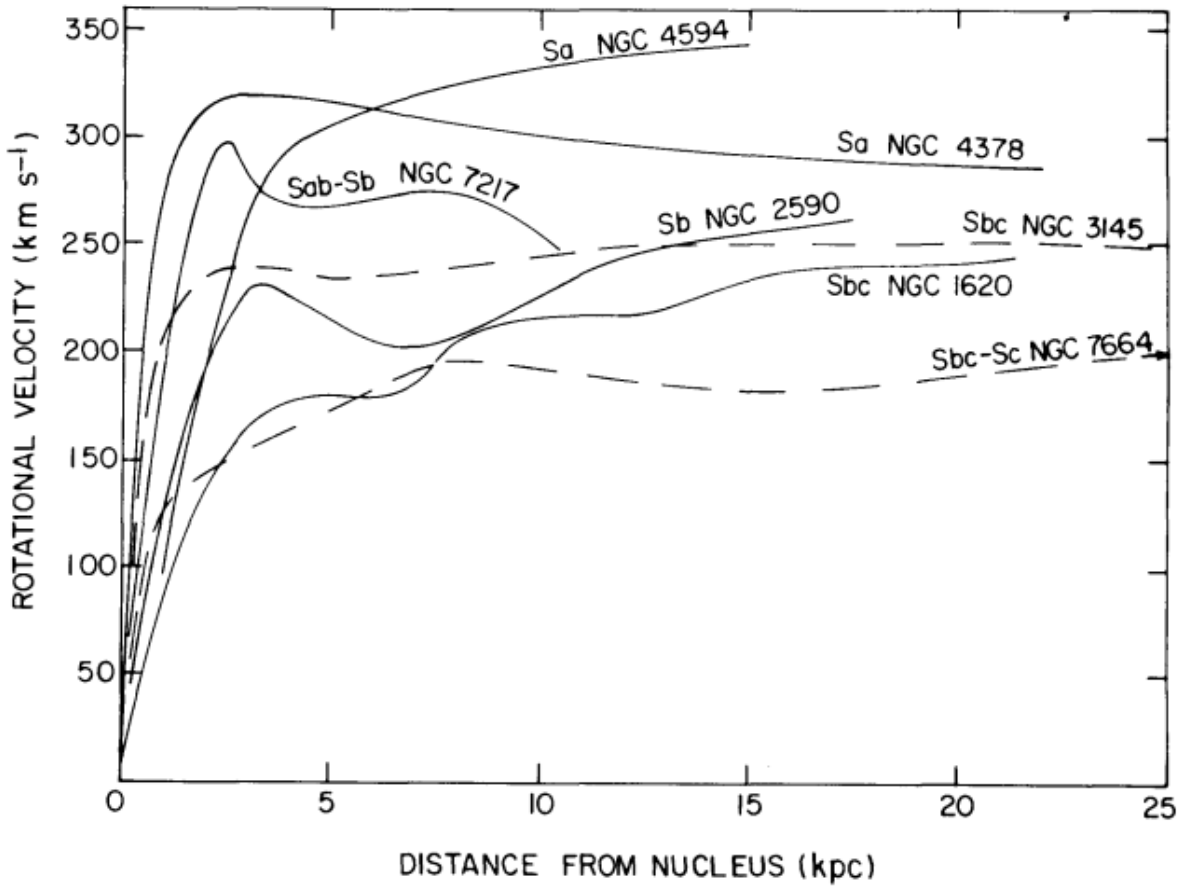

Figure 2.1: Rotational velocities for 7 galaxies as a function of the distance from the nucleus. The curves were smoothed to remove velocity undulations across the arms and small differences between the major-axis velocities on each side of the nucleus. Early-type galaxies consistently have higher peaks than late-type ones. Figure and caption from Rubin, V. C. et al. (1978).

troweak interactions. One of the most well established models of cold dark matter is the Lambda Cold Dark Matter (ΛCDM) model, which parametrizes the Big Bang cosmological model such that the universe contains a cosmological constant Λ, associated with dark energy, and cold dark matter. The ΛCDM model is the simplest and most concordant cosmological model that can reasonably account for several characteristics of the universe: the existence and structure of the CMB, large-scale structure in the distribution of galaxies, abundances of hydrogen (including deuterium), helium, and lithium, and accelerating universe expansion, which is deduced from the observations of distant galaxies and supernovae.

In order to model the structure of dark-matter halos in the ΛCDM cosmology, Navarro, J. F. et al. (1996) derived the so-called NFW density profile using N-body simulations. In

the NFW model, the simulated objects have masses ranging from those of dwarf galaxy halos to those of galaxy clusters, and a simple universal profile can be fitted to all halos in the simulation. This spherically averaged density profile strongly correlates with the halo mass, which reflects the mass dependence of the halo formation epoch. In general, the halo profiles are approximately isothermal ($\rho \propto r^{-}2$, where ρ is the density profile, and r is the radius from the center) over a large range in radii but are significantly shallower than r^{-2} near the center and steeper than r^{-2} near the virial radius. At large scales, e.g., the observations of bright galaxies like the Milky Way and M31, the NFW profile is a good description of dark matter halos. However, for smaller galaxy masses and radii, both CDM simulations in general and the NFW model in particular face three observational challenges:

- the core-cusp problem: the density distributions of dark-matter halos in cold-dark-matter simulations are much steeper than the observed profile in galaxies by investigating their rotation curves. (Gentile, G. et al. (2004))
- the missing-satellite problem: CDM simulations produce a much larger number of dwarf galaxies than that observed around galaxies like the Milky Way (Klypin, A. et al. (1999)),
- the disk of satellites problem: dwarf galaxies around the Milky Way and Andromeda galaxies are observed to orbit in thin, planar structures, whereas the simulations predict that their random distribution around their parent galaxies. (Pawlowski, M.S. et al. (2014))

In this work, we will focus on the core-cusp problem, which is reviewed as follows.

2.2 Simulations versus observations

As previously discussed, on one hand, the observed constant velocity in the rotation curves of galaxies suggests that the dark matter at large radii has a mass density profile closely resembling that of an isothermal sphere, i.e., the density $\rho \propto r^{-2}$. On the other hand, in the inner part of the galaxies, although DM is present, the stars constitute a dominant mass component. Hence, there is a transition between the star-dominant inner part and the DM-dominant outer part. For disk galaxies, the rotation velocity associated with dark matter in the inner parts increases approximately linearly with radius, which indicates a central core in the DM mass distribution and was described by the pseudo-isothermal model, developed by Begeman, K.G. et al. (1991):

$$\rho_{pseudo-isothermal} = \frac{\rho_0}{1 + (r/R_C)^2} \tag{2.1}$$

where ρ is the density, r is the radius from the center, ρ_0 is the central density, and R_C is the core radius of the DM halo.

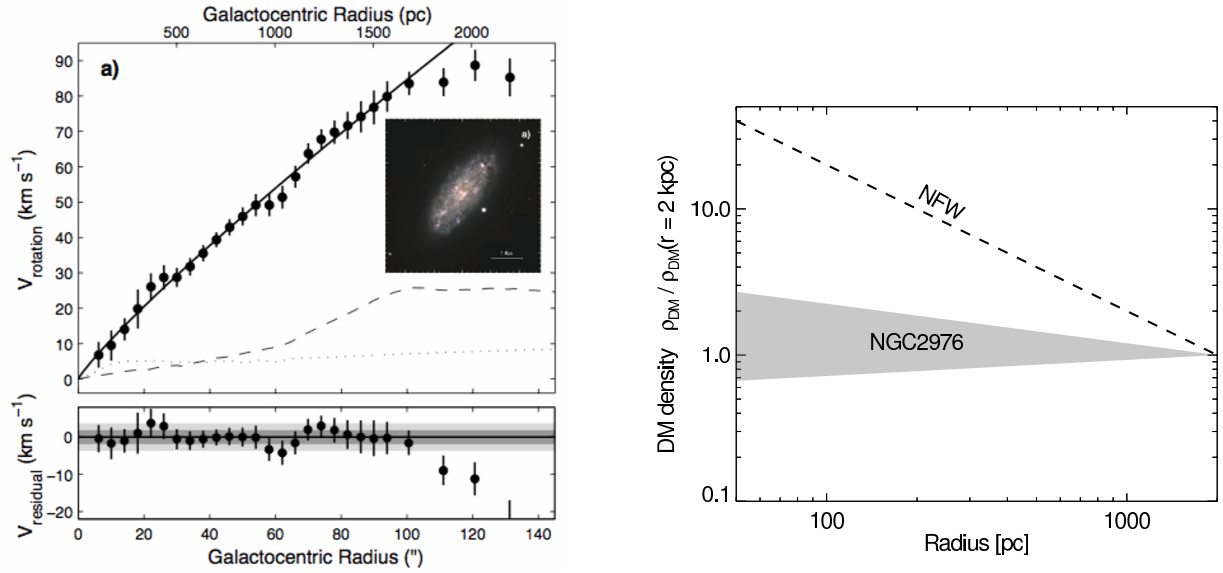

Figure 2.2: Left: Image and combined CO/Ha rotation curve extracted from 2-D velocity fields of NGC 2976 a nearby (d = 3.6 Mpc) dwarf disk galaxy from Simon et al. (2003). Right: The dynamics imply a DM density slope of $r \propto r^{-0.01}$ (shaded region indicates the 1σ uncertainty), which is much flatter than the canonical slope $r \propto r^{-1}$ expected for the cosmologically motivated CDM profile. Understanding the origin of the shallow DM density slopes and quantifying any correlation with the host galaxy properties is the primary goal of our study.

Such core structures are observed in early HI data of low-mass disk galaxies, which are dominated by DM; for example, Flores, R.A. & Primack, J.R. (1994) and Moore, B. (1994) revealed rotation curves that rose notably slowly with the radius.

However, instead of the core structure, when numerical simulations were developed using the ΛCDM model, which is the standard paradigm in cosmology and structure formation, the simulations predict a sharply rising DM density profile in the inner regions of galaxies, regardless of their total mass (Navarro, J. F. et al. (1996)):

$$\rho_{NFW} = \frac{\rho_0}{r/R_s(1 + r/R_s)^2} \tag{2.2}$$

where R_s is the scale radius.

Although ρ_0 and R_s are parameters that vary for different halos, the above predicted correlation of the density profile is universal and remains one of the central predictions of the theory. In such profile, at $r \ll R_s$, the relation becomes $\rho \sim r^{-1}$, i.e., the density sharply rises with decreasing radius and forms a central cusp. This prediction was not consistent with observations, hence the "core-cusp" problem of the standard model in cosmology.

A number of concerns were raised regarding the observations. First, the low spatial resolution of early HI data might suggest that beam smearing could produce apparent cores

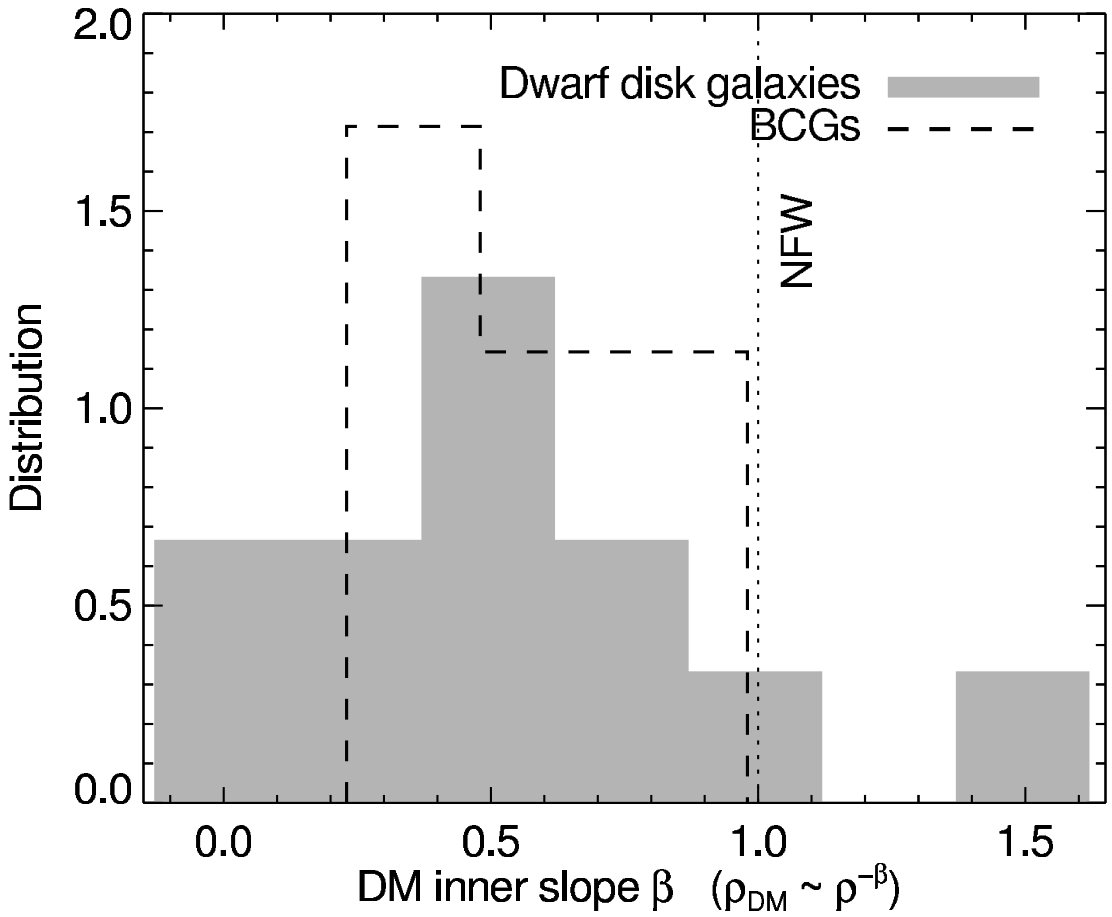

Figure 2.3: Current status of the dark-matter density slope in dwarf galaxies from high-resolution data (shaded; Simon, J.D. et al. (2005), Oh, S.-H. et al. (2011)). Most measurements indicate shallower slopes than an NFW profile ($\alpha = 1$) but a few are consistent with the cuspy profiles. We aim to better quantify this scatter with a significantly larger sample and search for its physical origin by correlating α with the host galaxy properties. For comparison, we overplot the DM slopes for brightest cluster galaxies by Newman, A. B. et al. (2013b) and Newman, A. B. et al. (2013a). These studies also indicate DM slopes with $\alpha < 1$.

in galaxies, which actually had steeper mass profiles (van den Bosch, F.C. & Swaters, R.A. (2001)). Long-slit observations that traced Hα emission (e.g., de Blok, W. J. G. et al. (2001a)) had improved angular resolution, but these 1-D cuts through the velocity field introduced additional ambiguities. Full 2-D sampling, which can accurately reconstruct dynamical models in detail to account for the radial motions in the disk plane and eliminate slit placement errors as well as other systematic uncertainties, are required. (For more details

on the discrepancy between simulations and observations prior to 2010, see the review of de Blok, W. J. G. (2010).) Thus, later studies (e.g., Bolatto, A.D. et al. (2002), Simon, J.D. et al. (2003), Simon, J.D. et al. (2005), Kuzio de Naray, R. et al. (2006), Kuzio de Naray, R. et al. (2008), Oh, S.-H. et al. (2015)) significantly improved the observational results by gathering 2-D velocity maps for several dwarf galaxies with high angular and spectral resolutions in CO and Hα using millimeter-wave arrays and integral field spectrographs. Interestingly, these observations revealed a range of inner DM slopes: 0.65 (NGC 4605, Bolatto, A.D. et al. (2002)), 0.27 $\pm$ 0.09 (NGC 2976, Simon, J.D. et al. (2003)), 0.0-1.2 (5 galaxies, Simon, J.D. et al. (2005)), -0.13-0.43 (7 galaxies, Oh, S.-H. et al. (2011)), and -0.01-1.25 (26 galaxies, Oh, S.-H. et al. (2015)). The range of slopes in fact contradicts the universality predicted by CDM simulations: some galaxies with the DM inner slope of ~ 1 are consistent with CDM predictions, but others have much shallower slopes (Figure 2.2).

As mentioned in Chapter 1, many theories attempt to explain the discrepancy, e.g., non-CDM particle (the so-called warm DM models), self-interacting DM (with a finite scattering cross-section that becomes significant in dense regions), adjustment of the DM distribution arising from recurring events of energetic baryonic feedback or flattening of the central cusp, and dynamical interaction with a bar or other baryonic matter. In recent years, theoretical efforts considering warm or self-interacting DM have intensified (e.g., Rocha, M. et al. (2013), Peter, A.H. G. et al. (2013), Vogelsberger, M. et al. (2016)), particularly as evidence for flattened dark matter profiles has increased on other mass scales, including those in Milky Way satellites (Boylan-Kolchin, M. et al. (2012)) and the central galaxies in massive clusters (Newman, A. B. et al. (2013b), Newman, A. B. et al. (2013a); Figure 2.3). Other non-CDM candidates are also proposed and verified with the core-cusp problem, such as wave dark matter (Chen, S.-R. et al. (2017)), which predicts a central soliton core in galaxies because of the balance between quantum pressure and gravity.

Furthermore, recent baryonic feedback models offer many mechanisms in which the central DM cusp may be flattened to suit the observed values. For example, in the hydrodynamical simulations in Governato, F. et al. (2010), strong outflows from supernovae remove the low-angular-momentum gas in dwarf galaxies, which inhibits the formation of bulges and decreases the dark-matter density by less than half in the central kiloparsec. In Governato, F. et al. (2012), the simulations take into account star formation and rapid, repeated supernovae-driven gas outflows at high redshifts, which transfer energy to the DM component and significantly flatten the originally cuspy central DM mass profile; this mechanism creates galaxies with stellar masses of $10^{4.5} - 10^{9.8} M_\odot$ at $z = 0$. They also found that the DM slope $\alpha = -0.5 + 0.35 \log_{10}(M_*/10^8 M_\odot$ by fitting $\rho \propto r^\alpha$ to the density profile of the simulated galaxies. In Macciò, A.V. et al. (2012), the increased stellar feedback causes the DM halo to expand, hence creating a flat, cored, DM density profile in the central several kiloparsecs of a massive Milky-Way-like halo. However, in this simulation, the stellar disk remains partially too thick to resemble the Milky Way thin disk. Di Cintio, A. et al. (2014) simulated galaxies (in the stellar mass range of $10^5 - 10^{10} M_\odot$) with blastwave supernova feedback and an additional source of energy from massive stars to show that the inner DM slope clearly depends on the stellar-mass-to-light ratio: a low ratio corresponds to inefficient

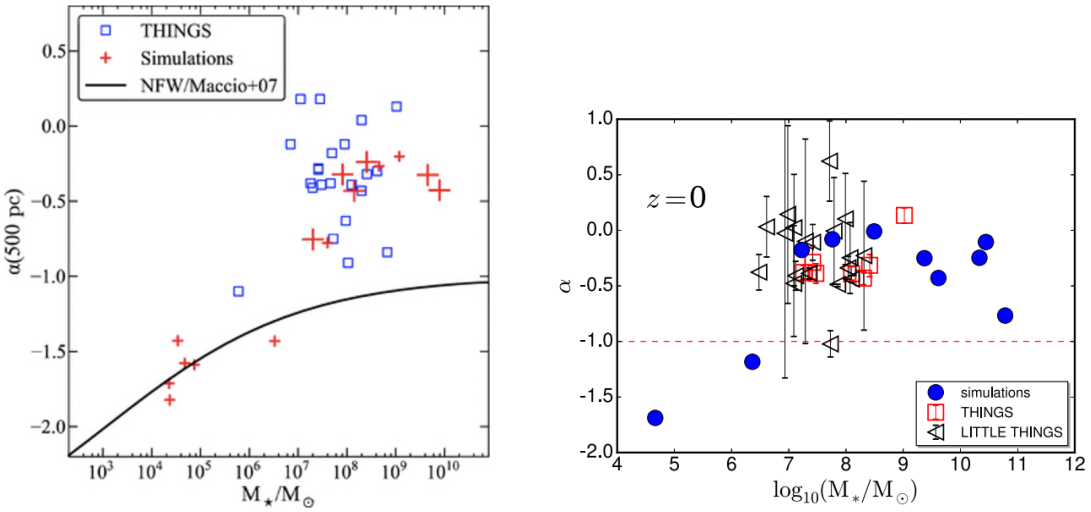

Figure 2.4: The slope of the DM density profile α versus stellar mass for the halos in the simulations of Governato, F. et al. (2012) (left) and Chan, T. K. et al. (2015) (right). In the left panel, the slopes of the simulated galaxies were measured at $r = 0.5$ kpc and $z = 0$; the solid "DM-only" line is the slope predicted for the same CDM cosmological model assuming (i) the NFW concentration parameter trend of Macció et al. (2007) and (ii) the measured relation of stellar mass versus halo mass in the simulations to convert from halo masses. Large crosses: haloes resolved with more than 0.5×10^6 DM particles within the virial radius. Small crosses: more than 5×10^4 DM particles. The small squares represent 22 observational data points measured from galaxies from the THINGS and LITTLE THINGS surveys. In the right panel, the slopes of the simulated galaxies were measured at $r = 0.3 - 0.7$ kpc and $z = 0$. Images from Governato, F. et al. (2012) and Chan, T. K. et al. (2015).

feedback to alter the cuspy profile, whereas at a high ratio, the feedback causes the halo to expand and form a cored profile. Furthermore, using cosmological simulations from the FIRE (Feedback In Realistic Environments) project, Chan, T. K. et al. (2015) find that stellar feedback induce core formation through several bursts of star formation, but only after the period of rapid growth of the haloes, when DM mass continuously accumulates. In general, these models produce similar profiles to the HI observations in THINGS and LITTLE THINGS (Walter, F. et al. (2008), Oh, S.-H. et al. (2011), Oh, S.-H. et al. (2015)) (e.g., see Figure 2.4). The galaxies in our sample have large masses than those in THINGS and LITTLE THINGS, so we will be interested in comparing our results and check whether the correlation between the DM slope and stellar mass found by Governato, F. et al. (2012) still holds in our mass range. In another approach to baryonic feedback, Trujillo-Gomez, S. et al. (2015) use radiation pressure from massive stars in simulations of dwarf and disk galaxies to produce constant and rising star formation histories that match the constraints across various redshifts; however, such feedback mechanism does not sufficiently flatten the cusp: their most flattened simulated DM halo has $\alpha = 0.7$ (Adams, J.J. et al. (2014)). Silk, J.

(2017) also suggests a feedback mechanism from massive black holes ($\sim 10^2 - 10^5 M_\odot$), which form from a combination of dynamical merging of smaller black holes and gas accretion, and associated processes to flatten the central cusp, but the study did not include simulation or observation results to verify such hypothesis.

Overall, there are several models that attempt to resolve the core-cusp problem, and each hypothesis can account for the discrepancy in several cases. However, the tested mass range of the dwarf galaxies remains small, and it is unclear whether any single explanation can account for these observed profiles over many orders of magnitude in halo mass, or whether several mechanisms must act together over different mass scales. Thus, to distinguish the mechanisms and their effects, further observations are required.

Chapter 3

CO Data

3.1 Target Selection

In preparation for the DMDG survey, we compiled a list of 172 nearby HI-detected and CO-detected small-mass galaxies from the literature[1] using the following criteria:

1. The galaxies are low-mass galaxies, which we define as galaxies with an HI line width (W_{20}) $\leq$ 200 kms^{-1}. As a matter of convenience, we will call them "dwarfs" henceforth, although traditional dwarf galaxies tend to have even lower masses and rotational velocities.

2. The galaxies have low luminosity, i.e., absolute magnitude $M_B \geq -18$.

3. The distance is less than 35 Mpc; the systemic velocity in the local standard of rest (v_{LSR}) is below 2000 kms^{-1}. This limit provides better spatial resolution than 80 pc for all targets.

Of these 172 galaxies, 63 have strong CO detections, and 42 have published upper limits in the literature. For the remaining 67 galaxies, some have been observed and detected in ^{12}CO(1-0), but no numerical value of the CO flux or intensity was published.

Among these 172 galaxies, we further narrowed our preferences to select dwarfs that have the following properties (in addition to the above 3 criteria):

1. symmetrical, non-disturbed visual appearance

2. not being classified as a barred galaxy, and not containing a visually obvious bar

[1]The galaxies were selected from the following compilations: Leroy, A.K. et al. (2005), Karachentsev, I. D. et al. (2003), Walter, F. et al. (2008) (the THINGS catalog), Leroy, A.K. et al. (2009) (HERACLES), Ott, J. et al. (2012) (VLA ANGST), Mateo, M. L. (1998), Young, J. S. et al. (1995), Obreschkow, D. & Rawlings, S. (2009), Welch, G.A. & Sage, L.J. (2003), Matthews, L. D. et al. (2005), Sauty, S. et al. (2003), Andreani, P. et al. (1995), Sage, L.J. (1993), Lees, J. F. et al. (1991), and Swaters, R.A. et al. (2002).

3. inclination angle of $30 - 70°$,

4. diameters > 1 arcmin (to provide enough extent for the Hα measurements).

5. strong mid-IR flux. This criterion was selected using the infrared images provided by WISE (Wright, E. et al. (2010)). To show clear dust properties, the galaxies should be detectable in the infrared at 22 μm. Because there is a strong correlation between the 22 μm flux and star formation rate, and consequently CO, selecting galaxies with strong 22 μm detection should maximize the chances of observing CO emission.

Table 1: List of dwarf galaxies with CO observations from CARMA

name	RA	Dec	vrot (km s^{-1})	v_{LSR} (km s^{-1})	distance (Mpc)	M_B	type	diameter (arcmin)	diameter (kpc)	inclination (deg)	PA (deg)
NGC 746	01:57:51.0	44:55:07	58	704	12	-16.9	Im	1.9	6.63	51	90
NGC 853	02:11:41.2	-09:18:22	60	1520	20	-16.2	Sm	1.5	8.72	56	65
NGC 949	02:30:48.6	37:08:12	91	607	10	-17.8	Sab	2.4	6.81	68	145
NGC 959	02:32:23.9	35:29:41	74	594	10	-17.2	Sdm	2.3	6.69	62	70
NGC 1012	02:39:14.9	30:09:05	96	982	18	-18.6	S0/a	2.5	13.09	68	20
NGC 1035	02:39:29.1	8:07:59	116	1229	17	-18.3	Sc	2.5	12.36	75	150
UGC 3371	05:56:38.6	75:18:58	72	821	18	-17	Im	4.6	24.09	46	130
UGC 4169	08:02:32.9	61:23:17	107	1608	32	-19.2	Scd	1.5	13.96	63	110
NGC 3622	11:20:12.4	67:14:30	73	1305	27	-18.9	Sc	1.3	10.36	68	50
NGC 4150	12:10:33.6	30:24:06	-	225	14	-18.3	S0	2.3	9.37	58	145
NGC 4310	12:22:26.3	29:12:29.8	79	919	10	-17.4	SAB	2.2	6.21	57	160
NGC 4376	12:25:18.0	5:44:28	73	1139	14	-16.8	I	1.4	5.70	62	70
NGC 4396	12:25:58.8	15:40:17	88	-124	16	-	Scd	3.3	15.17	72	120
NGC 4451	12:28:40.5	9:15:32	116	868	27	-17.7	Sbc	1.5	11.78	54	160
NGC 4632	12:42:32	-00:04:57	108	1726	18.5	-20.6	Sc	3.1	16.68	71	62
NGC 4701	12:49:11.6	3:23:19	101	725	17	-18.4	Sc	2.8	13.85	43	50
NGC 5204	13:29:36.5	58:25:07	56	213	5	-16.6	Sm	5.0	7.27	59	172
UGC 8516	13:31:52.6	20:00:04	60	1033	23	-17.6	Scd	1.1	7.44	49	45
NGC 5303	13:47:45.0	38:18:17	83	1431	24	-18.5	Sbc	1.1	7.68	62	84
NGC 5692	14:38:18.1	3:24:37	96	1573	30	-19.02	S	1.0	8.64	53	32
NGC 5949	15:28:00.7	64:45:48	87	445	15	-18.4	Sbc	2.4	10.47	69	143
NGC 6106	16:18:47.1	07:24:39	134	1464	25	-19.2	Sc	2.5	18.18	59	145
NGC 6207	16:43:03.7	36:49:57	115	871	20	-19.4	Sc	3.0	17.45	65	20
UGC 11891	22:03:33.9	43:44:57	87	508	9	-16.4	Im	4.2	10.99	43	113
UGC 12009	22:22:40.2	37:58:39	98	1252	20	-18	Sb	1.4	8.14	60	175
NGC 7320	22:36:03.4	33:56:53	82	797	19	-18.4	Sd	2.2	12.16	68	109

Note. — The RA, Dec, v_{LSR}, distance, type and diameter (in arcminute) were obtained from the NASA/IPAC Extragalactic Database (NED) at http://ned.ipac.caltech.edu. (For the distance, we used the mean distance value from NED.) v_{rot}, M_B, inclination and PA were obtained from the HyperLEDA catalog at http://www-ob.univ-lyon1.fr, with the exception of UGC 11891: the PA was not available in HyperLEDA and obtained from our photometric measurements (Relatores et al. in preparation).

We also include 16 galaxies from the HyperLEDA catalog[2] that satisfy these conditions. The heterogeneous nature and quality of HyperLEDA data generally do not affect the selection of galaxies in our sample because we verified the galaxy properties with the data in NED and WISE. The final list of selected targets is shown in Table 1. Distributions of several key properties of the target galaxies are displayed in Figure 3.1. The samples consists of mostly late-type spiral galaxies (Sbc-Sm) with linear diameters of 10-15 kpc and typical dynamical masses $M_{dyn} = v_{rot}^2 R/G \approx 10^{10} M_{\odot}$, where v_{rot} is the maximum inclination-corrected rotational velocity obtained from HyperLEDA, and R is the linear diameter.

3.2 Observations

To ensure both sufficient resolution and S/N, the galaxies were each observed in the C, D and E configurations of CARMA. The array consisted of nine 6.1-m diameter telescopes and six 10.4-m diameter telescopes with single-polarization SIS receivers for the 3-mm band. All observations were set up for the ^{12}CO ($J = 1 \rightarrow 0$) spectral line (rest frequency: 115.271 GHz) and were single-pointing observations. The CARMA primary beam has a half power diameter of ~ 2 arcmin. Three bands, each of which had a width of 62 MHz, 255 channels and a channel width of ~ 0.65 kms^{-1} (~ 0.25 MHz), were slightly overlapped to cover the entire signal. The combined velocity extent of the three bands was 410 kms^{-1}.

The gain and phase of the array were calibrated by observing a nearby quasar for 3 minutes every 15 minutes. The quasar typically had spectral flux density of ~ 1 Jy to provide sufficiently good calibration for our observations with three 62 MHz bands. Systemic calibration errors were minimized by selecting a quasar close to the target galaxy (typically within 20 degrees). The flux density scale (Jy/K) was determined from planetary observations (Mars, Uranus, Neptune) or observation of a bright source (e.g., MWC 349). The history of calibrator fluxes was maintained in the MIRIAD reduction software package. The calibrators were automatically determined by the CARMA observing tools when observing scripts were prepared using the CARMA system. Data collection for the project began in April 2013 and finished in March 2015 with over 600 hours at CARMA. Table 3.1 shows the integration time in each array configuration for the galaxies.

3.3 Data Reduction

To reduce the CARMA data, we used the INVERT, CLEAN and RESTOR algorithms in the MIRIAD reduction package. In short, INVERT generates a spectral line cube from the visibilities; CLEAN deconvolves the dirty (synthesized) cube and dirty (synthesized) beam to produce a model of the deconvolved cube, which has only the clean components; the output of CLEAN is then used by RESTOR to produce a clean map of the observed target. For each target, the data were obtained in several datasets, which were calibrated individually; then,

[2]The HyperLEDA catalog is on the web at http://www-ob.univ-lyon1.fr

Table 3.1: Integration time in each CARMA array configuration of the dwarf galaxies

name	C array (h)	D array (h)	E array (h)
NGC 746	0	7.2	0
NGC 853	6.5	17.5	0
NGC 949	10.1	15.8	9.5
NGC 959	7.3	6.2	0
NGC 1012	6.5	18.0	0
NGC 1035	8.4	16.6	6.4
UGC 3371	0	3.5	0
UGC 4169	0	4.1	0
NGC 3622	11.0	3.2	0
NGC 4150	23.0	31.7	4
NGC 4310	16.0	6.5	15.0
NGC 4376	9.2	7.3	0
NGC 4396	10.5	8.6	3.0
NGC 4451	7.0	10.4	0
NGC 4632	12.5	18.4	0
NGC 4701	7.2	16.0	0
NGC 5204	7.4	32.3	0
UGC 8516	0	6.4	0
NGC 5303	5.8	15.7	0
NGC 5692	10.2	22.5	0
NGC 5949	6.8	17.8	0
NGC 6106	6.5	7.2	17.1
NGC 6207	11.3	29.3	0
UGC 11891	9.5	4.0	0
UGC 12009	7.7	24.7	0
NGC 7320	18.7	7.0	0

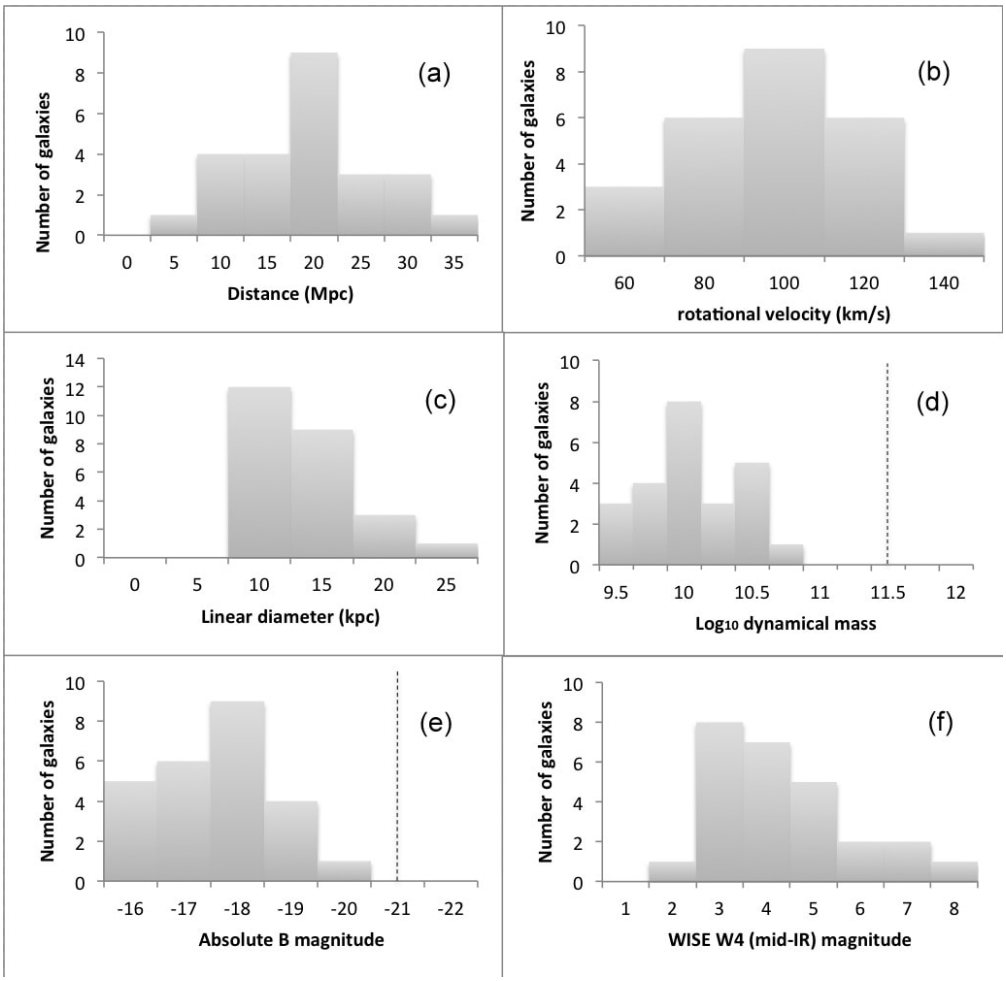

Figure 3.1: Summary of various properties of the galaxies targeted with CARMA in our survey: (a) distance (measured in Mpc); (b) rotational velocity (km s^{-1}); (c) linear diameter (kpc), using the distances from (a) and major diameters (arcmin) from NED; (d) $\log_{10}$ of the dynamical mass ($M_\odot$), $M_{dyn} = v_{rot}^2 R/GM_\odot$, with v_{rot} from (b); (e) absolute blue magnitude; (f) WISE w4 mid-infrared magnitude. The black dotted lines in (d) and (e) indicate the appoximate values for the Milky Way.

different datasets of the same target were reduced together to produce the final intensity (moment-0) and velocity (moment-1) maps. The resulting naturally weighted maps had average synthesized beams of $\sim$ 3.5" $\times$ 3", which corresponds to a physical resolution of 339 $\times$ 291 pc at a distance of 20 Mpc. The input visibility datasets had an average rms of $\sim$ 2.6 mJy beam^{-1} and a velocity resolution of $\sim$ 0.65 km s^{-1}. Using the INVERT algorithm, the input spectral channels in the uv datasets are resampled at equal increments of 10 kms^{-1} with their weighted average to produce the image data cube. Negative-value pixels were clipped, and masking (using the IMMASK algorithm) was applied to reduce the

noise in the moment maps and enhance the map clarity.

Furthermore, we calculated the velocity and velocity uncertainties per pixel in the moment-1 map using the Matlab code described by Bolatto, A.D. et al. (2002) and Simon, J.D. et al. (2003). Both velocity and velocity uncertainty are necessary data for the rotation curve fitting programs, which we apply in 4.2. The velocity uncertainty was calculated from straightforward error propagation and is expressed as follows:

$$dv = \frac{rms}{m0} \times \sqrt{\sum_{i=1}^{n}(v_i - m1)^2} \tag{3.1}$$

where n is the number of velocity channels in the data cube; v_i is the value of each velocity channel; $m0 = \sum_{i=1}^{n} s_i$ and $m1 = \sum_{i=1}^{n}(v_i s_i)/m0$ are the common moment 0 and moment 1 of the data cube, with s_i being the intensity of each pixel at velocity channel v_i.

Stringent constraints based on the rms and velocity range of the signal were applied in the algorithm to mask the pixels that would contribute mostly noise. In the data cube, we only used pixels with intensity $> 2.5 \times rms$ to isolate the signal in the spectrum. The velocity range of the emission was typically within ± 100 kms^{-1} of v_{sys}.

Figure 3.2 (p.27) shows the CO integrated intensity (whose values are denoted by the white contours) and velocity gradient of the targets with good CO detections. Among the 26 observed targets, 14 were detected in our measurements, 6 of which were detected in a previous CO single-dish measurement by Leroy, A.K. et al. (2005). Two of the 12 undetected galaxies in our sample were detected in Leroy, A.K. et al. (2005) (NGC 959 and NGC 4396), which might be due to the conditions of our observations: bad weather conditions on the observing days for these two targets, which reduced the amount of usable data; few hours of observation time (after the preliminary run, we increased the observing time for targets with clear signal by reallocating the time from targets with low or no signal), etc. Figure 3.3 (p.28) shows the velocity maps of the same targets after masking was applied, where the CO distributions appear much clearer with less noise. Note that several targets appear to have patchy CO distributions: NGC 853 has a hole in the center; NGC 1012, NGC 4701, NGC 4632, NGC 5303, NGC 5692 and NGC 5949 have a continous distribution for up to only $\sim$ 5" from the center; (NGC 853, NGC 949, NGC 4451, NGC 6106 and NGC 6207 have a patchy ring of CO); NGC 4150 has a notably small CO extension of only $\sim$ 10" in radius compared to the others. In Figure 3.4 (p.29), we show the CO contours overlaid on r-band optical images. All r-band imaging data were taken with SPICAM on the ARC 3.5m telescope at Apache Point Observatory (APO) on the nights of March 5 2014 and November 27 2014 (Relatores et al., in preparation), with the exception of NGC 4150 and NGC 4310: for these two galaxies, we used the r-band images in the SDSS III archive.

Figure 3.5 (p.31) shows the spectra of the detections at the central position. The heliocentric radial velocities derived from optical and radio (mostly HI) measurements are shown with vertical dotted and solid lines, respectively (these velocities were obtained from the hyperLEDA catalog). The range of maximum rotation velocity corrected for inclination is shown as the shaded region; this value was taken from the hyperLEDA catalog, which used

the HI 21-cm line width W_{20} and Hα rotation curves when available. The kinematic local-standard-of-rest (LSR) velocity (from NED) is shown with the vertical dashed lines. The systemic velocity as determined by MIRIAD from the CO data (Figure 3.3) is also shown with the vertical dash-dot lines. The spectra were obtained at only the central position in the images using the algorithm MBSPECT in MIRIAD. We note that NGC 853, which has a hole in the center, exhibits a noisy spectrum.

The signals of the other galaxies fall within the corresponding HI line widths, which fall within the velocity extent of our observing windows. There are two exceptions: (i) NGC 4150 had no recorded rotation velocity in the catalog; (ii) NGC 5949: its recorded optical systemic velocity is almost 150 km s^{-1} greater than its recorded radio systemic velocity in HyperLEDA. The HyperLEDA optical v$_{sys}$ is likely an erroneous value because: (1) our measured v$_{sys}$ of NGC 5949 is 412 kms^{-1} (Figure 3.3), which is close to the HyperLEDA radio v$_{sys}$, and (2) for this galaxy, Adams, J.J. et al. (2014) found a heliocentric v_{sys} of 440 kms^{-1} from fitting optical spectroscopy data.

3.4 Results & Discussion

With the CARMA observations, we detected CO in 14 galaxies, 8 of which had not been previously detected in CO in the literature, as shown in Table 3.2. Considering that past rotation curve studies had CO data for only 3 galaxies (NGC 2976, NGC 4605, and NGC 5963, Simon, J.D. et al. (2005)), our dataset will significantly increases the sample size of CO rotation curves that are adequate to accurately measure the dark matter distribution in dwarf galaxies, which is the main goal of our survey. To verify the reliability of our results, we will compare our results with past measurements (3.4.1) and show that we obtained consistent CO fluxes with Leroy, A.K. et al. (2005). In addition, we will show that there is a correlation between the CO flux and the IR flux, as we expected in our target selection (3.1).

Tables 3.2 and 3.3 summarizes the survey results for 26 galaxies observed with CARMA, including non-detections. Column (1) lists the galaxy names; column 2 shows the size of the synthesized beam in arcsec; column (3) shows the average rms over the entire image excluding the source emission; column (4a) is the total CO flux density (Jy beam^{-1} km s^{-1}) with 1σ error bar for the detected targets, or 3σ upper limit for the non-detected targets. The error bar was calculated as follows:

$$\sigma = rms \times \sqrt{N} \tag{3.2}$$

where rms is the average rms, and N is the number of synthesized beams per target. Information about the rms value and size of the synthesized beam are determined using the MIRIAD commands IMSTAT and IMLIST.

Columns (4b-5) and (2-4) in Tables 3.2-3.3 are intended for comparison between our results and literature results in terms of both CO measurements and infrared measurements.

Table 3.2: CO flux of the galaxies as measured at CARMA

name	syn. beam (arcsec^2)	rms (Jy/beam km/s)	F_{CO} (Jy/beam km/s)	F_{CO} (K km/s)	I_{CO} in ref. (K km/s)
(1)	(2)	(3)	(4a)	(4b)	(5)
NGC 746	4.04 × 3.23	0.983	< 77.0	< 1.06	-
NGC 853	5.09 × 3.97	0.516	216 ± 9.62	3.67	-
NGC 949	4.48 × 4.08	0.560	248 ± 13.9	4.11	1.87
NGC 959	2.77 × 2.22	0.634	< 82.5	< 1.39	0.86
NGC 1012	3.35 × 2.85	0.297	239 ± 9.56	3.66	1.5
NGC 1035	3.8 × 3.29	1.36	485 ± 30.5	10.1	-
UGC 3371	4.38 × 3.83	6.43	< 1150	< 2.4	< 0.58
UGC 4169	5.45 × 4.88	0.715	< 24.8	< 0.80	-
NGC 3622	2.06 × 1.63	0.759	< 72.2	< 2.20	-
NGC 4150	3.32 × 2.82	0.498	218 ± 18.7	3.60	2.38
NGC 4310	6.48 × 5.53	1.60	52.1 ± 26.0	1.14	3.31
NGC 4376	2.84 × 2.49	0.565	< 42.9	< 1.30	-
NGC 4396	2.63 × 2.29	0.528	< 70.4	< 1.70	2.37
NGC 4451	3.37 × 3.24	0.747	336 ± 16.6	5.35	-
NGC 4632	3.17 × 2.87	0.480	399 ± 18.4	6.96	-
NGC 4701	3.6 × 3.07	0.553	274 ± 24.2	4.90	4.85
NGC 5204	3.59 × 2.99	0.545	< 116	< 1.36	< 0.78
UGC 8516	4.32 × 3.38	1.20	< 53.1	< 1.62	-
NGC 5303	3.45 × 2.85	0.542	458 ± 6.87	7.60	-
NGC 5692	3.45 × 3.32	0.370	251 ± 5.25	3.88	-
NGC 5949	3.71 × 3.07	0.439	214 ± 11.7	3.48	1.86
NGC 6106	3.56 × 3.38	0.702	280 ± 22.7	5.19	-
NGC 6207	3.55 × 2.99	0.322	554 ± 11.7	8.90	-
UGC 11891	4.12 × 3.41	1.57	< 276	< 4.06	-
UGC 12009	2.24 × 1.77	0.694	< 62.1	< 0.63	-
NGC 7320	2.14 × 1.99	0.705	< 95.6	< 2.91	-

Note. — Column (2) is the synthesized beam size.
Column (4a) is the CO flux density $\pm 1\sigma$ (detection) or the limit of detection ($< 3\sigma$) (non-detection); column (4b) is the equivalent CO flux density for a single-dish measurement.
Column (5) (I_{CO}) is the CO integrated intensity corrected for the main beam efficiency, obtained from Leroy et al. (2005) when data are available.

Table 3.3: NIR and IR flux of the galaxies to compare with the CO flux measured at CARMA

name	F_{100} (Jy)	m_{Vega}	F_{22} (Jy)	M_{mol} $10^8 M_\odot$	M_{dyn} $10^9 M_\odot$	L_R $10^9 L_{r,\odot}$
(1)	(2)	(3)	(4)	(5)	(6)	(7)
NGC 746	1.632	7.095	0.0121	< 0.35	2.59	0.93
NGC 853	4.289	4.345	0.1529	3.02	3.65	3.02
NGC 949	7.56	4.578	0.1234	0.56	6.72	2.29
NGC 959	2.709	6.037	0.0322	< 0.24	4.26	1.02
NGC 1012	8.464	3.932	0.2236	0.72	14.0	4.47
NGC 1035	11.12	4.361	0.1506	2.77	19.3	3.47
UGC 3371	-	8.721	0.0027	< 1.96	14.5	1.66
UGC 4169	1.903	6.664	0.0181	< 2.83	18.6	5.37
NGC 3622	2.772	5.835	0.0386	< 0.81	6.33	3.98
NGC 4150	2.67	5.244	0.0668	0.15	-	-
NGC 4310	2.92	5.540	0.0509	0.23	4.49	-
NGC 4376	1.429	6.639	0.0185	< 0.22	3.53	1.70
NGC 4396	5.79	6.176	0.0283	< 0.22	13.6	1.35
NGC 4451	5.17	4.939	0.0885	8.30	18.6	6.31
NGC 4632	11.18	4.796	0.1009	3.01	22.5	5.01
NGC 4701	7.83	4.542	0.1275	1.67	16.4	3.39
NGC 5204	7.36	7.168	0.0113	< 0.06	2.65	3.72
UGC 8516	1.563	6.385	0.0233	< 0.37	3.15	2.04
NGC 5303	6.54	4.150	0.1830	2.73	6.15	3.63
NGC 5692	2.742	5.067	0.0786	7.71	9.16	4.68
NGC 5949	6.11	5.949	0.0349	0.99	9.21	2.57
NGC 6106	5.241	5.888	0.0369	6.15	37.9	7.08
NGC 6207	12.23	4.232	0.1696	14.2	26.8	4.68
UGC 11891	3.899	9.226	0.0017	< 0.87	9.67	1.58
UGC 12009	1.981	5.142	0.0734	< 0.46	9.09	1.82
NGC 7320	1.899	8.055	0.0050	< 1.43	9.50	2.57

Note. — The F_{100} values in column (2) were obtained from http://ned.ipac.caltech.edu.
Column (3) is the Vega magnitude of the galaxies, obtained from the WISE All-Sky Source Catalog for band w4.
Column (4) is the 22-micron flux, which was calculated as follows: $F_{22} = 8.363 \times 10^{-m_{Vega}/2.5}$.
Column (5) shows the molecular mass of the CO-detected galaxies, which was calculated from the CO flux in column (4b) in Table 3.2 assuming the galactic CO-to-H_2 conversion factor with the effect of helium.
Column (6) shows the dynamical mass, which was calculated from the rotational velocity in Table 1 as: $M_{dyn} = v_{rot}^2 R/GM_\odot \approx 10^{10} M_\odot$.
Column (7) shows the r-band luminosity, which was obtained from the observations with SPICAM on the ARC 3.5m telescope at Apache Point Observatory (Relatores et al., in preparation). Median values: $M_{mol}/M_{dyn} \approx 0.035$ and ≈ 0.010 for the CO detections and non-detections, respectively; $M_{mol}/L_r \approx 0.078 M_\odot/L_{r,\odot}$ and $\approx 0.024 M_\odot/L_{r,\odot}$ for the CO detections and non-detections, respectively.

Column (5) of Table 3.3 shows the molecular gas content in terms of mass in the CO-detected targets.

3.4.1 Flux comparison

First, for the single-dish-interferometer CO comparison, column (4b) of Table 3.2 shows the single-dish-equivalent CO flux from our observations in K km s^{-1}; column (5) shows the integrated CO flux (I_{CO}) from past single-dish observations (Leroy et al., 2005) of our targets where available. The single-dish-equivalent CO flux from our observation in K km/s was obtained as follows:

$$F[\text{K km/s}] = F[\text{Jy/beam km/s}] \times c_{K/Jy} \times \frac{A_b}{\pi(55/2)^2} \tag{3.3}$$

where $c_{K/Jy}$ is the K/(Jy/beam) conversion factor, A_b is the synthesized beam area (in arcsec^2, column (2) in Table 3.2) and 55 arcsec was the half-power beam width of the Leroy, A.K. et al. (2005) measurements, which were single-dish observations at 115.27 GHz using the ARO Kitt Peak 12-m telescope. $c_{K/Jy}$ and A_b were obtained from our moment-0 maps using IMSTAT and IMLIST; $c_{K/Jy}$ varies for different targets with a median value of ~ 8.4, independently of the clipping levels, whereas F and rms depend on the clipping levels in the maps. Despite the patchy CO distribution of the targets in Figure 3.2, for simplicity, we assumed that the entire signal was evenly distributed in the equivalent area of the single-dish beam to calculate the single-dish-equivalent flux. In general, some of our flux values are ~ 2 times larger than the values of Leroy, A.K. et al. (2005). This difference can be explained by our larger primary beam compared to the single-dish primary beam, which would contain more CO signal (if not the entire CO signal) of the larger sources.

Second, for the CO-infrared comparison, columns (2) and (4) of Table 3.3 show the corresponding IRAS 100-micron flux density and WISE w4 (22-micron) Vega magnitude, which we obtained from NED and WISE All-Sky Source Catalog, respectively. We converted the WISE w4 Vega magnitude (m_{Vega}) into the 22-micron flux density (in Jansky) using the following formula:

$$F_{22} = F_{w4-0} \times 10^{-m_{Vega}/2.5} \tag{3.4}$$

where $F_{w4-0} = 8.363$ Jy (Jarrett, T. H. et al. (2011)). Jarrett, T. H. et al. (2011) mentioned that the magnitude-flux conversion for the w4 band may require an additional red-source correction due to a discrepancy between red- and blue-source measurements. However, because our sources do not span a wide range of optical colors, we assumed that such discrepancy would be uniform among our sources, and we therefore did not apply the w4 correction for red sources. The red-source correction, if applied, would only change all values in our list by a constant factor close to unity.

In Figure 3.6 (p.32), we plot the 100- and 22-micron flux densities (F_{100} and F_{22}) of the observed galaxies with their respective CO flux (or the 3σ upper limit for non-detections)

from our measurements. In general, the galaxies with high F_{100} are detected in CO and have high CO flux, with some exceptions: NGC 4310, NGC 4150, and NGC 5692 (low F_{100} but detected in CO), and NGC 4396, NGC 5204 and UGC 11891 (high F_{100} but undetected in CO). We used the function *cenken* in the R/CRAN package (Helsel (2005), Akritas, M.G. et al. (1995)) to establish the existence of a correlation between F_{100} and CO flux (including the upper limits) and found:

$$I_{CO} = 54.09F_{100} - 77.77 \tag{3.5}$$

Conversely, $F_{100} = 0.01I_{CO} + 1.49$, where I_{CO} is measured in Jy/beam km/s and F_{100} in Jy, with a Kendall τ correlation coefficient of 0.45 (the p-value is less than 0.05).

Overall, the linear correlation is reasonable because the far-IR region corresponds to the central region of the galaxies with cold molecular clouds. The correlation between F_{22} and I_{CO} follows the same trend: the galaxies with high F_{22} generally have high CO flux, with the only exception of UGC 12009 (high F_{22} but undetected in CO). However, some galaxies with significantly higher mid-IR flux (compared to the others in the sample) have low CO flux, such as NGC 853 and NGC 1012, whereas NGC 4310 is detected in CO despite its small IR flux value. Again, using the function *cenken*, we found:

$$I_{CO} = 3.45 \times 10^3 F_{22} - 30.89 \tag{3.6}$$

Conversely, $F_{22} = 2.50 \times 10^{-4} I_{CO} + 1.59 \times 10^{-2}$, where I_{CO} is measured in Jy/beam km/s and F_{22} in Jy, with a Kendall τ correlation coefficient of 0.50 (the p-value is less than 0.05). Thus, compared to the far-IR flux, the mid-IR flux appears to be a better indication of whether a galaxy contains sufficient CO for detection at our level of sensitivity, but not necessarily a better indication of how much CO there is in the target. Note that in the original sample selection, we chose our targets partially based on the WISE mid-IR images and not the F_{100} values, so it is not surprising that the correlation between F_{22} and I_{CO} is better than that between F_{100} and I_{CO} in our sample. Nonetheless, this correlation could prove to be useful in future studies to help selecting other targets for CO observations.

3.4.2 Molecular gas content

We calculated the mass of molecular gas in the CO-detected targets from the CO flux, and the results are shown in column (5) of Table 3.3. Assuming the galactic CO-to-H_2 conversion factor [$X_{CO} = 2 \times 10^{20}$ cm^{-2} (K km s^{-1})$^{-1}$; Strong, A.W. & Mattox, J.R. (1996)] and following the derivation in Leroy, A.K. et al. (2005), we have: 1 K km s^{-1} is equivalent to a molecular surface density of $\Sigma = 4.4\cos(i) M_\odot$ pc^{-2}, which includes both H_2 and helium, where i is the inclination of the galaxy. A few dwarfs in our survey have relatively large M_{mol} (up to $10^9 M_{sun}$). We note that the Milky Way has a molecular mass on the order of $\approx 10^9 M_{sun}$ (Dame (1993)). In comparison, the dwarfs in Leroy, A.K. et al. (2005) had molecular mass on the order of $10^8 - 10^{10} M_{sun}$. However, the median molecular mass of our

galaxies is $\sim 2.75 \times 10^8 M_\odot$, which is consistent with the median molecular mass of dwarf galaxies in Leroy, A.K. et al. (2005) survey ($(3 \pm 0.5) \times 10^8 M_\odot$).

We compared the molecular mass with the dynamical mass and r-band luminosity, as shown in Figure 3.7 (p.33). The dynamical mass was calculated from the HI-derived rotational velocity (M_{dyn} in 3.1), and the r-band luminosity was calculated from r-band observations (as mentioned in 3.3, Relatores et al., in preparation). In Figure 3.7, we included both the targets with CO detection and those without, where the molecular mass of the non-detection was calculated from the 3σ upper limits in Table 3.2. We also included the radii of the galaxies in the plots (shown as the bubble size).

Figure 3.7 shows that the galaxies with more dynamical mass and larger size generally contain more molecular gas, and the average $M_{mol}/M_{dyn} \approx 0.035$ for our sample. (For comparison, $M_{mol}/M_{dyn} \approx 0.037 \pm 0.007$ for dwarfs in Leroy, A.K. et al. (2005)) However, 3 of the 14 detected galaxies in our sample show large molecular content while being small and have correspondingly lower dynamical mass: NGC 853 ($r = 4.36$ kpc), NGC 5303 ($r = 3.84$ kpc), and NGC 5692 ($r = 4.32$ kpc). The CO non-detections are consistent with the same linear correlation between M_{mol} and M_{dyn} as the targets with CO detections, and the median upper limit on M_{mol}/M_{dyn} is 0.010 for the non-detections. Hence, the achieved depth of the observations was reasonable given expectations for the CO luminosity.

Figure 3.7 also shows a weak correlation between the r-band luminosity and the molecular mass, which implies that larger galaxies with higher stellar mass generally have larger molecular mass, as expected (assuming stellar mass-to-light ratios of ~ 1 Adams, J.J. et al. (2014)). Again, NGC 5692 ($r = 4.32$ kpc) has high L_R despite its small size. The median $M_{mol}/L_r \approx 0.078 M_{sun}/L_{r,sun}$ for the CO detections and $\approx 0.024 M_{sun}/L_{r,sun}$ for the non-detections. Leroy, A.K. et al. (2005) did not show any r-band correlation, but their ratio of molecular mass and K-band luminosity is similar to our M_{mol}/L_r, where $M_{mol}/L_K \approx 0.065 \pm 0.008 M_{sun}/L_{K,sun}$.

Applying *cenken* to the values in our sample, we found the following correlations:

$$M_{dyn} = 47.49 M_{mol} + 4.05 \times 10^9 \tag{3.7}$$

$$L_r = 6.77 M_{mol} + 1.78 \times 10^9 \tag{3.8}$$

$$M_{mol} = 8.21 \times 10^7 r - 2.68 \times 10^8 \tag{3.9}$$

with $\tau = 0.42, 0.51$ and 0.32, respectively, where M_{mol} and M_{dyn} are measured in $M_\odot$, L_r in $L_\odot$, and r in kpc. All correlations are statistically significant with $p < 0.05$.

There are no resolved HI data for most of our galaxies, so we cannot make an analogous $M_{mol} - M_{HI}$ comparison, but considering that our M_{mol}/M_{dyn} and M_{mol}/L_r are consistent with past observations, we can assume that $M_{mol} - M_{HI}$ should be $\sim 0.30 \pm 0.05$ (Leroy, A.K. et al. (2005)) for our galaxies. We can apply this value to calculate the atomic gas content for the rotation curves and mass modeling in the second part of our survey (Truong et al., in preparation).

Acknowledgments

We are grateful to Melvyn Wright and Richard Plambeck for their invaluable help with MIRIAD, and to the staff and observers at Owens Valley Radio Observatory (OVRO) and CARMA for their assistance with the observations. Support for CARMA construction was derived from the states of California, Illinois, and Maryland, the James S. McDonnell Foundation, the Gordon and Betty Moore Foundation, the Kenneth T. and Eileen L. Norris Foundation, the University of Chicago, the Associates of the California Institute of Technology, and the National Science Foundation. The CARMA development and operations were supported by the National Science Foundation under a cooperative agreement, and by the CARMA partner universities. This publication makes use of data products from the Wide-field Infrared Survey Explorer, which is a joint project of the University of California, Los Angeles, and the Jet Propulsion Laboratory/California Institute of Technology, funded by the National Aeronautics and Space Administration. This study was partially supported by the NSF grant No. 1140031.

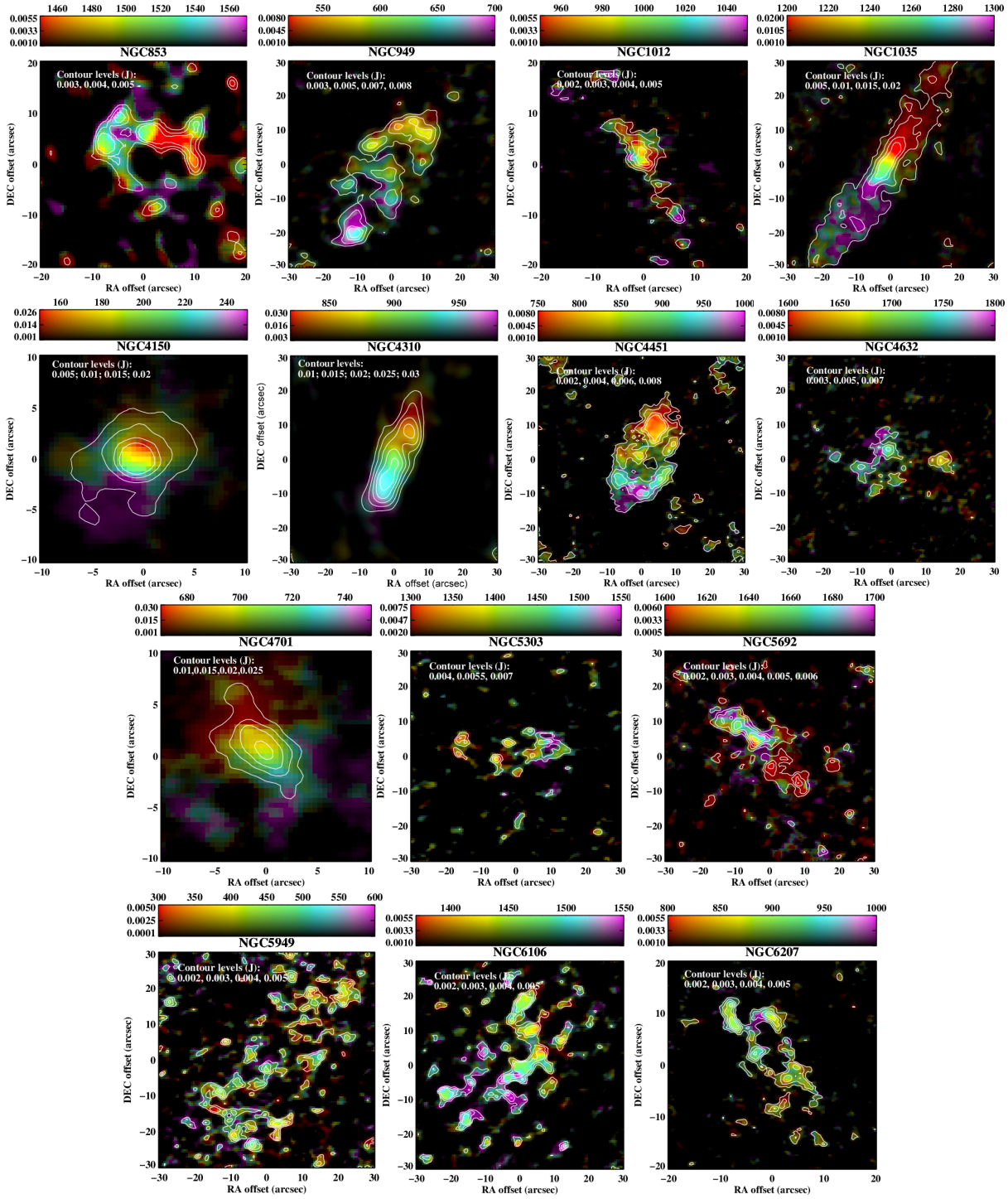

Figure 3.2: Naturally weighted CO(1-0) intensity and velocity distribution maps without masking of the CO-detected dwarf galaxies in the sample. The color bars indicate the velocity in km s^{-1} (gradient in the horizontal direction) and flux level in Jy (gradient in the vertical direction).

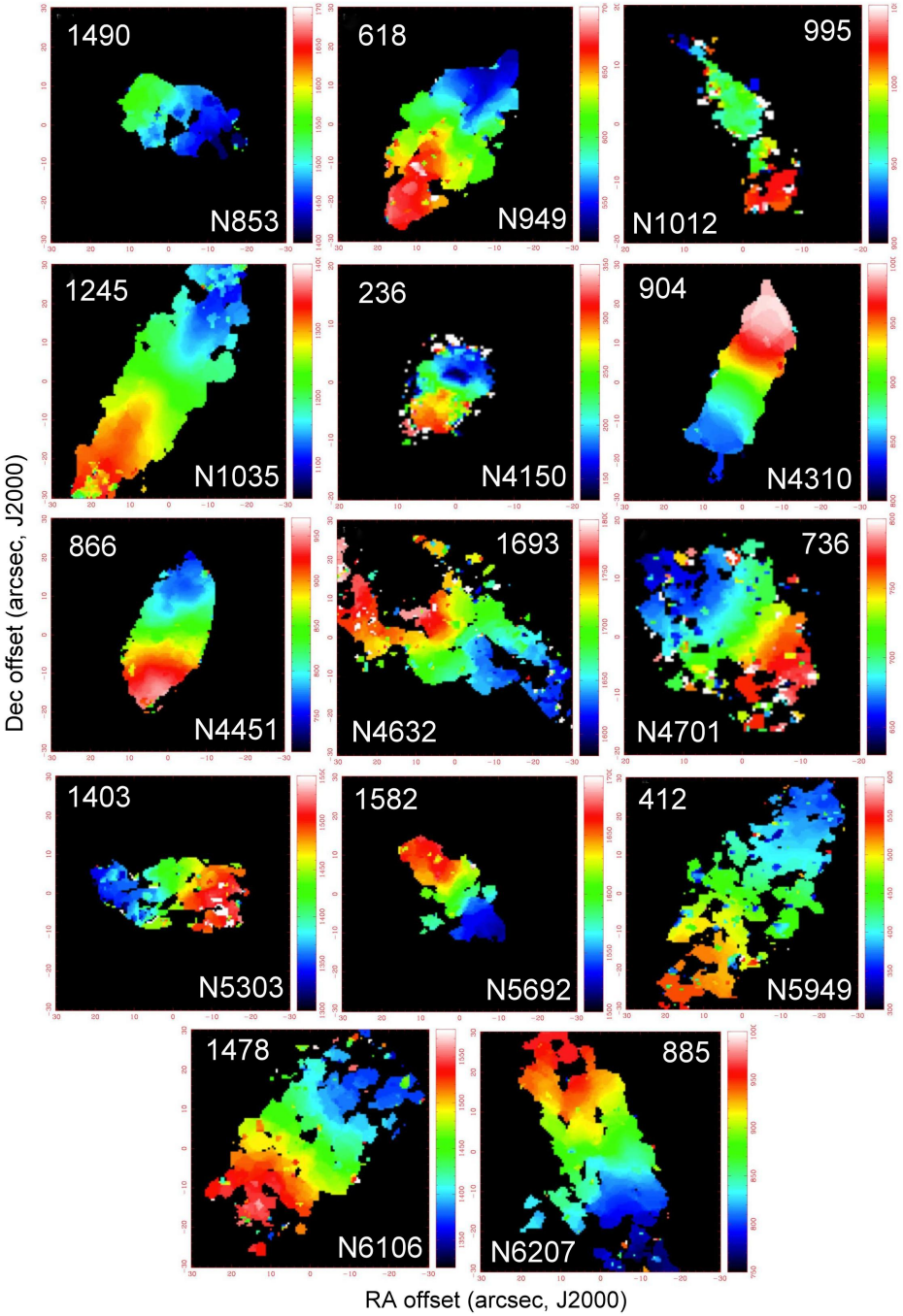

Figure 3.3: Naturally weighted CO(1-0) intensity and velocity distribution maps with masking to enhance the SNR. For all galaxies, the RA offset is from +30" (left) to -30" (right), the Dec offset is from -30" (bottom) to +30" (top); except for NGC 1012 and NGC 4150, whose RA and Dec offsets are from +20" to -20" and -20" to +20", respectively. The color bar on the right side of each image shows the velocity gradient; the number at the top corner is the systemic velocity.

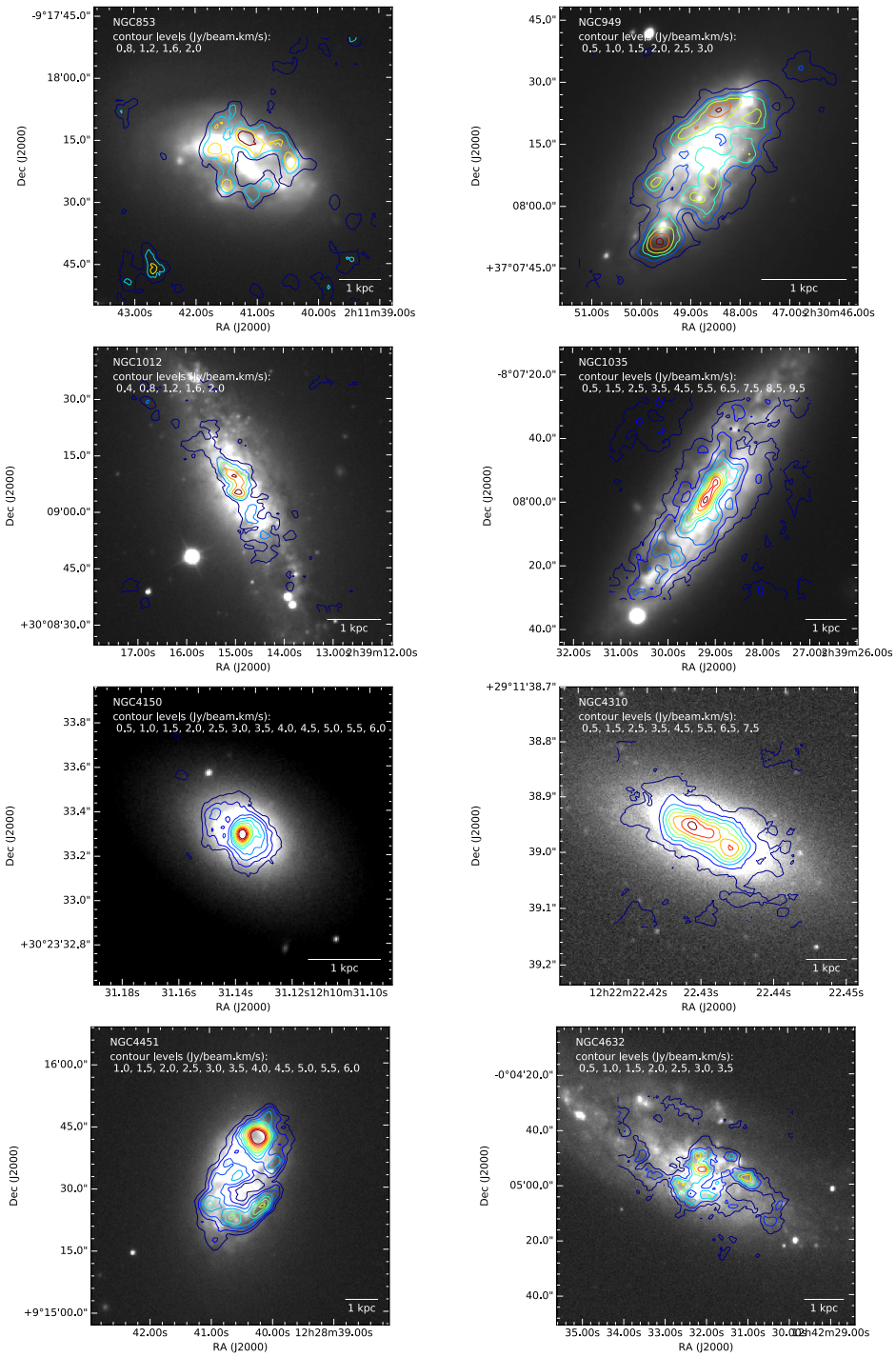

Figure 3.4: Contours of CO(1-0) intensity (CARMA data) on r-band imaging data, which were taken with SPICAM on the ARC 3.5m telescope at Apache Point Observatory. Exceptions: the r-band images of NGC 4150 and NGC4310 were obtained from the SDSS III archive.

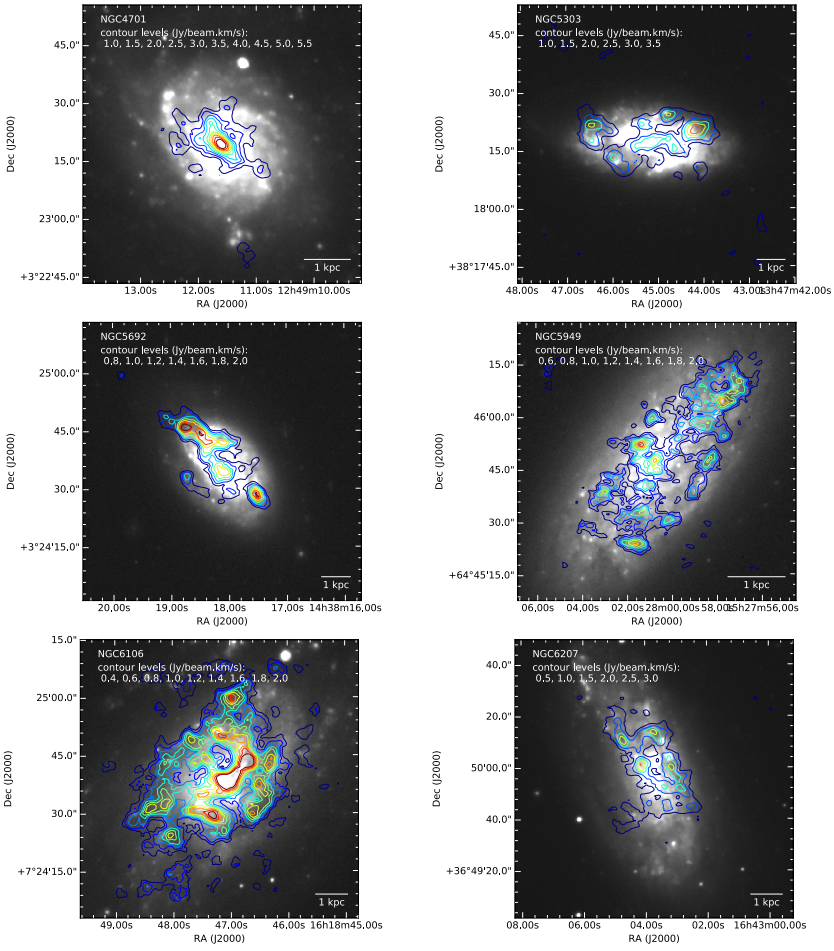

Figure 3.4: Contours of CO(1-0) intensity (CARMA data) on r-band imaging data, which were taken with SPICAM on the ARC 3.5m telescope at Apache Point Observatory. (cont.)

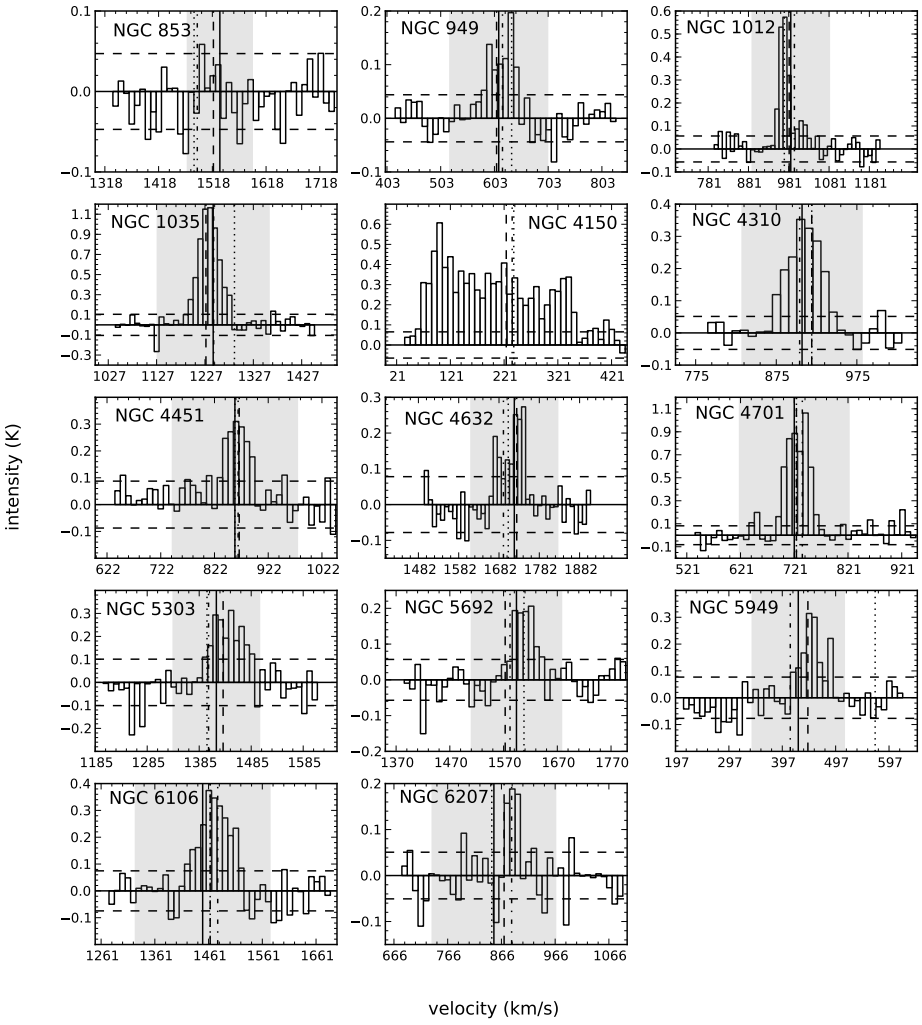

Figure 3.5: Spectra of detected galaxies from the survey at the central pixel in the image. The horizontal dashed lines indicate the rms noise; the vertical lines show the positions of the LSR (dashed), radio (solid), optical (dotted), and CO-data-based systemic velocities (dash-dot). The LSR, radio and optical velcities were obtained from NED and hyperLEDA. The shaded region shows the HI line width W_{20}. Note that NGC 853 has a hole in the center, hence the lack of a signal at the central pixel, and NGC 4150 has a broad linewidth that covers the entire velocity bandwidth and leaves no baseline, which may be due to it being an elliptical galaxy instead of a thin disk.

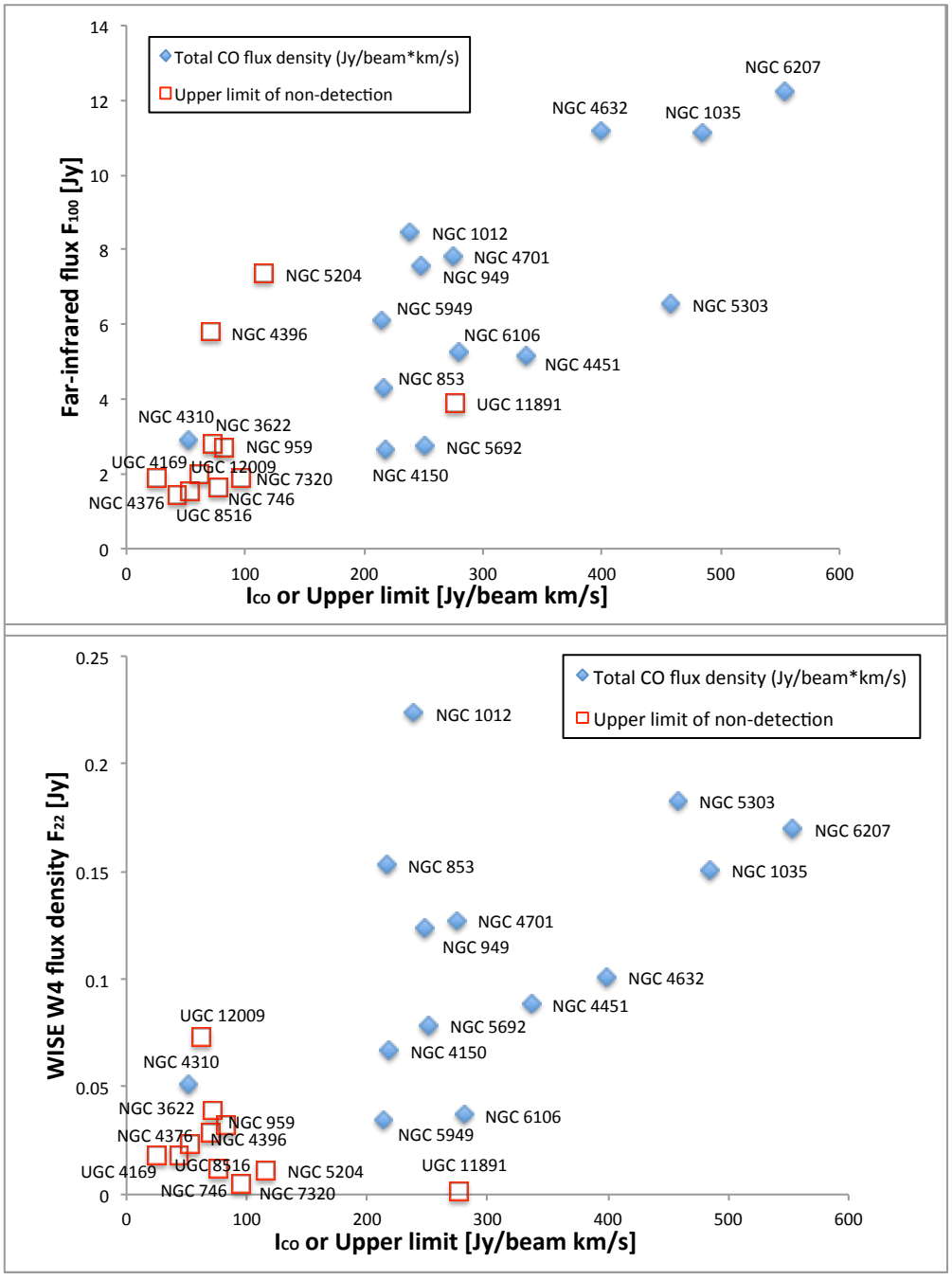

Figure 3.6: Correlation between the total CO flux of each target (or 3σ upper limit in the case of non-detection) and its corresponding $F_{100\mu m}$ and WISE w4 flux density $F_{22\mu m}$. $F_{100\mu m}$ was obtained from NED, and $F_{22\mu m}$ was converted from the Vega magnitude in band 4, which was obtained from the WISE All-Sky source catalog.

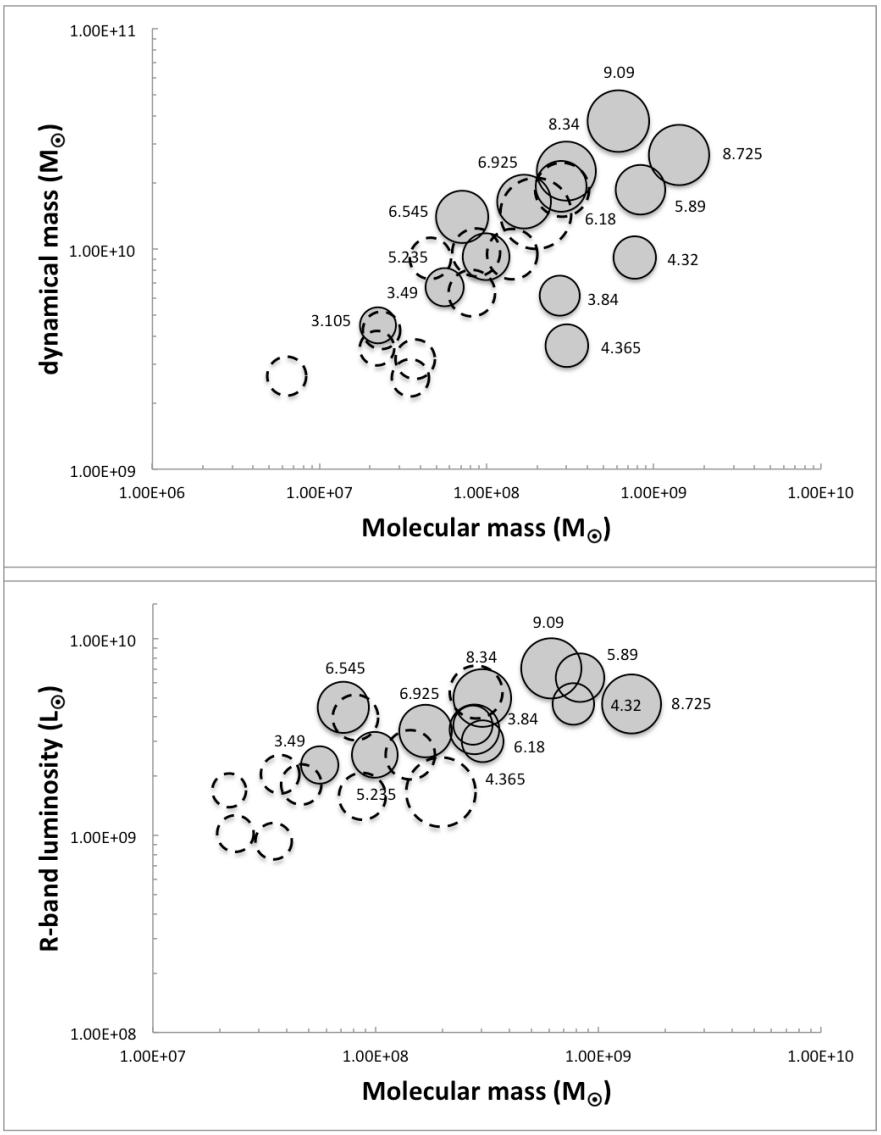

Figure 3.7: Correlations between the molecular mass, radius, and dynamical mass (top) and r-band luminosity (bottom) of the targets in the survey. The CO-detected targets are shown with filled circles, and the CO non-detections are shown with empty dashed circles. For the CO non-detections, the molecular mass was calculated from the 3σ upper limit (Table 3.2). The dynamical mass was calculated from the HI-derived rotational velocity; the r-band luminosity was obtained from r-band imaging at Apache Point Observatory (Relatores et al., in preparation). The size of the bubbles corresponds to the radius in kpc, whose value is the number shown next to the bubble. To avoid over-cluttering the image, we do not show the numerical values of the radii of the non-detections, which can be found in Table 1.

Chapter 4

Data Analysis, CO Rotation Curves and Mass Modeling

4.1 Data Analysis

In order to extract a rotation curve from the CO velocity fields obtained with CARMA (Truong et al, 2017), we used the publicly available code DiskFit (Spekkens, K. & Sellwood, J.A. (2007)), which can fit either axisymmetric or non-axisymmetric non-parametric models to velocity fields. DiskFit uses a χ^2 minimization method to determine the best fit values, and the galaxy geometric parameters in the model (position angle, ellipticity and galaxy center) are kept constant for all radii of the galaxies, with the assumption that the data are well represented by a thin disk, which should be correct for CO observations. As described by Reese, A.S. et al. (2007), Spekkens, K. & Sellwood, J.A. (2007) and Sellwood, J.A. & Sanchez, R.Z. (2010), DiskFit has two options of data fitting: a photometric option (fitting images) and a kinematic option (fitting velocity fields). The kinematic option of the code, which is VELFIT, is fundamentally different from ROTCUR (Begeman, K.G. (1989)), which derives kinematical parameters of a galaxy by fitting tilted-rings to its velocity field. This is because VELFIT fits physically motivated models, such as those with lopsided flow or bars in the galaxies, whereas ROTCUR simply parametrizes concentric rings in the velocity field.

As a check, we used another rotation curve fitting program named RingFit (Simon, J.D. et al. (2003)). Ringfit was written in Matlab to compare fitting results with ROTCUR, and it fits for radial motion (inflow and outflow) instead of assuming that the observed velocity is only due to circular rotation. DiskFit also allows fitting for radial motion, but it is one of many options instead of the only choice as in RingFit. For our purposes, the main relevant difference between DiskFit and RingFit is that RingFit keeps the geometric parameters of the galaxy (position angle, ellipticity and galaxy center) as fixed inputs, whereas DiskFit allows the position angle, ellipticity and center to be parameters in the fit, so that they are determined from the kinematic data. We will compare the results of DiskFit and RingFit in 4.1.3.

4.1.1 Fitting models

The velocity of a star or an element of gas in the plane of the disk of a galaxy can be described with two basic components: the tangential component and the radial component with respect to the kinematic center. The general equation for the kinematic models currently implemented in DiskFit is (Spekkens, K. & Sellwood, J.A. (2007), Kuzio de Naray, R. et al. (2012)):

$$\begin{aligned} v_{model} = v_{sys} + \sin i[V_t \cos\theta - V_{m,t} \cos(m\theta_b) \cos\theta \\ - V_{m,r} \sin(m\theta_b) \sin\theta] \end{aligned} \tag{4.1}$$

where v_{sys} is the systemic velocity, i is the inclination, V_t is the circular velocity, $V_{m,t}$ and $V_{m,r}$ are the tangential and radial components of non-circular flows with harmonic order m in the disc plane, θ and θ_b are the azimuthal angles relative to the major axis and non-circular flow axis (e.g., a bar), respectively.

Following Spekkens, K. & Sellwood, J.A. (2007), we assume that harmonic terms with $m > 2$ are negligible (Schoenmakers, R.H.M. et al. (1997)). When $m = 1$, the model describes a lop-sided flow; when $m = 2$, the model is bisymmetric and describes a barred or elliptical flow (Spekkens, K. & Sellwood, J.A. (2007)). When $m = 0$, the code can fit the data for models with or without radial flow, i.e.,

$$v_{model} = v_{sys} + \sin i[V_t \cos\theta - V_r \sin\theta] \tag{4.2}$$

for the radial-flow case, where V_t is the circular velocity, and V_r is the radial flow component, or:

$$v_{model} = v_{sys} + \sin i V_t \cos\theta \tag{4.3}$$

for the case without radial flow.

In our work, we considered all available models ($m = 0, 1, 2$ and radial flow) for our best datasets (NGC 1035 and NGC 6106) (more details are provided in 4.1.2), and we selected the case of $m = 0$ with radial flow to model the rotation curves of the remaining galaxies. In some cases, when the outer rings at the edge of the galaxies have insufficient data, the radial flow is excluded from the fit for those rings. Note that the outputs of both DiskFit and RingFit were inclination-corrected. The error bars were computed using 100 bootstrap resamplings in DiskFit (according to the uncertainty estimation procedure in Spekkens, K. & Sellwood, J.A. (2007)). The parameter selections are described in detail in 4.1.2. Regarding the velocity convention, we use radio velocity with respect to the local standard of rest.

4.1.2 DiskFit settings

As described by Reese, A.S. et al. (2007), Spekkens, K. & Sellwood, J.A. (2007) and Sellwood, J.A. & Sanchez, R.Z. (2010), DiskFit has two options for data fitting: a photometric option (fitting images) and a kinematic option (fitting velocity fields). The kinematic option of the code, termed VELFIT, differs from early velocity field modelling routines such

as ROTCUR (Begeman, K.G. (1989)), which derives kinematic parameters of a galaxy by fitting tilted-rings to its velocity field. This is because VELFIT fits physically motivated models, such as those with lopsided flow or bars in the galaxies, whereas ROTCUR simply parametrizes concentric rings in the velocity field.

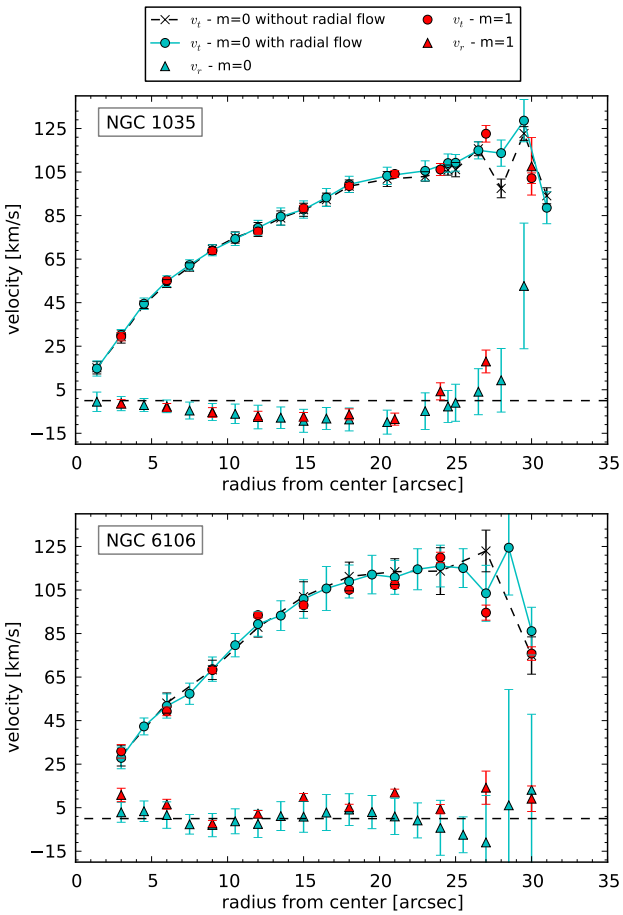

Figure 4.1: Rotation curves and residuals from the CO data of NGC 1035 and NGC 6106 using DiskFit in 3 cases: $m = 0$ with no radial flow (black crosses connected by a black dashed line); $m = 0$ with radial flow (cyan; tangential velocity [circles] and radial velocity [triangles]); $m = 1$, i.e., lop-sided model (red; tangential velocity [circles] and radial velocity [triangles]). The error bars were computed using 100 bootstrap resamplings.

In this work, we considered all available models ($m = 0, 1, 2$ and radial flow) for our best datasets (NGC 1035 and NGC 6106) to determine which model could best be applied for all galaxies (Figure 4.1). We observed the following:

- $m = 0$ (with and without radial flow): we set the radius increment to be 1.5 arcsec;

- $m = 1$: a 1.5-arcsec radius increment required a significantly longer time to complete the fitting, so we changed the radius increment to 3 arcsec. In the $m = 1$ case, for maps with low spatial resolution like ours, junc $= -1$ gives very large error bars after the resampling, whereas junc $= 1$ gives similar error bars to the $m = 0$ cases, as shown in Figure 4.1.

- $m = 2$: for completeness, we computed the $m = 2$ case, which is for bar structures. Note that the targets in our samples were selected to contain no visible bar, lopsided flow, or elliptical flow where possible, so we expect that the higher-order $m = 2$ terms will not be required to fit the velocity fields. Nonetheless, for the $m = 2$ case, DiskFit could not converge for any galaxy, most likely because of the small CO extent in the data set (only to ~ 30 arcsec).

Two important results are to be noted in Figure 4.1: (1) the radial components in all cases are consistently small ($\lesssim 10$ km s^{-1}, except at the outermost radii where there were no data over a large enough range in azimuth to constrain them); (2) the rotation curves in all three fitting cases have similar slopes, particularly in the inner radii. Because the rotation curves obtained using different models of the velocity field are consistent, we use the case of $m = 0$ with radial flow to model the rotation curves of the remaining galaxies.

Uncertainty estimation in DiskFit. The errors of the fit depend on the pseudo-velocity maps that DiskFit creates for the bootstrap resampling. The way that DiskFit creates the pseudo-velocity maps is determined by the parameter labelled "*junc*" in the input file: (i) for $junc > 0$, the residuals from the χ^2 minimization are randomly scrambled, so that the bootstrapped velocity field has the same noise properties as the input map; (ii) for $junc < 0$, the residuals are moved radially by a random amount. According to the DiskFit user manual, $junc = -1$ should be used if there are large-scale features (e.g., bars) in the velocity map and $junc > 0$ otherwise. We attempted various $junc$ values in our fitting, e.g., $junc = -1$ or $junc = 1$, which does not significantly change the result; thus, we selected $junc = 1$ for all galaxies, since .

Geometric parameters of the galaxies. Following Spekkens, K. & Sellwood, J.A. (2007), we assumed no warping because warps are rare for spiral-galaxy velocity fields within the optical radius. The input parameters of the fitting routines in DiskFit include: position angle, ellipticity, galaxy center, and systemic velocity. First, we estimated the center by eye, used the systemic velocity values in NED, and calculated the position angle and ellipticity using FIND_GALAXY[1] (Cappellari 2002) with the unmasked moment-0 maps of the galaxies. (Although FIND_GALAXY can also calculate the center, we found that compared to the estimated center, the calculated center more often made the fit unable to converge to a reasonable value, possibly because the calculated center is the coordinate of the brightest pixel, which may not be the geometric center.) To determine values of PA and ellipticity as accurately as possible, we used $10 - 60\%$ of the total number of pixels in the maps, as

[1]FIND_GALAXY is a publicly available Python routine in the MGE_FIT_SECTORS package by M. Cappellari (Cappellari, M. (2002)). It collects all pixels above a certain threshold and uses the luminosity-weighted moments to calculate the center, PA, and ellipticity.

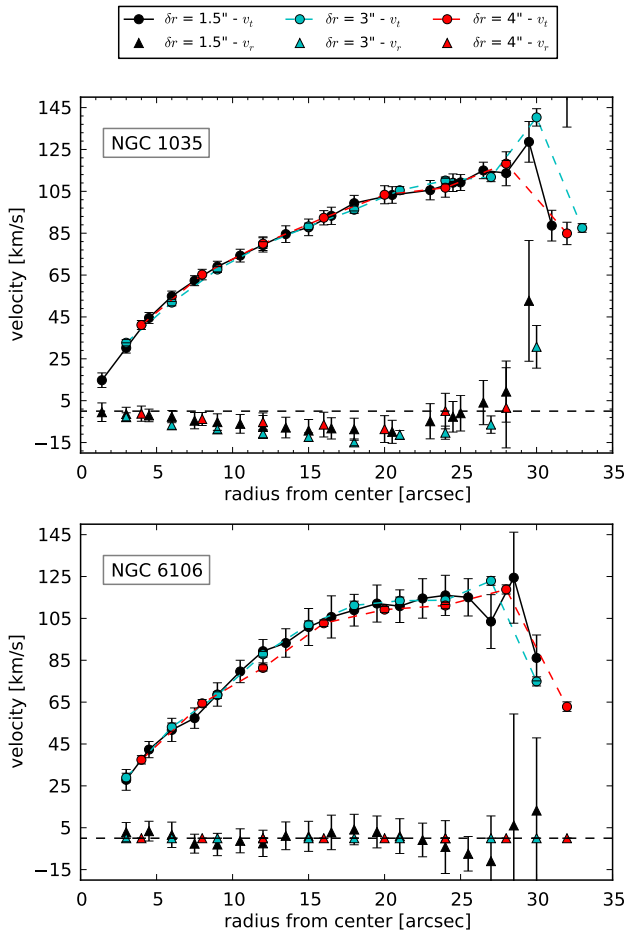

Figure 4.2: Rotation curves from CO data of NGC 1035 and NGC 6106 using DiskFit with three different ring widths: $\delta r = 1.5$ arcsec (black), 3 arcsec (cyan), and 4 arcsec (red). The model is $m = 0$ with radial flow.

suggested by the code documentation, because of the different sizes of our targets (higher percentages of pixels did not yield more accurate values). Then, the obtained parameters (from FIND_GALAXY) were used as the inputs of both RingFit and the first DiskFit run. For RingFit, as previously mentioned, these three parameters (PA, ellipticity and center) stay fixed for all rings throughout the fitting. However, for DiskFit, they can be adjusted during the fitting to minimize χ^2 and obtain the best fit. At the end of of each trial in DiskFit, a new (and possibly different) set of values with the best-fit velocities (v_{sys}, V_t and V_r) are the output of the trial. Then, these best-fitting output parameters (PA, ellipticity, center, and systemic velocity) were used as the inputs for subsequent trials until the output values were reasonably stable with reduced $\chi^2 < 1$. Typically, this process takes 2-4 iterations to converge.

For a dataset with N line-of-sight velocity measurements D_n with uncertainty ΔD_n, the goodness of fit at each point is determined by the following equations (Spekkens, K. & Sellwood, J.A. (2007)):

$$\chi^2 = \frac{1}{\nu}\sum_{n=1}^{N}\left(\frac{D_n - \sum_{k=1}^{K} w_{k,n}V_k}{\sigma_n}\right)^2 \tag{4.4}$$

$$\sigma_n = \sqrt{\Delta_D^2 + \Delta_{ISM}^2} \tag{4.5}$$

where ν is the number of degrees of freedom in the fit; K elements V_k are the tabulated velocity profiles in the model; the weights $w_{k,n}$ describe the interpolation from V_k to the modelled velocity at the position of the observed D_n; Δ_D is the uncertainty at each velocity value from the measurements, and Δ_{ISM} represents the amplitude of random motion that gets added in quadrature to the measurement errors. Δ_{ISM} can be increased to minimize χ^2 without affecting the output fitting values. In our work, we selected $\Delta_{ISM} = 5$ km s^{-1}. For our sample, the average reduced χ^2 of the fit is ≈ 0.2 because of the large measurement uncertainty in our observations. The uncertainties in the data, which were calculated using a bootstrap resampling from the moment maps, may have have been overestimated, but we currently do not have another method to calculate these uncertainties.

Ring size. In DiskFit, the velocity field is divided into concentric elliptical rings; we chose the width of each ring to be 3″ to have a reasonable number of rings to measure the rotation curve while ensuring that the ring width is approximately the beam size. As shown in Figure 4.2, changing the ring width does not affect the fitting results. For ring widths smaller, equal to or larger than the beam size, the obtained rotation curves have the same shape and only differ in the sampling (number of points in the curve).

We fitted both the tangential and radial components of the velocity (Eq. 4.3). As previously mentioned for NGC 1035 and NGC 6106, the uncertainty was estimated using 100 bootstrap resamplings.

Similarly, in RingFit, the velocity field is also divided into concentric elliptical rings, and we chose the smallest possible ring width that still allowed a reasonable fit for each galaxy and its beam size. The velocity uncertainties in the rotation curves were estimated using a Monte Carlo technique as described in Simon, J.D. et al. (2003).

Other settings in DiskFit. The reduced images have a pixel size of $0.33 - 0.50$ arcsec and the CO detections extend to at most ~ 30 arcsec from the center. DiskFit provides an option to reduce the sampling of the map at large radii, but we do not use this option in order to obtain stability in fitting for the angular resolution of our data, i.e., to make sure that the results converge despite small changes in the paramaters. We chose to sample the velocity field at every pixel after the first pixel (i.e., in the DiskFit input file, regrad = 1 and istepout = 1). Although our choice technically leads to oversampling the velocity field, because of the small number of independent points, the fitting results would lose stability otherwise (small variations in the input parameters lead to large variations in the fitting results). Other settings such as seeing/ beam smearing correction and model component

smoothing parameters were kept at the default values, i.e., no beam smearing correction was applied because DiskFit beam smearing correction cannot account for beam smearing effects that result from taking the moment of a datacube, which is the case of CO velocity fields. The model component smoothing was also not applied because it is only necessary when the best-fitting points in our rotation curve oscillate about a mean trend, and applying the smoothing did not improve the fit.

4.1.3 DiskFit vs. RingFit

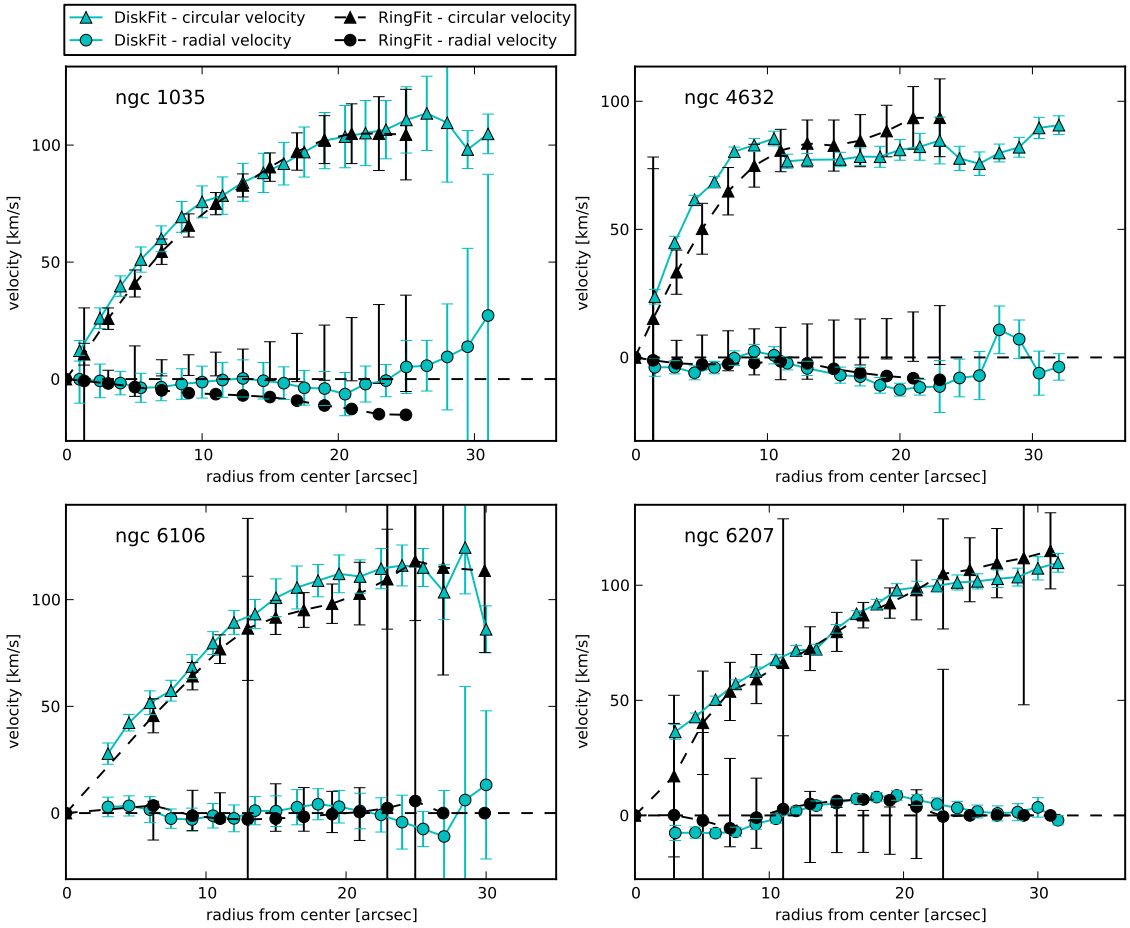

Figure 4.3: Comparison between DiskFit (cyan) and RingFit (black) results of the rotation curves of 4 galaxies, including circular velocity (triangles) and radial velocity (circles). The error bars were estimated using bootstrap (DiskFit) and Monte Carlo (RingFit) resamplings.

Figure 4.3 shows the rotation curves obtained using DiskFit (cyan) and RingFit (black) for 4 galaxies (the same procedure was performed for the remaining 10 galaxies, and the

conclusions are similar to those for the plotted objects).

We see that DiskFit and RingFit give similar rotation and radial velocities for each galaxy. Considering the entire rotation curves, DiskFit provides more regular uncertainty estimation than RingFit: the uncertainties at some radii in the RingFit curves are unusually large (possibly because of the patchy CO distribution at those particular radii), although their neighboring values are normal. Because the results of DiskFit and RingFit are consistent with one another, and considering the flexibility of DiskFit in terms of input parameters, we used DiskFit to derive the final rotation curves for this study.

4.2 Rotation Curve Fitting Results

In this section, we compare the kinematic center, ellipticity and PA to those estimated from optical or near-infrared imaging. Further details of the imaging data will be presented by Relatores et al. (in preparation). In brief, we use archival 4.5-micron images from IRAC on the Spitzer telescope for 10 of our 14 targets. For the remainder, we use r-band images obtained with SPICAM at the Apache Point Observatory. The center, ellipticity, and PA were generally measured using FIND_GALAXY, consistent with the methods used for the CO data, except for systems containing a clear nucleus, in which cases, the position of the nucleus was taken to be the center.

Table 4.1 provides the best fitting values of the systemic velocity, PA, ellipticity, inclination, and kinematic center of all 14 galaxies. The photometric results (reduced from r-band imaging data from APO and IRAC Channel-2 data, Relatores et al. in preparation) are included for comparison. Table 4.2 shows the rotation velocities at the maximum observed radii of the galaxies, and the correspondingly calculated dynamical mass at those radii. Figure 4.4 shows the comparison between the geometric parameters derived from the CO data and those from photometric measurements for the galaxies, where the parameters from the CO data were obtained from the rotation curve fitting using DiskFit, with either: (1) all initializations from CO data (circles) and a ring width of 1.5", or (2) photometric center as the initialization for the center (triangles) (the other parameters are initialized with CO data) and a ring width of 3". Hereafter, for simplicity, we will refer to the CO rotation curve results with all initializations from CO data simply as CO results, and the CO results with photometric centers as the initialization as the "photometric-CO" results. The difference in ring width should not significantly affect the shape of the rotation curves, as shown in 4.1.2. We observe that having the photometric center as the initialization does not significantly change the DiskFit result either, because as long as the center is not a fixed parameter, DiskFit will run until the result converges to the best-fit value. In addition, fixing the center to a specific value or letting it vary does not significantly change the fitting results.

Furthermore, the photometric PA and CO PA are consistent with each other for all galaxies in the sample. Although the photometric inclination and CO inclination are different by $\sim 9^\circ$ on average, the discrepancy does not harm our results because this difference will only change the rotation curves by a constant factor of $\sin(i + \Delta i)/\sin(i) = \cos(\Delta i) + \cot(i)\sin(\Delta i) \approx 1 + 0.15\cot i < 1.2$ for $\Delta i \approx 0.15$ and $i \geq 40^\circ$ (the bestfit inclinations of all galaxies in our sample are greater than 40°, see Table 4.1). This change does not significantly change the inner power-law slope of the difference between the observed velocity profile and the stellar velocity profile, which is our interest in the mass modeling. We also tried performing fits in which the ellipticity was fixed to the photometric value, but this also did not change the shape of the rotation curves. In terms of geometric center, the CO results and photometric results are consistent with each other to within $\sim 1''$ and are no more than $\pm 2''$ from the center of the images, with the exception of NGC 853 and NGC 4310.

The rotation curves of 14 galaxies with good CO detections are shown in Figure 4.5 with the corresponding moment-1 maps. The overlaid ellipses on the moment maps show the rings

that were used in DiskFit for the fitting. The overlaid ellipses help to verify by eye that the best fit parameters are reasonably consistent with the velocity distribution of the galaxies in consideration. The CO rotation curves, including both tangential velocity (triangles) and radial velocity (circles) components, were obtained with either purely CO inputs (dashed lines) or photometric input for the center (solid lines) in DiskFit. Note that the photometric center was only used for the initialization in DiskFit and not kept as a fixed value, unless noted otherwise in special cases (e.g., NGC 853). For 11 galaxies in our sample, we have obtained Hα rotation curves using the Cosmic Web Imager at Palomar Observatory. The analysis of the full Hα sample will be presented by Relatores et al. (in preparation). Here, we overlay the Hα rotation curves in Figure 4.5 to note their general consistency with the CO kinematics.

For NGC 853 and NGC 4150, neither DiskFit nor RingFit could provide any stable results using the previously stated procedure and settings. Thus, for completeness, we had to use the $m = 0$ model with no radial flow for these two galaxies (hence the zero radial-flow component in the rotation curve plot on the right) and keep some parameters in DiskFit fixed to the photometric values: the PA, ellipticity, and center were fixed for NGC 853, whereas the PA and ellipticity were fixed for NGC 4150. In addition, for NGC 1012 and NGC 5303, which have patchy CO distributions, to improve the fitting results, we limited the number of degrees of freedom in the fit by keeping the center fixed in DiskFit and using the $m = 0$ model with no radial term for the largest 1-2 rings, where the data are most scarce[2]. We note the following points in Figure 4.5:

1. All targets whose best-fit rotation curves could be obtained using DiskFit with the specified settings and procedure, except NGC 949 and NGC 4451, show a good fit to the radial-flow model with a small residual component.

2. The results indeed converge with the appropriate choice of input parameters (including the aforementioned radial binning) and were relatively stable for small variations of the initial guesses for PA, center, and ellipticity.

3. All galaxies (except NGC 853 and NGC 4150) show generally well-behaved rotation curves that are still rising at the last measured points. Several galaxies in the sample, such as NGC 1012, NGC 4310, NGC 4451, and NGC 5949, have classic, slowly rising rotation curves that suggest shallow density profiles, while other galaxies including NGC 949, NGC 1035, NGC 4632, and NGC 6106, exhibit much steeper central velocity gradients. We will compare the mass modelling results in 4.4 with these rotation curves to verify these predictions.

4. The tangential and radial components are consistent between the CO and Hα rotation curves for all galaxies, except NGC 949, NGC 4451, and NGC 5303 (the CO radial

[2]In Figure 4.5, the radial term of the largest 1-2 rings was kept in the fit for the CO rotation curve and removed for the photometric-CO rotation curves, which demonstrates the good behavior of the photometric-CO rotation curves in comparison because of this decrease in number of degrees of freedom.

component is smaller in magnitude than the Hα radial component for these galaxies), and importantly, the radial components are consistently low enough not to affect the estimates of the rotation velocity (except for NGC 4451). For NGC 949, NGC 4451 and NGC 5303, the differences between the Hα and CO curves are only the result of slightly different inclinations (Table 4.1 and will not affect the dark matter profiles in the end.

5. NGC 853 has a hole in the center as shown in the velocity map, whereas NGC 4150 has a very small CO extent (less than 20 pixels, i.e., $10'' \sim 0.7$ kpc, across). Inhomogeneous or incomplete CO coverage likely causes DiskFit to fail to produce a stable fitting result with a radial flow. For NGC 853, the photometric-CO rotation curve is consistent with the Hα rotation curve in the inner kpc and consistent with the CO curve starting from 1 kpc outward, because the photometric-CO curve had the same fixed geometric parameter initializations as the Hα curve, and the CO distribution is patchy, so the center cannot be well determined from the CO map. We do not have Hα data for NGC 4150 for comparison.

6. NGC 4451 has a large positive V_r term, which indicates that it has a significant non-axisymmetric component (a radial flow or a bisymmetric perturbation, e.g., a bar). As shown in A14, in some cases, both radial flow and bisymmetric models can give a good fit to the data and cannot be discriminated from each other.

7. Compared to the other galaxies, NGC 5692 and NGC 5949 have larger error bars in the CO rotation curves, but not the photometric-CO rotation curves. DiskFit did not converge to the minimum χ^2 with the CO-based initialization of the center, causing this difference in the curves.

Considering the patchy CO distribution for some galaxies, the high resolution of photometric data, and the consistency in DiskFit results, we will use the photometric-CO rotation curves for the mass modeling (Recall that the center, PA and ellipticity were allowed to vary, and the "photometric" term only refers to the initialization of the center in DiskFit).

Table 4.1: Best fitted parameters obtained from DiskFit using CO data and those obtained from photometric data

(1) Name	(2) data	(3) v_{sys} (kms^{-1})	(4) PA (deg)	(5) ϵ	(6) inc. (deg)	(7) center offset $(arcsec)$	(8) RA & Dec deg
NGC 853†	CO	1489.5 ± 0.4	72.5	0.32	48.5	-0.3, 2.9	-
	phot.	-	72.5	0.32	47.8	-0.3, 2.9	32.9, -9.3
NGC 949	CO	591.5 ± 2.8	146.8 ± 2.7	0.63 ± 0.1	68.1 ± 2.4	-0.6 ± 0.1, -0.6 ± 0.1	-
	phot.	-	142.8	0.48	59.6	-0.0, 0.3	37.7, 37.1
NGC 1012†	CO	965.7 ± 3.1	17.7 ± 2.5	0.64 ± 0.0	68.8 ± 1.9	1.08, -0.51	-
	phot.	-	21.4	0.49	60.3	1.1, -0.5	39.8, 30.1
NGC 1035	CO	1202.8 ± 1.2	145.3 ± 0.38	0.62 ± 0.0	67.6 ± 0.6	0.42 ± 0.1, 2.27 ± 0.3	-
	phot.	-	146.9	0.69	73.8	-0.4, 0.8	39.9, -8.1
NGC 4150†	CO	208.0 ± 3.8	147.8	0.22	39.7	0.1 ± 0.06, -0.1 ± 0.05	-
	phot.	-	151.9	0.28	44.4	-0.3, -0.1	182.6, 30.4
NGC 4310	CO	908.6 ± 0.2	157.5 ± 0.9	0.4 ± 0.1	49.6 ± 1.0	-0.7 ± 0.04, 2.6 ± 0.03	-
	phot.	-	157.9	0.53	62.8	0.5, -0.2	185.6, 29.2
NGC 4451	CO	841.0 ± 1.0	160.7 ± 1.3	0.5 ± 0.02	59.8 ± 1.2	0.4 ± 0.1, -0.1 ± 0.1	-
	phot.	-	165.6	0.34	49.4	0.1, 1.1	187.2, 9.3
NGC 4632	CO	1680.6 ± 0.2	60.4 ± 0.4	0.5 ± 0.0	59.1 ± 0.3	1.1 ± 0.3, -0.3 ± 0.1	-
	phot.	-	60.2	0.63	69.7	0.1, 0.3	190.6, -0.1
NGC 4701	CO	706.2 ± 1.0	48.1 ± 1.8	0.4 ± 0.1	51.3 ± 1.0	0.4 ± 0.1, 0.7 ± 0.1	-
	phot.	-	41.9	0.24	40.7	0.4, 0.7	192.3, 3.4
NGC 5303†	CO	1418.9 ± 1.0	81.9 ± 1.0	0.5 ± 0.0	63.7 ± 0.3	-0.2, -0.3	-
	phot.	-	82.9	0.41	54.9	-0.2, -0.3	206.9, 38.3
NGC 5692	CO	1578.9 ± 1.0	31.8 ± 1.3	0.3 ± 0.0	48.5 ± 0.9	0.7 ± 0.1, -0.2 ± 0.1	-
	phot.	-	36.8	0.36	50.9	-0.3, 0.1	219.6, 3.4
NGC 5949	CO	442.1 ± 0.7	136.9 ± 0.5	0.5 ± 0.1	62.5 ± 0.5	-0.8 ± 0.1, -1.0 ± 0.1	-
	phot.	-	143.1	0.53	63.0	0.5, -0.5	232.0, 64.8
NGC 6106	CO	1441.7 ± 0.4	137.2 ± 0.6	0.4 ± 0.1	52.7 ± 0.7	1.3 ± 0.1, 0.6 ± 0.1	-
	phot.	-	139.3	0.43	56.3	-1.3, -0.0	244.7, 7.4
NGC 6207	CO	847.1 ± 0.3	19.0 ± 0.2	0.6 ± 0.0	67.7 ± 0.2	0.4 ± 0.1, -1.6 ± 0.1	-
	phot.	-	21.2	0.51	61.6	-0.1, -0.8	250.8, 36.8

Note. — (†): some or all of the parameters (position angle, ellipticity, and center) had to be fixed to obtain a fitting result that made sense; otherwise, the fitting was unstable or unreasonble, possibly due to the large hole at the center of the CO distribution (e.g., NGC 853) or the total size of the CO distribution being too small (e.g., NGC 4150). In detail, the fixed parameters for each galaxy are: NGC 853: PA, ellipticity, and center; NGC 1012: center; NGC 4150: PA and ellipticity; NGC 5303: center.
For each galaxy, the CO values were obtained from CO data using DiskFit; the photometric values were reduced from r-band imaging data from Apache Point Observatory or IRAC Channel-2 data when available. For DiskFit, the input and output values for the center are the offset with respect to the center pixel (0,0) of the image. Hence, both CO and photometric values in column (7) are the center offset with respect to the center pixel of each CO image. The photometric values in column (7) are converted from the RA and Dec in columns (8) and (9).

Table 4.2: Constraints on the disk geometry from CO and optical imaging

(1) Name	(2) distance Mpc	(3) source	(4) v_{rot} (km s^{-1})	(5) radius (kpc)	(6) M_{dyn} ($10^9 M_\odot$)	(7) $\log(L_*/L_\odot$
NGC 853	20	(HFD)	83 ± 3	1.6	2.5	9.48
NGC 949	10	(T13)	79 ± 1	1.4	2.0	9.36
NGC 1012	14	(HFD)	67 ± 3	1.6	1.7	9.65
NGC 1035	16	(T13)	113 ± 3	2.3	6.8	9.54
NGC 4150	13	(T13)	119 ± 3	0.6	2.1	9.53
NGC 4310	15	(HFD)	106 ± 1	1.4	3.8	9.27
NGC 4451	26	(T13)	98 ± 3	2.3	5.0	9.80
NGC 4632	14	(T13)	84 ± 1	1.9	3.2	9.70
NGC 4701	17	(T09)	75 ± 1	1.3	1.7	9.53
NGC 5303	28	(HFD)	112 ± 3	3.2	9.4	9.56
NGC 5692	27	(HFD)	101 ± 2	2.5	5.9	9.67
NGC 5949	12	(T13)	105 ± 2	2.1	5.5	9.41
NGC 6106	24	(T13)	116 ± 3	3.3	10.3	9.85
NGC 6207	16	(T13)	107 ± 1	2.4	6.3	9.67

Note. — Column (2) shows the distance to the galaxies. The values were obtained from the sources listed in column (3): Tully et al. (2009) (denoted as T09) or Tully et al. (2013) (denoted as T13) when available and the Hubble Flow Distance (HFD) (Virgo + GA + Shapley) on the NASA/IPAC Extragalatic Database (NED, http://ned.ipac.caltech.edu).
The rotation velocities (v_{rot}, column (4)) were obtained from the CO rotation curves in our observations at the maximum observed radius in column (5).
Column (6) is the dynamical mass calculated from the rotation velocity at the radius in column (5), using $M_{dyn} = v_{rot}^2 r/G$.
Column (7) is the stellar luminosity obtained from r-band images.

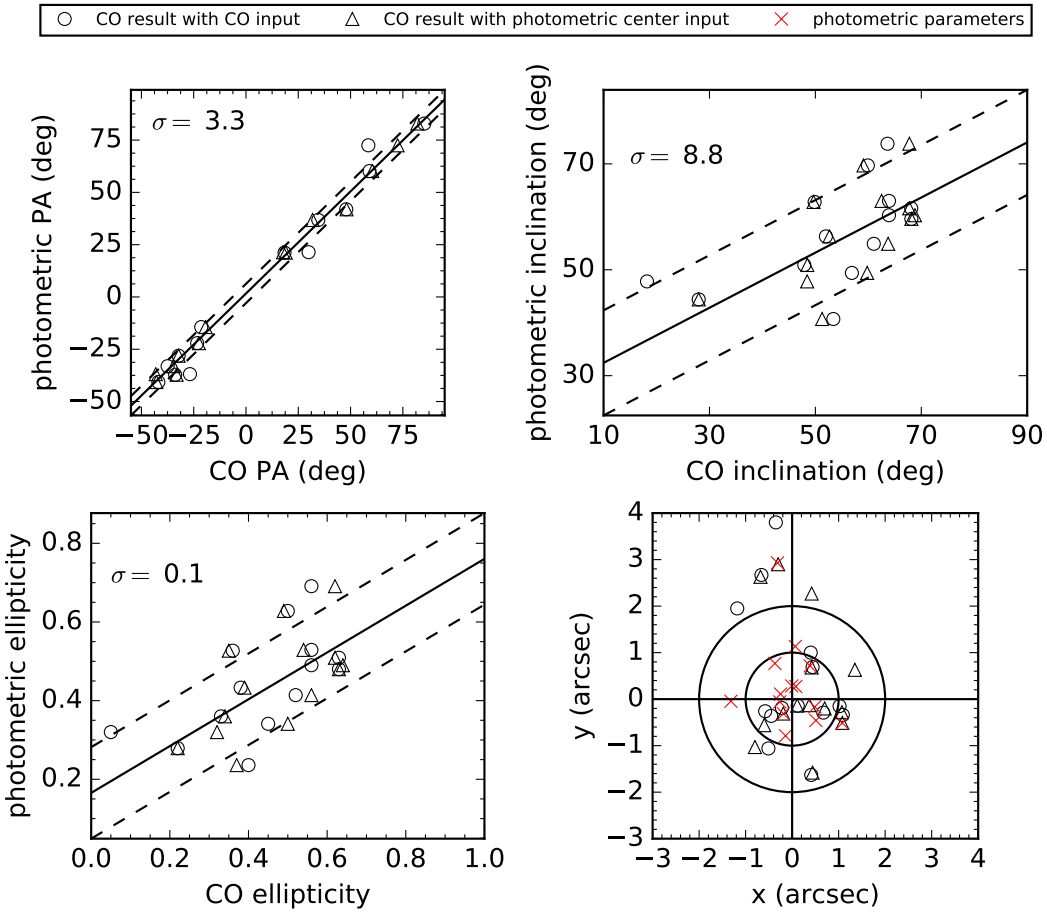

Figure 4.4: Comparison between the geometric parameters derived from the CO data and those from photometric measurements (APO r-band data or IRAC channel-2 data) for the galaxies with CO detections. The parameters from the CO data were obtained from the rotation curve fitting using DiskFit, with either all fitting inputs from CO data (circle) or photometric centers as the inputs for the centers (triangle). The straight black line is the best fit line to show the correlation between photometric parameters and CO parameters; the dashed lines indicate the 1σ standard deviation from the best fit line. The bottom right plot shows the centers of the galaxies relative to the center pixel (0, 0) of their CO images; the CO centers (black) were obtained from DiskFit, and the photometric centers (red) were converted from the RA and Dec values obtained in APO r-band data or IRAC channel-2 data. The circles indicate the radii of 1 and 2 arcsec, where most of the galaxy centers are with respect to the centers of their CO images.

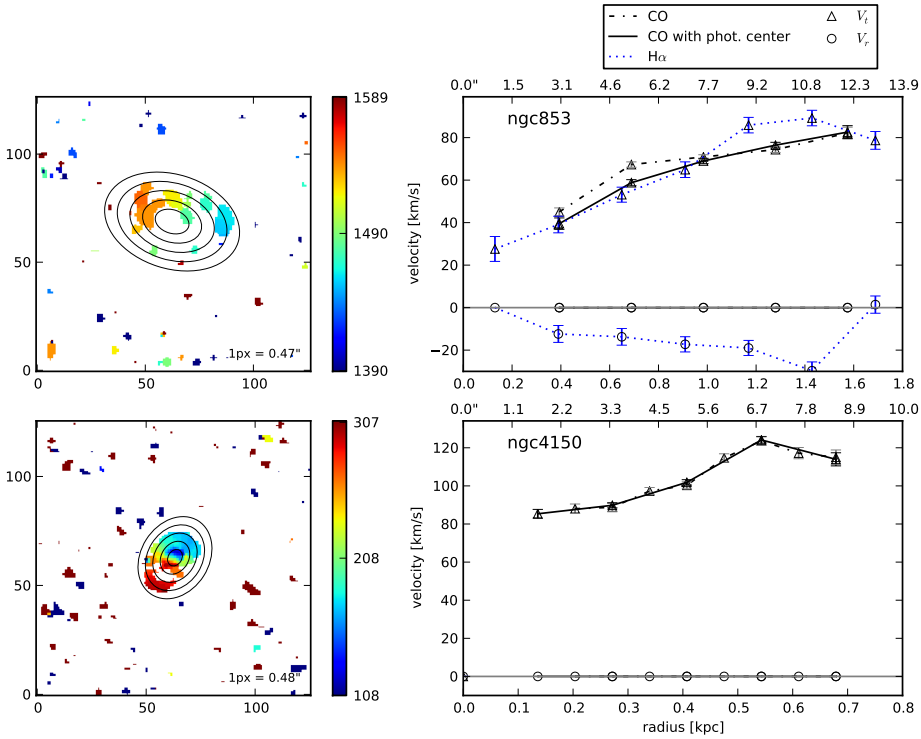

Figure 4.5: Rotation curves of the galaxies in the survey as fitted by DiskFit. Left column: the corresponding (unmasked) moment-1 maps with overlaid rings, whose centers, PA and ellipticity were obtained from DiskFit results. The x and y coordinates of the maps are measured in pixels, corresponding to a coverage of $30'' \times 30''$; the color bars indicate the systemic velocity (km/s). The triangles and circles indicate the tangential and radial velocity components, respectively. The blue dotted line shows the Hα rotation curves (also obtained using DiskFit; the PA, ellipticity and center were also fixed for NGC 853). The black lines show the CO rotation curves with all CO data input (dot-dashed) and CO rotation curves with photometric center for the input (solid). Both NGC 853 and NGC 4150 were fitted using the $m = 0$ model with no radial flow; the input PA, ellipticity and center were fixed for NGC 853, whereas the input PA and ellipticity were fixed for NGC 4150. For NGC 1012 and NGC 5303, the center was fixed. All other galaxies were fit with the $m = 0$ radial-flow model and no fixed parameters

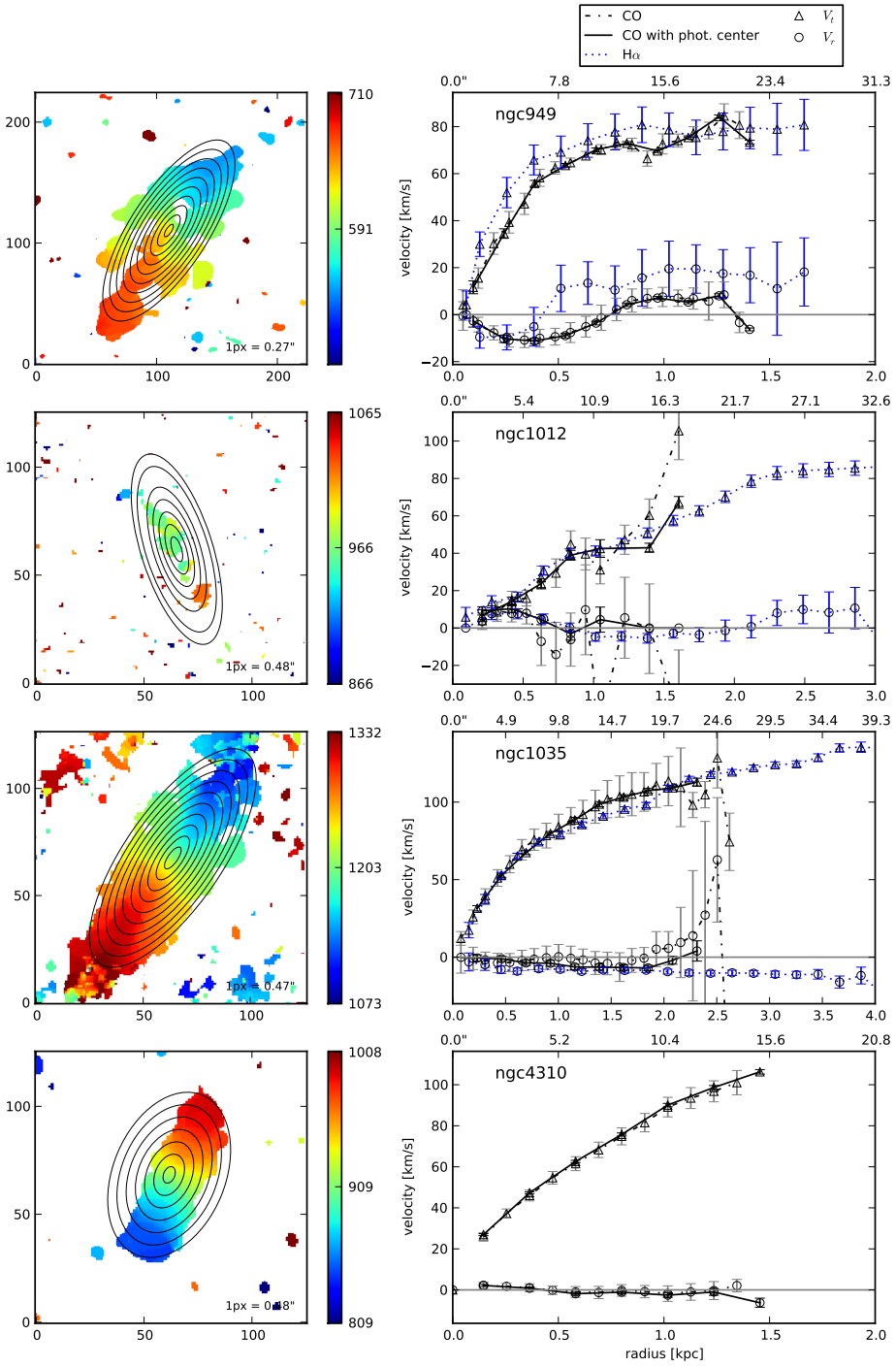

Figure 4.5: (cont.)

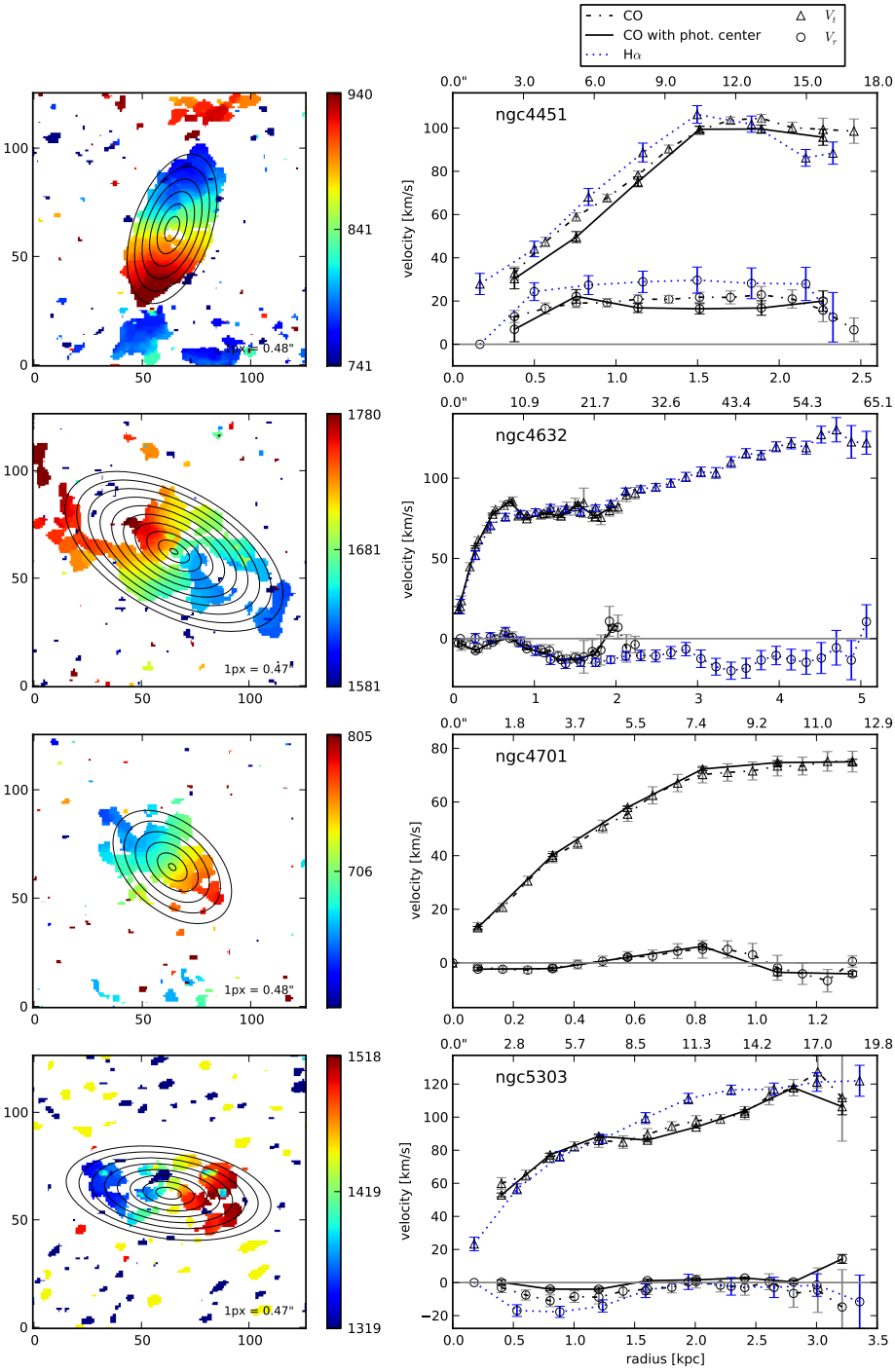

Figure 4.5: (cont.)

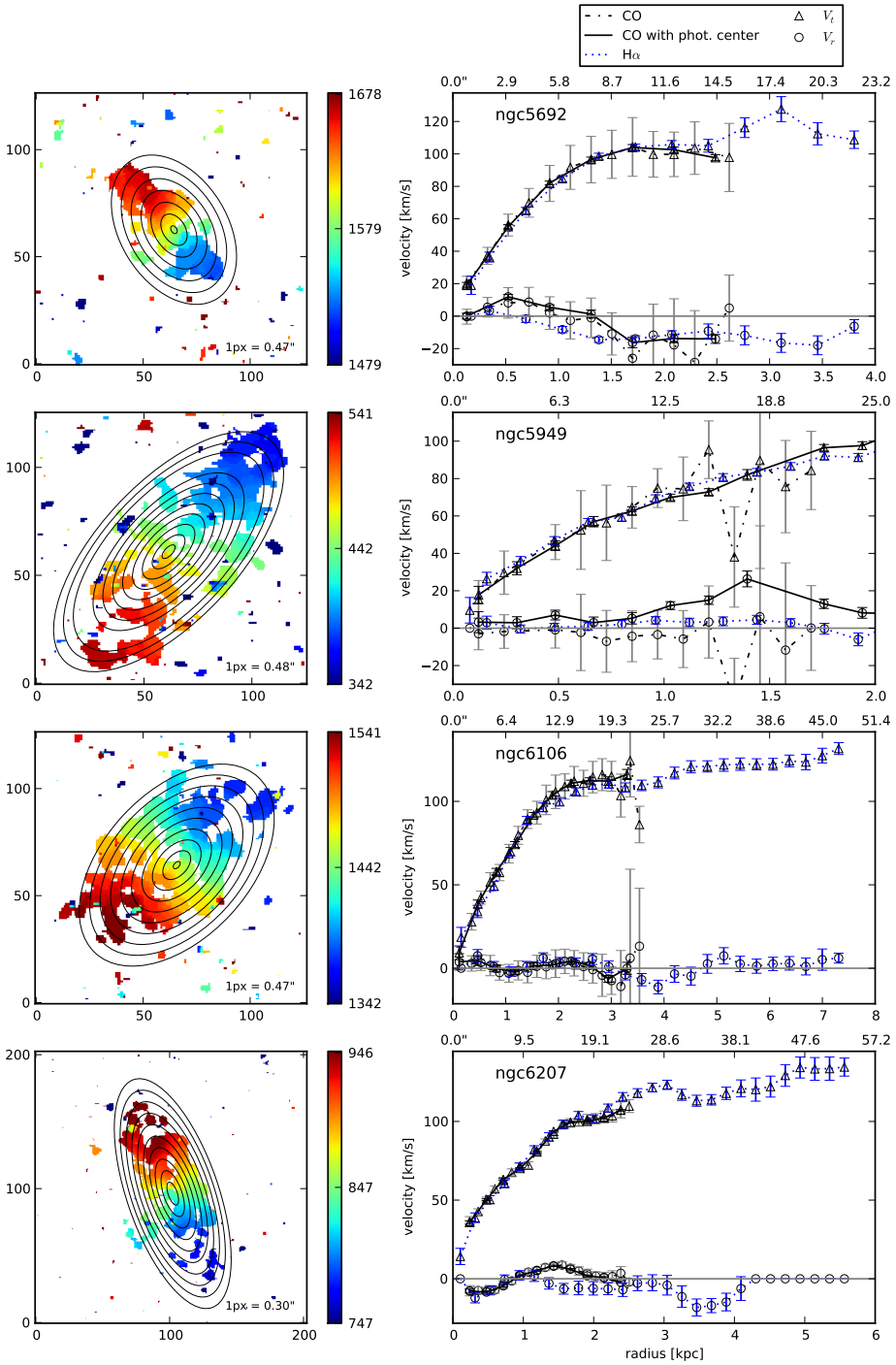

Figure 4.5: (cont.)

Table 4.3: Constraints on the mass distribution from models with a gNFW halo and variable disk

(1) Name	(2) α	(3) log M_{200} $/(M_\odot)$	(4) c_{200}	(5) M_*/L $(M_\odot/L_\odot)$	(6) r_{-2} (kpc)	(7) log ρ_0 $/(M_\odot$ kpc$^{-3})$
r-band						
NGC853	0.92 ± 0.67	9.06 ± 0.93	23.91 ± 9.60	1.58 ± 0.92	<4.10	7.73 ± 1.22
NGC949	0.93 ± 0.59	9.51 ± 0.95	>11.68	1.26 ± 0.40	<4.51	7.81 ± 1.15
NGC1012	<1.67	<11.81	14.23 ± 9.02	<0.60	<15.05	7.74 ± 0.53
NGC1035	<0.44	11.04 ± 0.07	35.07 ± 2.87	<1.55	2.81 ± 0.36	8.96 ± 0.20
NGC4150	1.09 ± 0.46	>9.99	>16.62	0.49 ± 0.34	4.85 ± 1.82	7.96 ± 0.76
NGC4310	0.60 ± 0.09	>11.4	24.36 ± 2.94	<0.65	7.46 ± 1.86	8.18 ± 0.2
NGC4451	<1.86	<11.31	<37.32	1.31 ± 0.21	<8.56	7.67 ± 1.12
NGC4632	1.74 ± 0.15	10.74 ± 0.23	>12.32	<1.17	2.65 ± 2.72	6.22 ± 1.04
NGC4701	<0.71	10.83 ± 0.39	33.20 ± 6.39	<0.25	2.54 ± 1.67	8.82 ± 0.42
NGC5303	0.93 ± 0.52	11.05 ± 0.52	20.99 ± 10.3	<1.05	4.52 ± 5.98	7.66 ± 0.77
NGC5692	<1.51	10.47 ± 1.72	<36.69	0.97 ± 0.41	2.48 ± 2.65	8.08 ± 0.75
NGC5949	0.41 ± 0.23	11.58 ± 0.31	18.51 ± 3.44	0.98 ± 0.60	8.10 ± 3.39	8.03 ± 0.32
NGC6106	<0.56	11.43 ± 0.22	22.69 ± 4.41	<1.10	5.87 ± 2.63	8.42 ± 0.35
NGC6207	<0.86	10.75 ± 0.45	<24.22	1.73 ± 0.41	5.06 ± 2.94	7.8 ± 0.41
———-						
IRAC Ch2 (4.5μm)						
NGC853	-	-	-	-	-	-
NGC949	-	-	-	-	-	-
NGC1012	-	-	-	-	-	-
NGC1035	<0.38	11.11 ± 0.08	33.6 ± 2.43	<0.12	3.09 ± 0.44	8.93 ± 0.18
NGC4150	1.03 ± 0.27	>11.05	>22.53	<0.19	4.94 ± 1.07	8.14 ± 0.54
NGC4310	0.52 ± 0.16	>11.37	24.17 ± 3.08	<0.21	7.42 ± 1.96	8.25 ± 0.23
NGC4451	<1.87	<11.38	19.56 ± 11.88	0.29 ± 0.05	<8.76	7.64 ± 1.16
NGC4632	1.76 ± 0.16	10.69 ± 0.23	>12.45	<0.38	2.57 ± 2.55	6.08 ± 1.13
NGC4701	<0.67	10.85 ± 0.53	27.31 ± 7.61	<0.19	3.09 ± 3.23	8.59 ± 0.49
NGC5303	0.89 ± 0.54	10.91± 0.73	21.45 ± 10.29	<0.28	3.92 ± 5.28	7.71 ± 0.81
NGC5692	-	-	-	-	-	-
NGC5949	0.44 ± 0.24	11.59 ± 0.32	19.31 ± 3.32	<0.65	7.74 ± 3.15	8.05 ± 0.33
NGC6106	<0.64	11.41 ± 0.24	21.91 ± 4.72	<0.34	5.99 ± 2.88	8.36 ± 0.40
NGC6207	0.6 ± 0.73	<11.27	<32.99	0.53 ± 0.13	<9.02	7.63 ± 0.76

Note. — †: some parameters were fixed in DiskFit to obtain the rotation curves: NGC 853: the PA, ellipticity and center were fixed; NGC 1012 and NGC 5303: the center was fixed; NGC 4150: the PA and ellipticity were fixed. For all other galaxies, the rotation curves were obtained with no fixed geometric parameter.

Columns (2-5) show the MCMC best-fit results of the rotation curves to the gNFW function in terms of the inner power-law slope α, virial mass M_{200} in the logarithmic scale, concentration c_{200}, and stellar mass-to-light ratio M_*/L, respectively. The characteristic radius $r_{-2} = (2-\alpha)r_s$ and the log density in columns (6) and (7) were calculated from M_{200} and c_{200}.

4.3 Mass modeling

The rotation curves of the galaxies receive contributions from five mass components: atomic gas, molecular gas, stars, dust, and dark matter. In this study, for simplicity, we assume that the dust, atomic gas and molecular gas components are negligible, since for disk galaxies, the dust-to-gas mass ratio is $\sim 1\%$, and the gas-to-stellar mass ratio is $\sim 5-10\%$, e.g., for the Milky Way, the total HI mass is $7\times10^9 M_\odot$ and the total H_2 mass is $1.7\times10^9 M_\odot$ (Dame (1993)). In future studies, we will include the HI mass from archival HI data and H_2 mass deduced from CO measurements and the CO-to-H_2 conversion factor, and we expect that such inclusion does not significantly change the result. First, for the DM component, the density profile is originally seen in CDM simulations in Navarro, J. F. et al. (1996) as follows:

$$\rho(r) = \frac{\delta_c \rho_{crit}}{(r/r_s)[1+(r/r_s)]^2} \tag{4.6}$$

where δ_c is the overdensity factor, r_s is the scale radius, and ρ_{crit} is the critical density of the universe.

$$\rho_{crit} = \frac{3H^2(z)}{8\pi G} \tag{4.7}$$

A concentration c, also called c_{200}, is defined as r_{200}/r_s, with r_{200} being the virial radius where the mean enclosed density is 200 times the critical density.

If we define the density parameter $\rho_0 \equiv \delta_c \rho_{crit}$, the integrated mass within a radius R is:

$$M = \int_0^R 4\pi r^2 \rho(r) dr = 4\pi\rho_0 r_s^3 \left[\ln\left(\frac{r_s+R}{r_s}\right) - \frac{R}{r_s+R}\right] \tag{4.8}$$

Thus, the virial mass is:

$$M_{200} = 4\pi\rho_0 r_s^3 \left[\ln(1+c) - \frac{c}{1+c}\right] \tag{4.9}$$

and the parameter ρ_0 is related to the mean squared density inside the virial radius and that inside the scale radius as follows:

$$\langle\rho^2\rangle_{r_{200}} = \frac{\rho_0^2}{c^3}\left[1 - \frac{1}{(1+c)^3}\right] \tag{4.10}$$

$$\langle\rho^2\rangle_{r_s} = \frac{7}{8}\rho_0^2 \tag{4.11}$$

A very general halo profile form was introduced by Hernquist, L. (1990), where the inner power law, outer power law, and sharpness of the transition are all variables. Klypin, A. et al. (2001) show that these parameters are too degenerate for realistic data to constrain

and modified the generalized NFW (gNFW) function to have only an inner power-law slope α as a variable. Thus, the gNFW density function is:

$$\rho(r) = \frac{\delta_c \rho_{crit}}{(r/r_s)^{\alpha}[1 + (r/r_s)]^{3-\alpha}} \tag{4.12}$$

which means when $\alpha = 1$, the profile reduces to the NFW profile, and the DM halo has a central cusp when $\alpha \geq 1$.

Because the density $\rho \propto r^{-\alpha}$ at $r \ll r_s$, there is a large covariance between α and r_s in the parametrization of the gNFW profile. To circumvent this problem, instead of r_s, we use the radius $r_{-2} \equiv (2-\alpha)r_s$, which is the radius at which the local slope of the density profile is r^{-2}. Correspondingly, we redefine the concentration $c_{200} = r_{200}/r_{-2}$; for an NFW profile, $r_{-2} = r_s$.

Following Adams, J.J. et al. (2014), we model the stellar and DM mass components in the galaxies using the following procedure. First, we obtained the stellar rotation curves by modelling the optical and near-IR imaging data[3], introduced in 4.2, using a multi-Gaussian expansion. Then, the routines provided by Cappellari, M. (2002) allowed us to compute the circular velocity in the disk midplane that corresponds to the disk potential for a fiducial M_*/L, which we selected to be unity. Full details will be provided in Relatores et al (in preparation). Finally, we use the Markov Chain Monte Carlo (MCMC) method to measure parameter constraints and covariances with the python-based software *emcee* (Foreman-Mackey, D. et al. (2013)), the uncertainties of the fits are calculated follows the procedure in *emcee*, which uses percentiles of the posterior distribution: the code computes the 16th, 50th, and 84th percentiles, takes the 50th percentile as the primary value, the difference between the 84th and 50th percentiles as the upper error and the difference between the 50th and 16th percentiles as the lower error, as described in more detail in Adams, J.J. et al. (2014) and Relatores et al. (in preparation). The model contains 4 parameters: logarithm of the virial mass ($\log M_{200}$), concentration c, inner density logarithmic slope of the gNFW function α, and stellar mass-to-light ratio M_*/L. The first 3 parameters, $\log(M_{200})$, c and α, describe the DM halo profile. Note that α is similarly defined in some literature (e.g., Bolatto, A.D. et al. (2002), Simon, J.D. et al. (2005)) and is equivalent to γ in Adams, J.J. et al. (2014).

As previously mentioned, the stellar rotation curves described above were computed for a fiducial mass-to-light ratio $M_*/L = 1$. Then, when fitting the total rotation curves to the gNFW model, we allow the algorithm to scale these stellar rotation curves by $\sqrt{M_*/L}$ for the minimization process. Note that M_*/L is specific to each photometric band and depends on age, dust extinction, and metallicity. These quantities may vary from galaxy to galaxy and within each galaxy, but M_*/L changes significantly less at redder wavelengths. Thus, we assume a single M_*/L for each galaxy with the r-band (0.6 micron) and Ch2 (4.5 micron) data, and we expect that this assumption is more valid for Ch2 with its longer wavelength compared to r-band . We set the limits for the parameters as follows: $0 \leq \alpha \leq 2$;

[3]For NGC 4150 and NGC 4310, due to the lack of r-band images from the ARC 3.5-m telescope, we used r-band images from the SDSS III archive.

$8.0 \leq log(M_{200}) \leq 12.5$; $2 \leq c \leq 40$; $0.1 \leq M_*/L < 2.0$ for r-band and $0.05 \leq M_*/L < 1.0$ for Ch2 data. The priors that we used are: $\alpha = 1$, $\log(M_{200}) = 10$, $c = 25$, and $M_*/L = 1$ for r-band or 0.5 for Ch2.

For the results, we report the median and 68% confidence level in the MCMC posterior distribution of the parameters when possible; otherwise, when the posterior peaks at the edge of the limit interval, we report the 95% confidence level limit. The average values of the parameters (e.g., α) of the galaxy sample can be computed by assuming that the sample has a distribution of each parameter, which can be approximated as a Gaussian distribution, and finding the mean and scatter.

We also fit the data for the minimum-disk (i.e., $M_*/L = 0$) and maximum-disk models. The maximum M_*/L is determined by increasing M_*/L until the stellar rotation curve exceeds the sum of the total rotation curve and its uncertainty for at least two radii, i.e., $v_*(r) > v_t(r) + \Delta v_t(r)$ for at least 2 data points in the rotation curve. The points with $v_*(r) > v_r(r)$ were not considered in the fit.

4.4 Mass Modeling Results

In this section, we will first discuss the mean values and range of the parameters in our sample, which we obtained from the MCMC fits, and compare them to literature values to verify the consistency of different samples. Then, we will discuss the correlations between the parameters in the samples and whether the correlations provide evidence for theoretical models. Finally, we discuss specific galaxies with unusual behaviors in the sample and how much they affect the robustness of our previously stated results. The samples to which we compare ours are Oh, S.-H. et al. (2011) and Oh, S.-H. et al. (2015)(abbreviated as "O11" and "O15", respectively, in the remainder of the text), which have lower-mass and more nearby galaxies, Adams, J.J. et al. (2014) ("A14"), which have galaxies in approximately the same mass range as our sample, and the simulations from Chan, T. K. et al. (2015) and Governato, F. et al. (2012). Taken together, the samples constitute a wide range of mass, in which the variation of the DM inner slope may give evidence for baryonic feedback models, which we will discuss in section 4.5.

Throughout the section, we will refer to Figures 4.6-4.10 and Table 4.3. Figure 4.6 (p.63) shows the results of the mass modeling procedure to the rotation curves derived from a subset of our CO observations. The total rotation curve (magenta), which is fit to the CO data (cyan), is the sum of two mass components in the gNFW model: stellar mass (green) and dark matter (blue). Five posterior samples of parameters were randomly selected after the MCMC walkers began converging to plot the example curves as shown. Table 4.3 lists the constraints on the mass profile parameters derived from models with a variable M_*/L. In cases where both r-band and 4.5-micron data are available to construct the stellar rotation curve, we use both and list the constraints separately. For the galaxies with only the 95% confidence level upper limits of α reported (see Table 4.3), we show the histogram of their posterior distribution of α in Figure 4.7. To visualize a direct comparison between the

gNFW parameters obtained using r-band data and those obtained using Ch2 data, we also plot the parameters in Figure 4.8 (p.66), where all three cases of minimum, variable, and maximum disks are shown. We also plot the inner slope values for the individual galaxies in Figure 4.9. We note that although Figure 4.6 shows generally good fits to the data for most of the sample, NGC 1012, NGC 4451 and NGC 4701 have bad fits, where the parameters are forced to the limits. These galaxies will be discussed in detail later, but we caution that their large DM inner slopes may be a result of the bad fits, and the average α might decrease compared to those shown in Table 4.3 when we compute the results for Hα in Relatores et al. (in preparation).

4.4.1 Average values and range of the parameters in our sample and comparison with literature values

In this subsection, we will state the main values of the gNFW parameters and compare them with the results of the most recent surveys: A14, O11 (THINGS), and O15 (LITTLE THINGS).

Inner DM slope. First, the average inner slope of the DM profile is $\alpha = 0.58 \pm 0.45$ or 0.64 ± 0.49 when r-band or 4.5-micron images are used to estimate the stellar contribution to the rotation curves, respectively. As four of our galaxies do not have Ch2 data, we also computed the mean slope for the sample of 10 galaxies that have both r-band and Ch2 available, and we found that $\alpha = 0.66 \pm 0.54$ with the r-band contribution; thus, our slope values do not vary with respect to the band of the stellar data. This α value is close to the values in A14 of 0.58 ± 0.24 (measured from the gas kinematics) and 0.67 ± 0.10 (measured from stellar kinematics). Simon, J.D. et al. (2005) has a slightly steeper slope of 0.73 ± 0.44 (average of 5 galaxies). However, O11 and O15 have much shallower density profiles: 0.29 ± 0.07 (O11, 7 galaxies), and 0.32 ± 0.24 (O15, 26 galaxies). Note that the density profile slope of Simon, J.D. et al. (2005) was calculated from a power-law fit.

Regarding the range of α, Figure 4.8 shows that for most galaxies, α spans over the range of $\sim 0.4 - 0.9$ and α does not significantly change when using different photometric bands (there are some exceptions which we will later discuss). Considering only the values without upper limits, the slopes indicate generally cuspier profiles; however, the other half of the galaxies with upper limit values actually have quite low α (based on the histogram of the posterior distribution of α.) In comparison, the range of α is $0.3 - 0.88$ in A14, $-0.13 - 0.43$ in O11, and $-0.97 - 1.25$ in O15. Hence, all surveys have large ranges of inner slope values from cored to cuspy.

Other parameters in the gNFW model. In our sample, the average M_*/L is 0.10 ± 0.02 and 0.49 ± 0.32 for Ch2 and r-band, respectively. The r-band value is consistent with the stellar mass-to-light ratios found in A14 (~ 1.0 for both gas-traced and stellar-traced models with r-band data), considering the large scatter.

Figure 4.9 shows that in some cases, the maximum M_*/L is lower than the best-fit M_*/L for a variable disk (e.g., NGC 853, NGC 4451, and NGC 5692) because we allowed the variable-disk M_*/L to vary between 0.1 and 2 in the MCMC code instead of having

the maximum M_*/L as the upper limit. These galaxies also appear to have higher stellar contribution in Figure 4.6. For the remaining galaxies, considering the similarity between the two values for most galaxies, we conclude that our fitting results are reasonable. In the next paper, we will need to examine the Hα rotation curves and mass modelling fits in more detail and check the consistency with CO data.

For the virial mass, our sample has the range of $\log(M_{200}/M_\odot) \sim 10 - 11.6$ (with only NGC 853 having $\log(M_{200}/M_\odot) = 9.06 \pm 0.93$); for the concentration, $c \approx 14 - 35$. In A14, the average $\log M_{200} = 11.5 \pm 0.3$ and $c = 17.8 \pm 2.2$ (mean $\pm$ std). Hence, both virial mass and concentration are consistent between the two samples; the high concentration of some of our galaxies may be due to the small extent of our CO data. A comparison between these CO results and the Hα results in our next paper (Relatores et al. in preparation) will help validate the difference in such c values.

4.4.2 Dependence of the density profile slope on other parameters

Figure 4.9 shows that the mean α of the sample is robust against the variation of M_*/L (0, variable, or maximum). There are a few exceptions, e.g., NGC 5692, where α significantly changes with the variation of M_*/L, which we will discuss later. In addition, the virial mass, scale radius, density ρ_0, and concentration c are also robust among the three disk cases, and they are consistent across the galaxies (see Figure 4.8). This result is to be expected because the galaxies in our sample were selected to have similar physical characteristics (e.g., low-mass, low-surface-brightness, nearby galaxies).

Considering Figure 4.6 and Table 4.3, we can divide the galaxies in the sample into three groups: completely dark-matter-dominated, completely star-dominated, and mixed; in the mixed group, there is a cross-over behavior, where the stellar contribution appears to be dominating in the inner radii (up to 0.5 kpc) but tapers off, and dark matter begins to dominate. In the DM-dominated group (NGC 1035, NGC 4310, NGC 4632, NGC 5303), all except NGC 1035 have larger α than the mean of the sample (≥ 0.7). In the star-dominated group (NGC 853, NGC 949, NGC 1012, NGC 4451, NGC 5692), NGC 853 and NGC 949 have large α, but the posterior distribution of α of the other three galaxies gravitate towards lower values. The mixed group has similarly unpredictable behaviors: the radius at which the cross-over occurs in the stellar and DM rotation curves does not indicate how large α is, and we have a mixture of cored and cuspy profiles here: NGC 4701, NGC 5949 and NGC 6106 are cored, NGC 6207 has approximately the mean slope of the sample, and NGC 4150 is cuspy. The star-dominated galaxies have the largest M_*/L in the samples (except NGC 1012), which raises the question of whether the DM slope can be reliably inferred from the small residual rotation. However, the test with the limiting cases of minimum and maximum disks show that the slope does not significantly change with respect to the disk for these galaxies (Figure 4.9), the only exception being NGC 5692. The fit of NGC 5692 only relies on the r-band data, for which the assumption of a constant M_*/L throughout the disk may not apply, and M_*/L for r-band data is always larger than that of Ch2 data, so the stellar mass-to-light ratio of this galaxy may actually be lower than the result that we have. There is

a very large range in α depending on our assumption about the stellar M_*/L for NGC 5692, as the $1-\sigma$ uncertainty on α extends from 0.6 to 1.4. In addition, recall Figure 4.5 and 4.2, some steeply rising rotation curves correspond to large DM slopes (e.g., NGC 949, NGC 4632) and some slowly rising ones correspond to small slopes (e.g., NGC 5949); however, contrary cases are also present, e.g., NGC 853 has a slowly rising curve but a large α, and NGC 1035 has a steep rotation curve but a small α. Because the rotation curve and density profile are closely linked mathematically (i.e., the rotation curve depends on the square root of the enclosed mass, which is the integral of the density profile), the apparent steepness of the rotation curves should be an indicator of the DM slope. Thus, we believe that the contrary case of NGC 853 is due to its bad rotation curve (from patchy CO distribution), and we will show that the problem with NGC 1035 is resolved with better-resolution data (5.2).

Now, we proceed to statistically examine the behavior of α as functions of different parameters: stellar mass-to-light ratio, stellar mass, dynamical mass, virial mass, and distance to the galaxy. Figure 4.10 shows the relations of α, $\log M_*$, $\log M_{200}$, dynamical mass ($\log M_{dyn}$, M_*/L, and distance. In this figure, we include the galaxies in our sample (red and black squares for r-band and Ch2 data, respectively), the results of A14 (yellow circles), and the results of THINGS (O11) and LITTLE THINGS (O15) (green stars and cyan circles) when available. To find the correlations when we have upper limits in our values (specifically, α, $\log M_{200}$, and M_*/L), we used the "cenken" function in the CRAN/NADA package (Helsel (2005), Akritas, M.G. et al. (1995)), which computes the Kendall tau for singly (y only) or doubly (x and y) censored data (upper limits), the Akritas-Theil-Sen nonparametric line, and the Turnbull estimate of intercept. Among our $\log M_{200}$ values, two galaxies have lower limits (NGC 4150 and NGC 4310), which we removed from the correlation computation of α vs. $\log M_{200}$. We found the following correlations:

$$\alpha = 0.02d + 0.27 \text{ (r-band or Ch2, A14, O11, O15)} \tag{4.13}$$

$$\alpha = 0.16 \log M_{dyn} - 1.09 \text{ (r-band, O11, O15)} \tag{4.14}$$

$$\alpha = 0.17 \log M_{200} - 1.38 \text{ (Ch2, A14, O15)} \tag{4.15}$$

where d is the distance to the galaxy, and the data used to obtain the correlations are listed in the parentheses. The p-values of these correlations are 0.005, 0.03, and 0.02, respectively.

There is no significant correlation between α and M_*/L, which confirms the results shown in Figures 4.8 and 4.9. More importantly, there is also no significant correlation between α and the stellar mass. The correlations between α and the masses were only found in either r-band or Ch2 but not both, and their large significance values (p-values) suggest against their certainty. Note that the range of total dynamical mass in our sample is $3.65 - 37.9 \times 10^9 M_\odot$ with an average of $(14.5 \pm 9.43) \times 10^9 M_\odot$ (mean $\pm$ std) (Truong et al. 2017, collected from literature values), and the dynamical mass calculated up to the extent of our data is $1.7 - 10.3 \times 10^9 M_\odot$ (Table 4.2). The correlation with distance is surprising because one would naively expect shallower density profiles at larger distances due to lower resolution in the data.

There are some simulations to which we can compare our results. First, our DM slopes are slightly larger on average than galaxies of comparable stellar mass in Chan, T. K. et al. (2015) (FIRE simulations), as $\alpha_{FIRE} \approx 0.5$ for $M* =\sim 10^7 - 10^{11} M_\odot$) (the stellar masses in our sample are in the range of $10^8 - 10^9 M_\odot$). In terms of trends, the FIRE simulations do not predict any trend over the mass range from LITTLE THINGS to ours. Governato, F. et al. (2012) show a slight trend of $\alpha \approx -0.35 \log_{10}(M_*/10^8 M_\odot) + 0.5$ with $4 < \log M_* < 9.4$ within 500 pc, i.e., the inner DM profile flattens with increasing stellar and halo mass, and for galaxies in our mass range, the slope would approach the values of the THINGS and LITTLE THINGS samples. On the other hand, our results suggest the opposite trend: more massive galaxies may have larger DM slopes, i.e., cuspier profiles. The lack of correlation between alpha and dynamical mass is most likely attributed to methodological differences between our work and the work for THINGS and LITTLE THINGS data. In the next paper of the series, we will present the full Hα sample, which has approximately twice as many galaxies as the CO sample, and the full mass modeling results of the Hα rotation curves. This larger sample may allow the detection of clearer correlations (if any) between α and M_{dyn} as well as other quantities.

4.4.3 Further discussion on some specific galaxies and their effects on the robustness of the results

NGC 5949. For NGC 5949, which is the only galaxy common to both our sample and Adams et al. (2014), we measure $\alpha = 0.44 \pm 0.24$ and $M_*/L =< 0.65$ with Ch2 data (the r-band results: $\alpha = 0.41 \pm 0.23$ and $M_*/L = 0.98 \pm 0.60$), whereas Adams et al. found $\alpha = 0.53 \pm 0.14$ and $M_*/L = 1.16 \pm 0.34$. Hence, the inner slope is reasonably consistent between the two papers, and the stellar mass-to-light ratio is consistent if we compare the r-band value.

NGC 4632 and NGC 5303. In our sample, only NGC 4632 has α clearly larger than 1 with both Ch2 and r-band data, but the posterior distribution of its stellar mass-to-light ratio gravitates towards the lower limit (0.1) in both channels. This case is in contrast to the case of NGC 853. However, Figure 4.6 shows NGC 4632 as a DM-dominated galaxy (although the fit of the total rotation curve to the data is poor), Figure 4.5 shows a steeply rising rotation curve (for both CO and Hα), and the uncertainty of α is small. Thus, the large α is reasonable. (However, as a check, if we exclude this galaxy from the average alpha computation, we find that $\alpha = 0.2 \pm 0.06$ and 0.5 ± 0.06 for the r-band and Ch2, respectively. This decrease occurs because half of the sample, i.e., 7 galaxies, have α with posterior distribution heavily biased towards lower values near 0, as shown in Figure 4.7 (p.65)). A similar argument can be made for NGC 5303, which has $\alpha \sim 0.9$ with both Ch2 and r-band data. Future results with the Hα rotation curves will help determine if these galaxies are truly cuspy.

NGC 4150 and NGC 4310. These two galaxies have large virial masses ($\sim 10^{11} M_\odot$), and their stellar mass-to-light ratios gravitate towards the limit of the MCMC routine. Figure 4.6 shows that they have different matter distributions: NGC 4150 is star-dominated up

to ~ 0.2 kpc and DM-dominated afterwards, and NGC 4310 is completely DM-dominated. In terms of the DM slope, NGC 4150 has $\alpha_r = 1.09 \pm 0.46$ and $\alpha_{Ch2} = 1.03 \pm 0.27$, and NGC 4310 has $\alpha_r = 0.60 \pm 0.09$ and $\alpha_{Ch2} = 0.52 \pm 0.16$ (the r-band data are from SDSS). Figure 4.5 shows small and/or patchy CO distributions for NGC 4150, the CO extent of NGC 4310 has not reached the flat part of the rotation curve, and no Hα data for NGC 4150 and NGC 4310 for comparison purposes (although NGC 4150 and NGC 4310 do show steeply rising rotation curves, which explains their large α values). Furthermore, NGC 4150 and NGC 4310 are early-type galaxies, unlike the remainder of the sample, so although they are more disk-like than other elliptical galaxies, the current assumption that the stars are in a thin disk to calculate the stellar rotation curves may not correctly apply to these two galaxies. If the stellar distribution is not actually in a thin disk, only the value of the stellar mass-to-light ratio required to produce a given rotation velocity from the stellar component would change, and the fit to the DM halo should not be affected. Nonetheless, if we believe them to be outliers and remove their values from the sample, the average DM slope does not significantly change: $\alpha = 0.57$ and 0.55 for the cases with r-band and Ch2 data, respectively.

NGC 4701. The gNFW fit of this galaxy shows a strong peak of the stellar contribution in the inner 0.3 kpc due to a very bright nuclear cluster, which makes M_*/L stay at 0.1 in the fit to best fit the data. Without NGC 4701, the mean slope of the sample is 0.49 and 0.72 for r-band and Ch2, which is not significantly different from the values with NGC 4701 included in the sample.

NGC 1012 and NGC 4451 These two galaxies have rather bad fits in Figure 4.6. Both appear to be star-dominated and have large upper limits for α: NGC 1012 has $\alpha < 1.67$ (only r-band data are available for the stellar rotation curve), NGC 4451 has $\alpha < 1.86$ for both Ch2 and r-band data. Figure 4.5 shows a small and patchy CO distribution for NGC 1012 and its CO extent has not reached the flat part of the rotation curve. Excluding these two galaxies and NGC 4701 from the calculation of the sample mean because of their bad mass model fits, we obtain $\alpha = 0.66 \pm 0.52$ (r-band) and 0.75 ± 0.57 (Ch2), i.e., the average slope becomes slightly steeper but is still consistent with the values in Adams, J.J. et al. (2014).

4.5 Discussion

In summary, the results show that the inner power-law slope varies over a large range from below 0.38 to 1.76, with the average $\alpha = 0.64 \pm 0.49$, which is consistent with the results of Adams, J.J. et al. (2014) (A14) ($0.30 \leq \alpha \leq 0.88$ and average $\alpha = 0.58 \pm 0.24$ or $\alpha = 0.67 \pm 0.10$ based on the gas or star dynamics model, respectively). In comparison, the average α values calculated by previous studies include: 0.73 ± 0.44 (Simon, J.D. et al. (2005), 5 galaxies), 0.29 ± 0.07 (Oh, S.-H. et al. (2011) (O11), 7 galaxies), and 0.32 ± 0.24 (Oh, S.-H. et al. (2015) (O15), 26 galaxies). Thus, there is a difference in results due to our methodologies: $\alpha \sim 0.6$ (our study, Simon, J.D. et al. (2005) and A14) versus $\alpha \sim 0.3$ (O11 and O15).

On one hand, we selected a sample of well-behaved galaxies, and our method to analyze them is unbiased with respect to cored vs. cuspy profiles. Among our galaxies, 5 have cuspier profiles ($\alpha \geq 0.7$, with NGC 4632 being especially cuspy), and 9 have shallower profiles, which show that dwarf galaxies similar in size (dynamical mass $\sim 10^9 M_\odot$) can have notably different density profiles in the central region. On the other hand, the methodology in O11 and O15 may be biased towards shallower slopes: the density profile slopes are calculated using only data within the so-called break radius (up to 1 kpc), which may be subjected to low resolution in the data and systematic errors. Furthermore, many galaxies in O11 and O15, as typical of low-mass galaxies, have significant kinematic disturbances that may make the density profiles unreliable. Nonetheless, the lower masses of these samples compared to our sample offer a valuable range to search for the correlations with galaxy properties.

In feedback models, the energy of supernovae pushes on the baryons, which are a substantial enough component of the total mass that when they move out, the gravitational potential of the entire galaxy changes, which subsequently alters the velocity distribution (and hence the density distribution) of the dark matter. Hence, if baryonic feedback indeed causes the flattening of the cusp, we would expect that the DM slope increases in galaxies with lower mass than ours. Moreover, one might expect this effect to depend more strongly on the maximum star formation rate reached by the galaxy in the past, and/or the burstiness of the overall star formation history, rather than strictly the stellar mass. We observe that the THINGS and LITTLE THINGS samples, which have lower mass than ours, have smaller slopes, and as shown in the results (4.4.2) and Figure 4.10, the inner DM profile slope increases with the galaxy dynamical mass and virial mass when we look at different samples (our sample, A14, O11 and O15) collectively, although we note that the correlation of α and M_{200} only exists when we use the Ch2 fitting results, whereas that of α and M_{dyn} only exists with the r-band results. Simulation results in the literature predict no trend between the DM slope and the mass in the range of $10^7 - 10^{11} M_\odot$ (Chan, T. K. et al. (2015)), which includes the range of galaxies in our samples, or only a slight trend (Governato, F. et al. (2012)), but the simulation in Governato, F. et al. (2012) contains few galaxies so the correlation may not be statistically significant. In addition, the lack of a trend between the slope and the stellar mass in the mass range from O11 and O15 to ours ($M_* \sim 10^{6.5} - 10^{10} M_\odot$) disfavors the simple baryonic feedback models. Depending on the history of the galaxies, events such as merging or collision may alter the mass structure and density profile and erase the correlation between mass and density profile slope. A sample with a wider range of redshift would better compare with the simulation results; however, observations with the necessary resolution for the central region would be challenging at larger redshifts. Thus, the results from our CO data in combination with the literatures indicate that baryonic feedback models alone cannot explain the observed DM density profiles. With our measurements, we are constraining the mass range over which baryonic feedback might be effective in altering the DM profile: if feedback is the cause of the shallow DM slopes, it must be similarly effective over $M_* \sim 10^{6.5} - 10^{10} M_\odot$ if it is the origin of the shallow DM slopes. We expect that the full Hα sample will help us determine the certainty of this trend.

Acknowledgments

We would like to thank Kristine Spekkens for the detailed instructions and discussion regarding DiskFit. Support for CARMA construction was derived from the states of California, Illinois, and Maryland, the James S. McDonnell Foundation, the Gordon and Betty Moore Foundation, the Kenneth T. and Eileen L. Norris Foundation, the University of Chicago, the Associates of the California Institute of Technology, and the National Science Foundation. The CARMA development and operations were supported by the National Science Foundation under a cooperative agreement, and by the CARMA partner universities. This work is based [in part] on observations made with the Spitzer Space Telescope, which is operated by the Jet Propulsion Laboratory, California Institute of Technology under a contract with NASA. Support for this work was partially from the NSF grant No. 1140031.

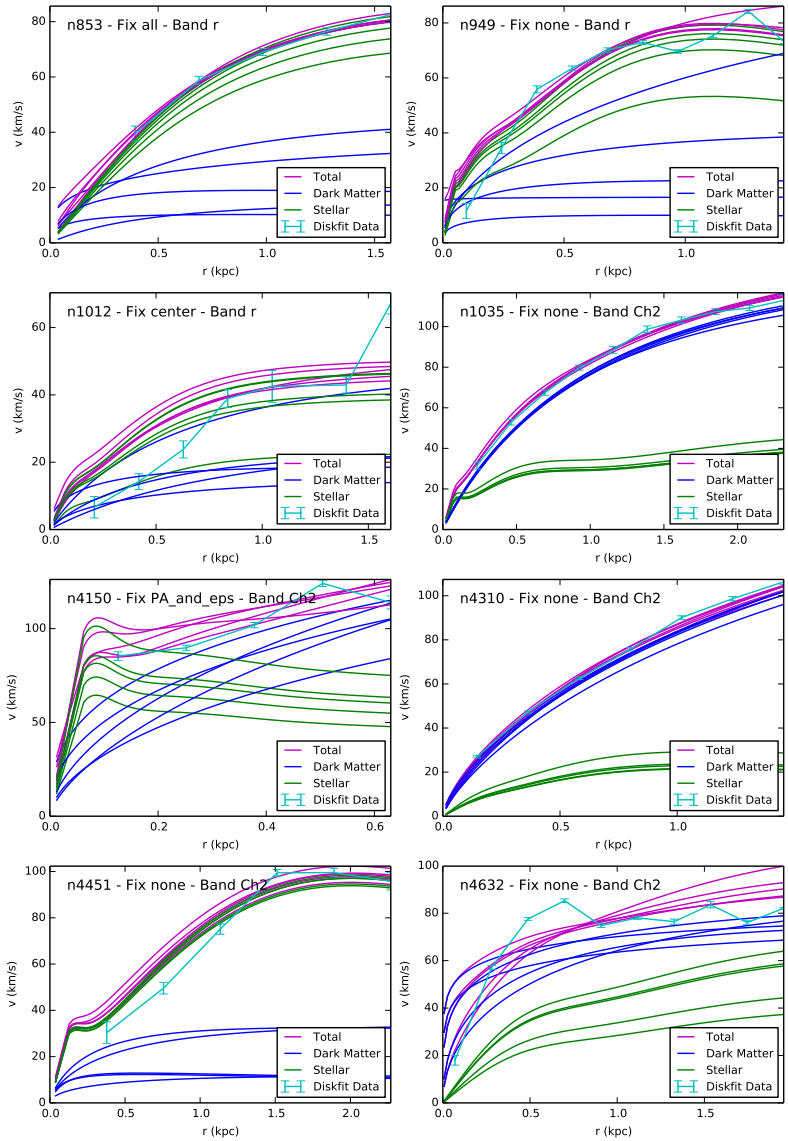

Figure 4.6: Example of gNFW fitting to CO data. The total rotation curve (magenta), which is fitted to the CO data (cyan) is the sum of two mass components in the gNFW model: stellar mass (green) and dark matter (blue). "Fix all", "Fix center", "Fix PA_and_eps" and "Fix none" indicate the fixed geometric parameters in the initialization of the fit to obtain the rotation curves; "Fix all" indicates that the PA, ellipticity (i.e., "eps") and center were fixed. The parameter constraints and covariances of the model were generated using the Markov Chain Monte Carlo (MCMC) method with the python-based software *emcee* (Foreman-Mackey, D. et al. (2013)), 100 walkers and 5000 steps. Five generated sets of parameters were randomly selected after the walkers began converging to plot the curves as shown.

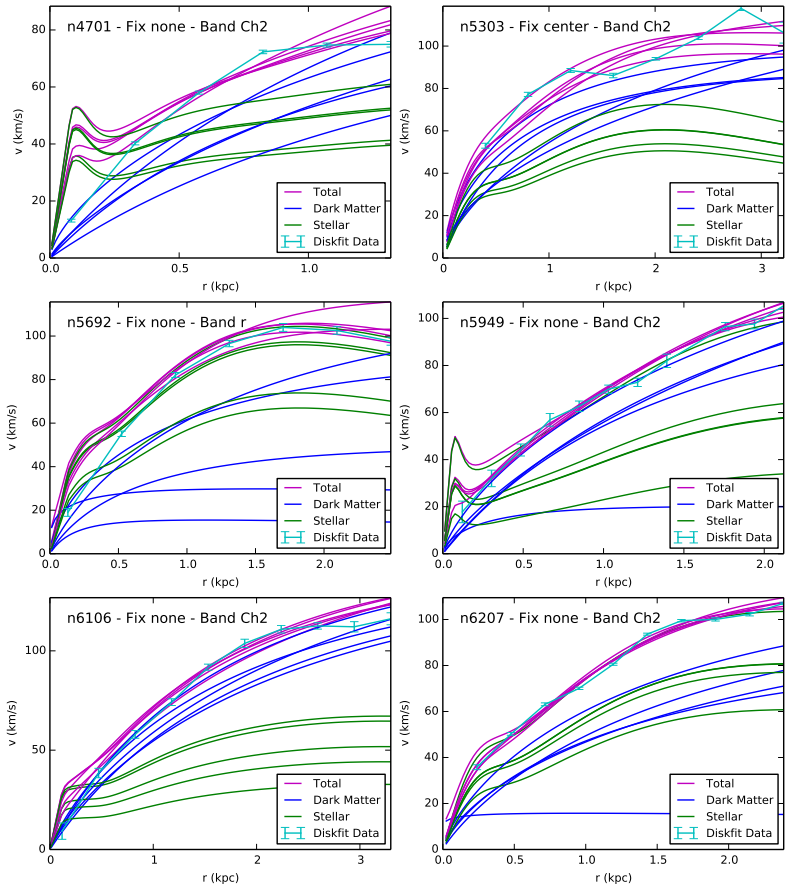

Figure 4.6: (cont.)

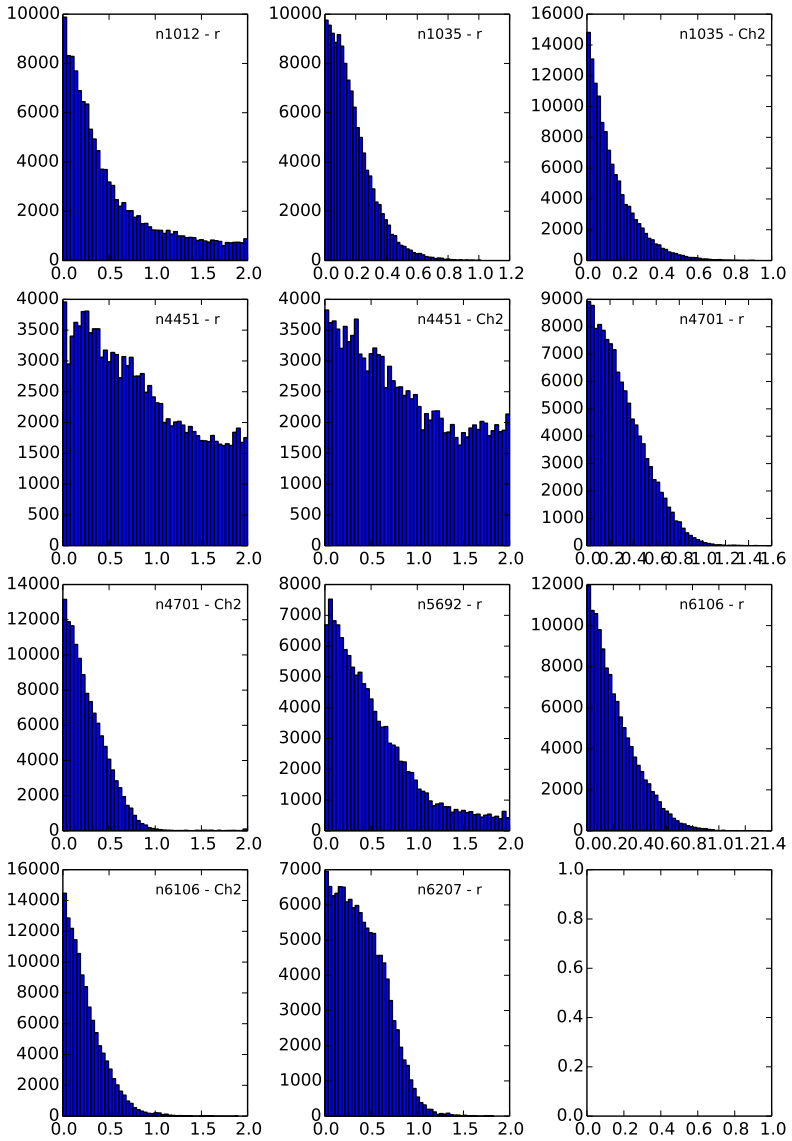

Figure 4.7: Histogram of the posterior distributions of the dark-matter inner profile slope α of the galaxies, whose only the 95% confidence level upper limit values are obtained (see Table 4.3).

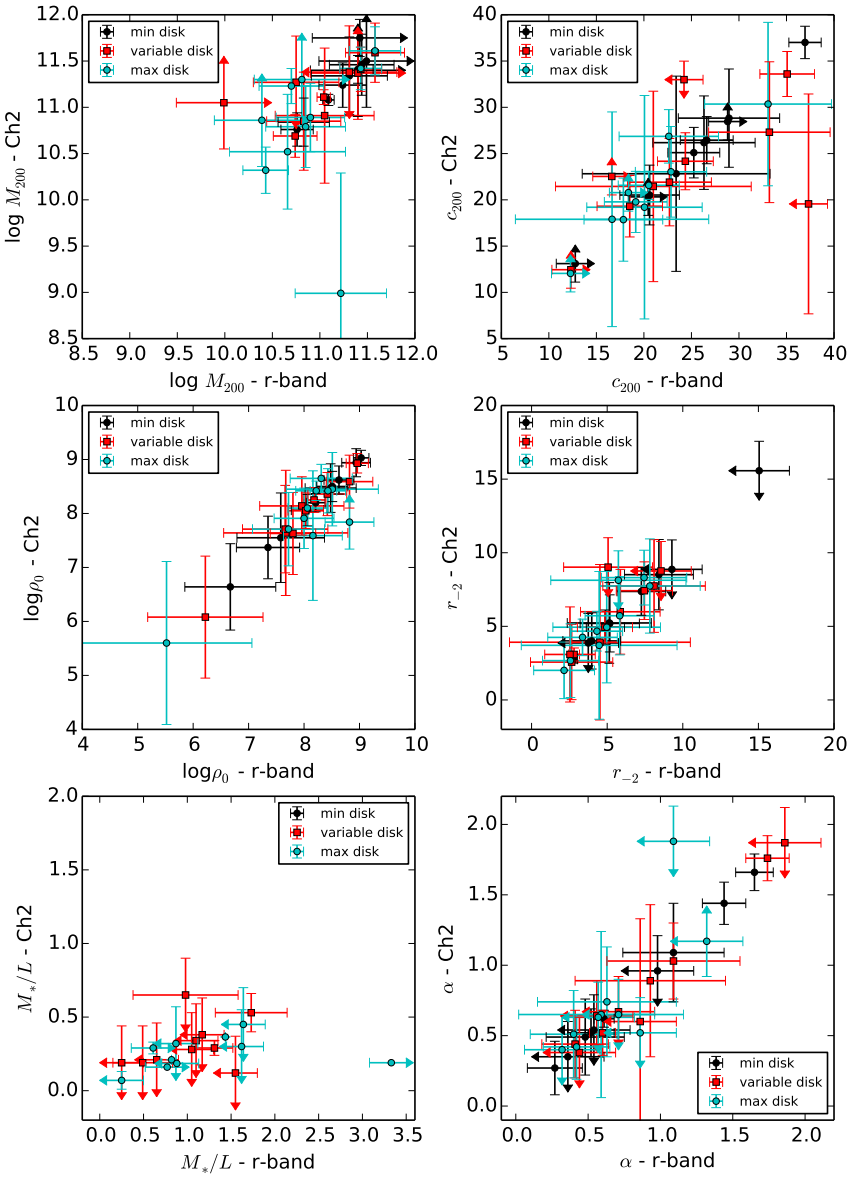

Figure 4.8: Comparison of the gNFW parameters for mass models constructed using different bands to trace the stellar component. The gNFW parameters are the virial mass ($\log M_{200}$), concentration (c_{200}), stellar mass-to-light ratio (M_*/L), density parameter ($\log \rho_0$), scale radius (r_s) and inner slope (α). The modeling is based on the CO kinematics with the stellar mass assumed to be proportional to the luminosity in either r-band data (horizontal axis) or IRAC channel-2 (denoted "Ch2") data (vertical axis). The parameters were fit for 3 models: minimum disk (black circles), maximum disk (cyan circles), and variable disk (red squares). The arrows indicate the upper and lower limits (the length of the arrow is only for visual purpose and is not related to any physical quantity). The plots show that all parameters except M_*/L are robust with respect to the choice of r-band or Ch2 data.

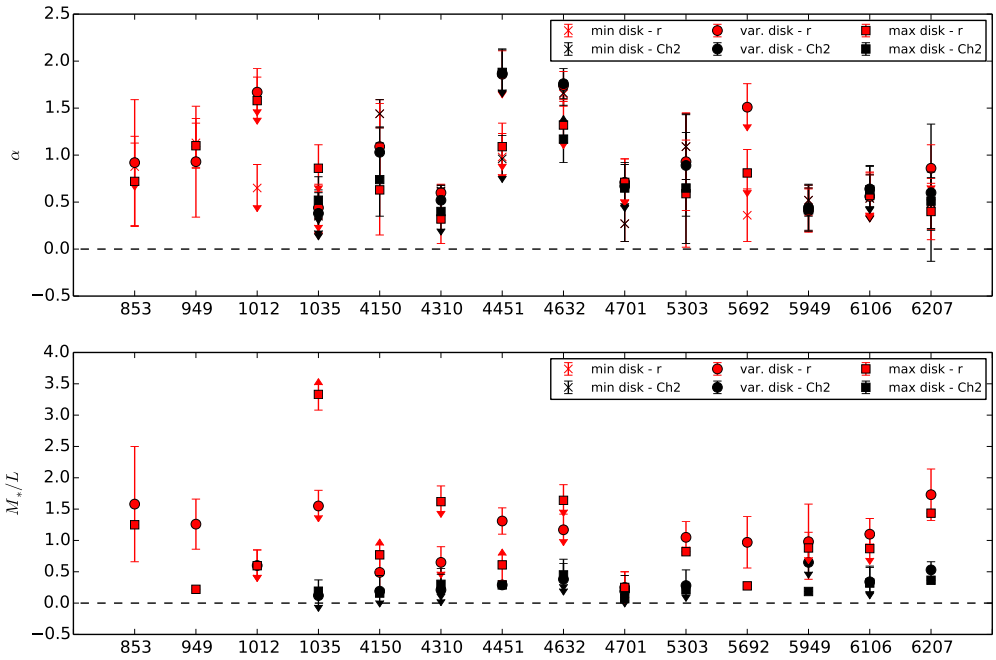

Figure 4.9: Values of the inner power-law slope α (top) and stellar mass-to-light ratios (bottom) of each galaxy in the sample for three fitting cases to the gNFW function: minimum disk (cross), variable disk (circle), and maximum disk (square). The parameters were obtained using either r-band data (black markers) or IRAC channel-2 ("Ch2") data (red markers) for the stellar mass. The arrows indicate the upper and lower limits (the length of the arrow is only for visual purpose and is not related to any physical quantity).

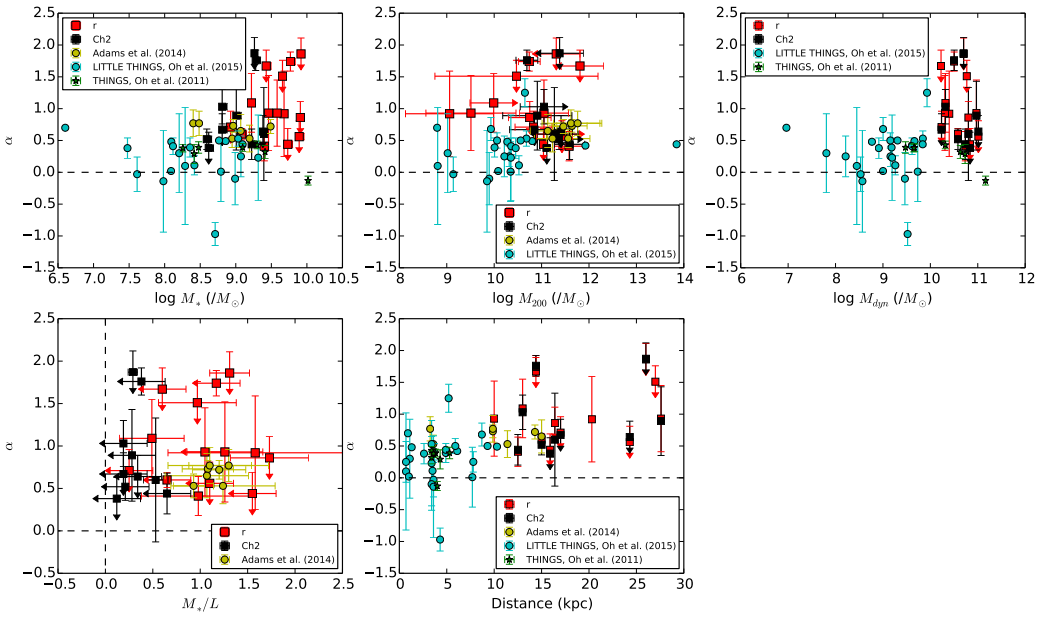

Figure 4.10: Correlations of the inner power-law slope α versus the virial mass, stellar mass-to-light ratios, dynamical mass, and distance of the galaxies in the sample. The survival analysis shows no statistically significant correlation between α and $\ln(M_*/L)$, but there are correlations between α and $\log M_{200}$, $\log M_{dyn}$, or distance. Our values are shown as red squares (r-band data) and black squares (IRAC channel-2 data), and the values from Adams, J.J. et al. (2014), Oh, S.-H. et al. (2011) and Oh, S.-H. et al. (2015) are shown as yellow circles, green stars and cyan circles, respectively. The arrows indicate the upper and lower limits (the length of the arrow is only for visual purpose and is not related to any physical quantity). Note that the Oh et al. studies measured α in a notably different way from our study.

Chapter 5

Addition data from ALMA and preliminary results

5.1 Data and rotation curves

In addition to the CO data from CARMA, we observed eight of the galaxies in the sample using the ALMA (Atacama Large Millimeter/submillimeter Array) interferometric array located in Atacama desert, Chile; the eight galaxies are NGC 1035, NGC 4150, NGC 4310, NGC 4451, NGC 4632, NGC 4701, NGC 5692, and NGC 6106. Our purpose was to increase the resolution and sensitivity of our data. The galaxies were observed during Cycle 3 of the ALMA scheduling period in 2015 and 2016. Compared to CARMA, ALMA has much greater sensitivity. Approximately 43 telescopes were in the array of ALMA when the observations were made. The entire program at CARMA took about 800 hrs of observing time, whereas the ALMA observations were completed in 9 hours. ALMA also has better imaging than CARMA because there are many more baselines per observation. For this ALMA dataset, the on-source observing time was approximately 15-30 minutes per source, yielding an rms sensitivity of about 9.2 mJy per source. The spectral resolution was 1.3 km s^{-1}. The angular resolution was approximately 2 arcsec, giving an average linear resolution of $\sim$ 150 pc. The data type was spectral line observations.

The ALMA data were reduced following similar MIRIAD algorithms as described in 3.3 and combined with CARMA data to make velocity maps for further analysis. The velocity maps of the galaxies produced from the combination of ALMA and CARMA data are shown in Figure 5.1, which show much better resolution, high level of detail and overall improved appearance of the CO distributions compared to the maps of CARMA data alone. The rotation curves (Figure 5.2) were produced from the velocity maps using DiskFit as previously described, with one exception: the velocity uncertainties at each pixel were estimated to be uniformly 10 km s^{-1} throughout the maps instead of calculated from Equation 3.1 to obtain a reasonable reduced $\chi^2 \sim 1$ for every rotation curve fit. This estimate of velocity uncertainty is in the same order of magnitude with the calculated values from Equation 3.1 but simplifies the procedure of rotation curve fitting. All galaxies were fit with the radial

model with $m = 0$ and without the radial component for the outer radii where data are scarce, as previously done. All parameters (PA, center, ellipticity and systemic velocity) were initialized with the values in Table 4.1, allowed to be varied in the fit, and adjusted until the results converge. The only exception is NGC 4150, which was was completely fit without the radial component because of its small CO extent, and the PA and ellipticity were kept fixed to their initializations.

The results, as shown in Figure 5.2, are mostly consistent with the rotation curves produced from only CARMA data. We note that the higher resolution of ALMA data reveals a ring structure in NGC 4150 (Figure 5.1) and a less steep rotation curve, but the CO extent remains at less than 1 kpc. In addition, the rotation curves of NGC 4310 and NGC 4701 appear steeper than those obtained from only CARMA data.

5.2 Preliminary mass modeling results and discussion

We applied the same mass-modeling algorithm described in 4.3 to fit the rotation curves from ALMA and CARMA data to the gNFW model. All parameter initializations and limits are identical to those used for only CARMA data, and we did not fit for the minimum- and maximum-disk cases, assuming that the small changes in rotation curves do not significantly change the results of the limiting cases. Figure 5.3 shows examples of the gNFW fitting, using either r-band or IRAC Ch2 data to extract the stellar mass contribution. Compared to the mass modeling fits with only CARMA data (Figure 4.6), NGC 1035 and NGC 6106 still have good fits in both cases of r-band and Ch2; NGC 4310 has similarly good fits in Ch2; the fits for NGC 4451 and NGC 4632 have notably improved; the fits for NGC 4701 have improved but are still incorrect in the inner 1 kpc because of the strong emission feature in the optical; the fits of NGC 4150 and NGC 5692 have become worse. The values listed in Table 5.1 show overall improvement in the fits, as expected from better-resolution data: NGC 1035 no longer has only upper limits reported for α in r-band and Ch2; in particular, NGC 1035, which has a steeply rising rotation curve, now has a relatively high slope value (0.64 in r-band and 0.50 in Ch2), which confirms that its odd behavior mentioned in 4.4 was due to the lower resolution of the data. Similarly, NGC 5692 and NGC 6106 no longer have only upper limits for α in the r-band, which means their posterior distributions do not get pushed to the limits, despite the fit of NGC 5692 looks bad in Figure 5.3. However, note that only the upper limit of α is reported for NGC 4310 now, which means the fit for this particular galaxy has become worse with the increase in sensitivity of the data, possibly because the assumption of uniform velocity uncertainty in the rotation curve fitting is not applicable for this galaxy (which makes the rotation curve less smoothly rising in the outer radii, as shown in Figure 5.2), or the assumption of a thin disk does not apply because NGC 4310 is an early-type galaxy. Furthermore, consistent with Figure 4.6, all of these galaxies are dark-matter dominated, except NGC 4150 and NGC 4701, which have large stellar contribution up to 0.4 kpc and 2 kpc, respectively.

Table 5.1: Constraints on the mass distribution from models with a gNFW halo and variable disk, using the combination of ALMA and CARMA data

(1) Name	(2) α	(3) $\log M_{200}$ $/(M_\odot)$	(4) c_{200}	(5) M_*/L $(M_\odot/L_\odot)$	(6) r_{-2} (kpc)	(7) $\log \rho_0$ $/(M_\odot$ kpc$^{-3})$
r-band						
NGC1035	0.64 ± 0.39	11.31 ± 0.22	16.15 ± 4.20	0.73 ± 0.58	7.52 ± 4.20	7.68 ± 0.55
NGC4150†	0.71 ± 0.61	11.28 ± 0.47	29.77 ± 6.99	0.54 ± 0.54	3.84 ± 2.64	8.21 ± 1.06
NGC4310	<0.53	>11.26	14.69 ± 1.32	<0.41	11.96 ± 2.98	7.97 ± 0.23
NGC4451	<0.88	11.53 ± 0.37	13.03 ± 2.83	<0.56	11.08 ± 4.37	7.76 ± 0.31
NGC4632	1.10 ± 0.68	10.32 ± 0.45	30.29 ± 10.95	>0.23	1.87 ± 1.35	7.82 ± 1.36
NGC4701	<1.58	10.65 ± 1.32	20.35 ± 9.44	0.92 ± 0.49	3.24 ± 3.74	7.96 ± 0.71
NGC5692	0.69 ± 0.67	10.89 ± 0.67	<36.01	<1.03	4.39 ± 5.42	7.73 ± 0.87
NGC6106	0.25 ± 0.25	11.61 ± 0.22	12.99 ± 2.19	<0.64	11.81 ± 4.05	7.75 ± 0.27
IRAC Ch2 (4.5μm)						
NGC1035	0.50 ±0.32	11.50 ± 0.23	<20.77	<0.25	9.87 ± 5.46	7.66 ± 0.45
NGC4150†	0.68 ± 0.64	11.27 ± 0.49	29.44 ± 10.69	<0.34	3.85 ± 2.69	8.24 ± 1.10
NGC4310	<0.57	>11.16	14.14 ± 1.29	<0.11	12.48 ± 3.44	7.93 ± 0.24
NGC4451	<0.97	11.51 ± 0.49	12.40 ± 3.34	<0.15	11.46 ± 5.21	7.71 ± 0.29
NGC4632	1.04 ± 0.69	9.73 ± 1.11	27.00 ± 10.58	0.49 ± 0.23	<4.41	7.73 ± 1.36
NGC4701	<1.27	10.83 ± 0.51	22.23 ± 8.17	<0.37	3.65 ± 3.77	8.15 ± 0.67
NGC5692	-	-	-	-	-	-
NGC6106	<0.65	11.65 ± 0.22	12.43 ± 1.97	<0.16	12.73 ± 3.91	8.3 ± 0.4

Note. — †: the PA and ellipticity were fixed in DiskFit to obtain the rotation curves. For all other galaxies, the rotation curves were obtained with no fixed geometric parameter.
Columns (2-5) show the MCMC best-fit results of the rotation curves to the gNFW function in terms of the inner power-law slope α, virial mass M_{200} in the logarithmic scale, concentration c_{200}, and stellar mass-to-light ratio M_*/L, respectively. The characteristic radius $r_{-2} = (2-\alpha)r_s$ and the log density in columns (6) and (7) were calculated from M_{200} and c_{200}.

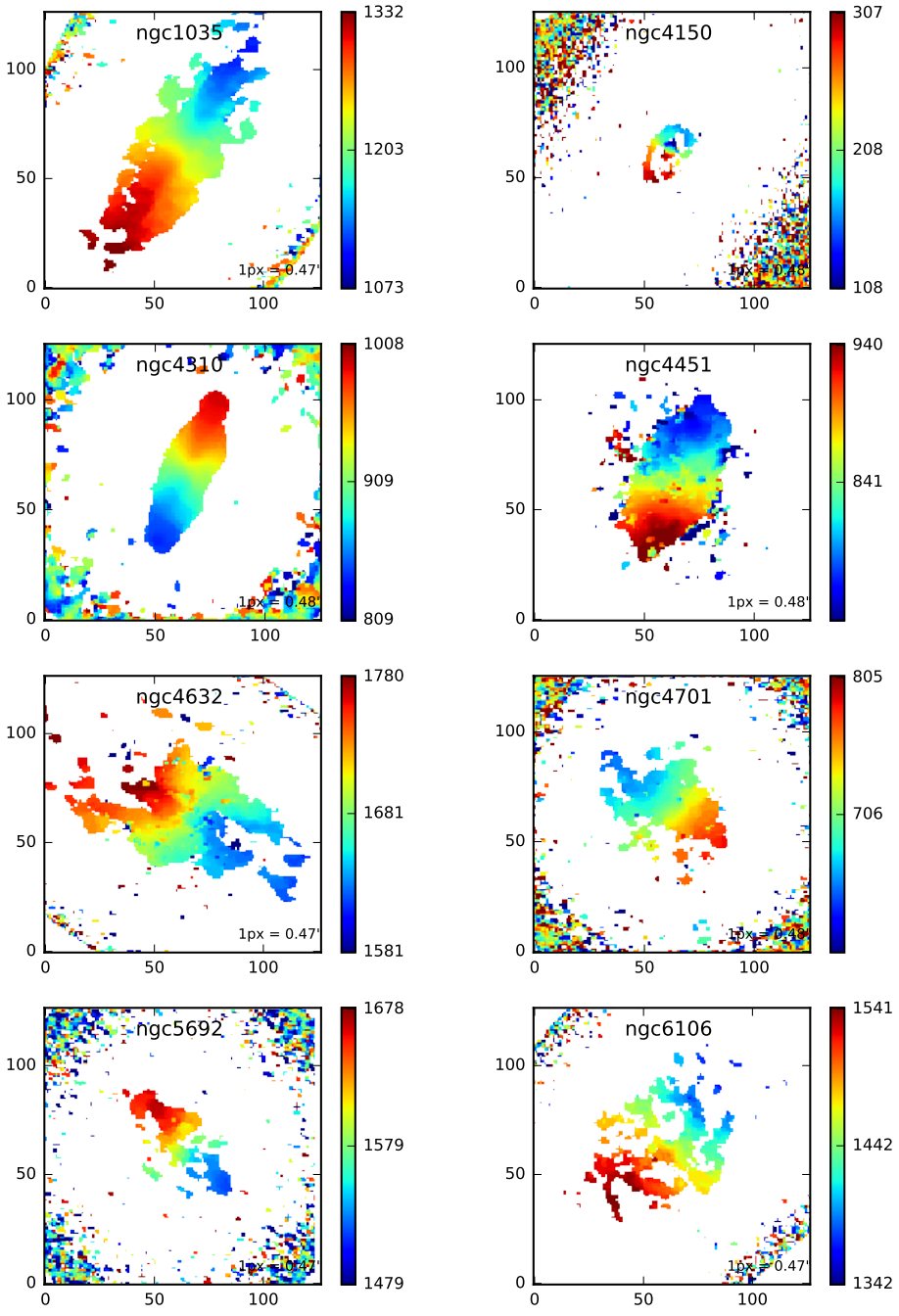

Figure 5.1: Naturally weighted CO(1-0) intensity and velocity distribution maps with masking to enhance the SNR. The data are a combination of observations from CARMA and ALMA. For all galaxies, the RA offset is from +30" (left) to -30" (right), the Dec offset is from -30" (bottom) to +30" (top). The side bar indicates the velocity (in km/s) in the distribution, and the units of the image are pixels.

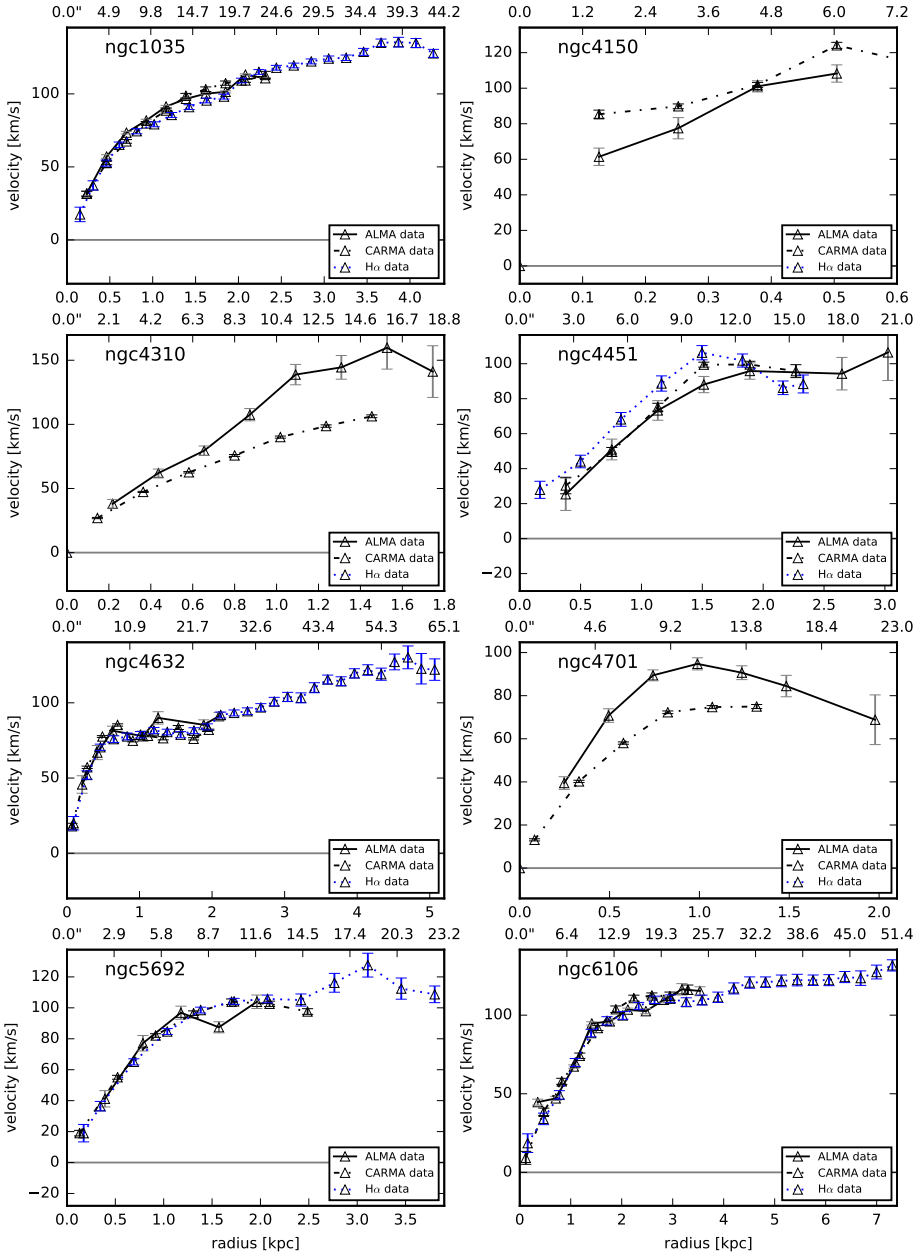

Figure 5.2: Rotation curves of the galaxies, obtained from fitting the ALMA and CARMA data using DiskFit in the radial mode with $m = 0$. The exception is NGC 4150, which was fit without the radial component due to the small CO extent. The solid line denotes the combination of ALMA and CARMA data, the black dashed line denotes the CARMA data, and the blue dotted line denotes the Hα data when available.

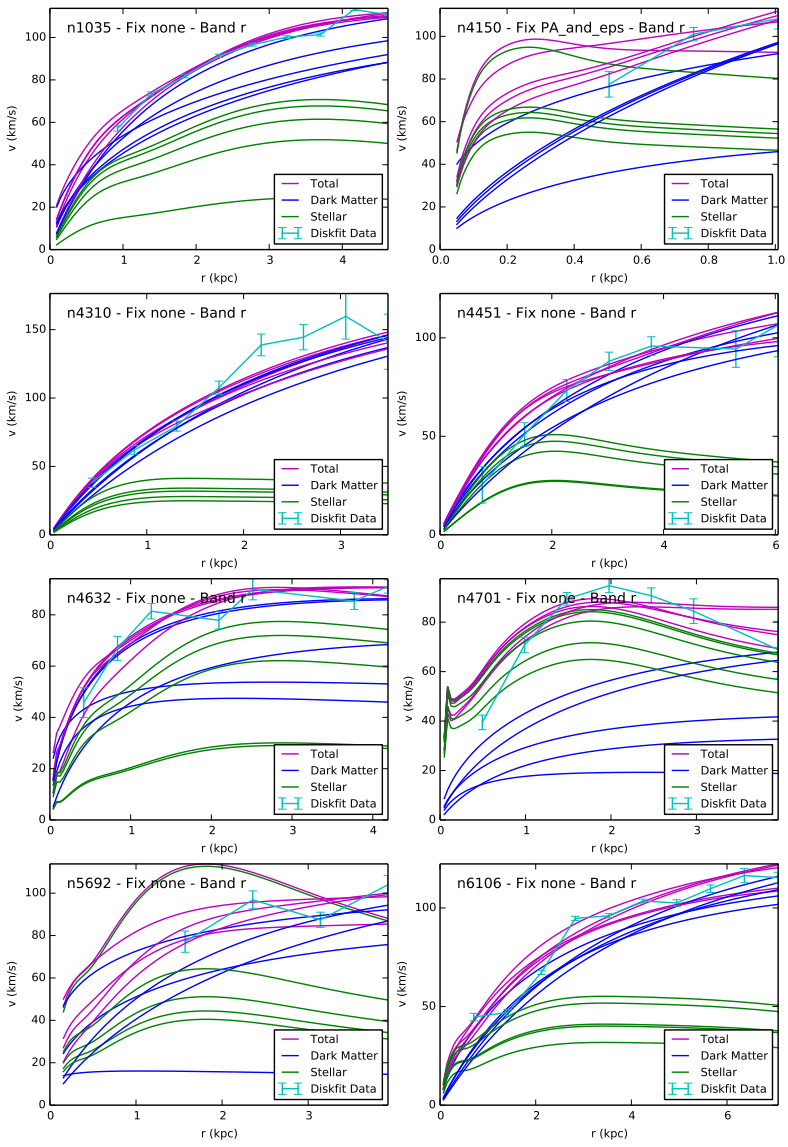

Figure 5.3: Example of gNFW fitting to the combination of ALMA and CARMA data. The stellar mass was fit using r-band data. The total rotation curve (magenta), which is fitted to the data (cyan) is the sum of two mass components in the gNFW model: stellar mass (green) and dark matter (blue). "Fix PA_and_eps" and "Fix none" indicate the fixed geometric parameters in the initialization of the fit to obtain the rotation curves. The parameter constraints and covariances of the model were generated using the Markov Chain Monte Carlo (MCMC) method with the python-based software *emcee* (Foreman-Mackey, D. et al. (2013)), 100 walkers and 5000 steps. Five generated sets of parameters were randomly selected after the walkers began converging to plot the curves as shown.

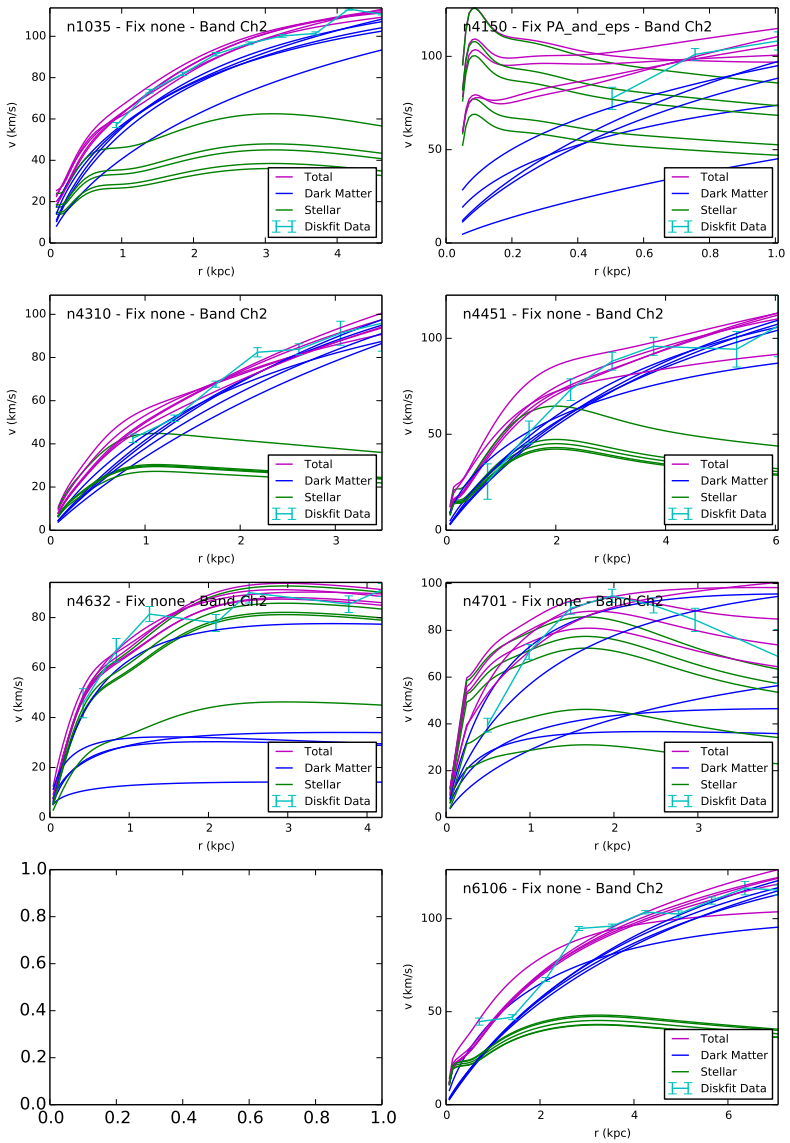

Figure 5.3: (Cont.) Example of gNFW fitting to the combination of ALMA and CARMA data. The stellar mass was fit using Ch2-band data. All other settings are similar to those in the case with r-band data.

As shown in Figure 5.4, all parameters of the gNFW model (except the stellar mass-to-light ratio) still remain robust regardless of whether r-band or Ch2 data are used. To examine the change in behavior of each galaxy, we plot the results of α, M_*/L and $\log M_{200}$ in Figure 5.5. In general, with the ALMA data, the slope decreases, the stellar mass-to-light ratio decreases, but the virial mass remains approximately the same. The difference between Ch2 and r-band values also appears to decrease for the stellar mass-to-light ratio. In particular, the DM slope of NGC 4632, which has the steepest slope ($\alpha \sim 1.7 \pm 0.2$) based on the CARMA data, has now significantly decreased to $\sim 1.0 \pm 0.7$; nonetheless, the two values are within the 1σ uncertainty level of each other and both indicate the steep NFW-like slope of the DM inner profile.

The mean of the sample is also calculated by approximating a Gaussian distribution for the entire sample (4.3). With the ALMA data, the mean α of the eight galaxies is 0.24 ± 0.08 (r-band) and 0.08 ± 0.03 (Ch2). These values are significantly lower than the mean values calculated from only CARMA data: for the same galaxies, $\alpha = 0.73 \pm 0.65$ (r-band) and 0.74 ± 0.69 (Ch2). Considering the bad fits in both cases of data, we also calculate the entire sample average based on a mixture of the galaxies with good fits in at least the CARMA or the CARMA-ALMA dataset, i.e., the sample to calculate the Gaussian distribution is composed of: (a) with r-band stellar contribution: NGC 853, NGC 949, NGC 4150, NGC 4310, NGC 5303, NGC 5692, NGC 5949, and NGC 6207 from CARMA data, and NGC 1035, NGC 4451, NGC 4632, NGC 4701 and NGC 6106 from CARMA-ALMA data; (b) with Ch2 stellar contribution: NGC 4150, NGC 4310, NGC 5303, NGC 5949, and NGC 6207 from CARMA data, and NGC 1035, NGC 4451, NGC 4632, NGC 4701 and NGC 6106 from CARMA-ALMA data. (NGC 1012 is excluded from the sample due to its bad fit with the CARMA data, the small extension and patchy distribution of CO data, and the lack of ALMA data.) The average slope of the sample with only good fits is 0.45 ± 0.16 (r-band, 13 galaxies), 0.44 ± 0.15 (r-band, 10 galaxies with Ch2 data), and 0.11 ± 0.04 (Ch2). Hence, the average slope of the sample decreases compared to when only CARMA data is used, especially with the stellar contribution deduced from Ch2 data, and the slope is no longer robust with whether r-band or Ch2 data is used.

We also computed the correlation between the DM slope and the stellar mass, following the method described in 4.4, using the galaxies with good gNFW fits from both CARMA and ALMA (as listed above), and the results of Adams, J.J. et al. (2014), Oh, S.-H. et al. (2011) and Oh, S.-H. et al. (2015). The correlations are as follows:

$$\alpha = 0.19 \log M_* - 1.24 \qquad (r\text{-band, A14, O11, O15}); \; p = 0.07 \tag{5.1}$$

$$\alpha = 0.12 \log M_* - 0.61 \qquad (\text{Ch2, A14, O11, O15}); \; p = 0.46 \tag{5.2}$$

Thus, with the higher-resolution and better-fit data, there is still no statistically significant correlation between the slope and the stellar mass for the combined sample, which spans a mass range of $M_* \sim 10^{6.5} - 10^{10} M_\odot$. The difference in significance level (p-value) may be due to the difference in sample size: there are more galaxies in our sample with r-band data

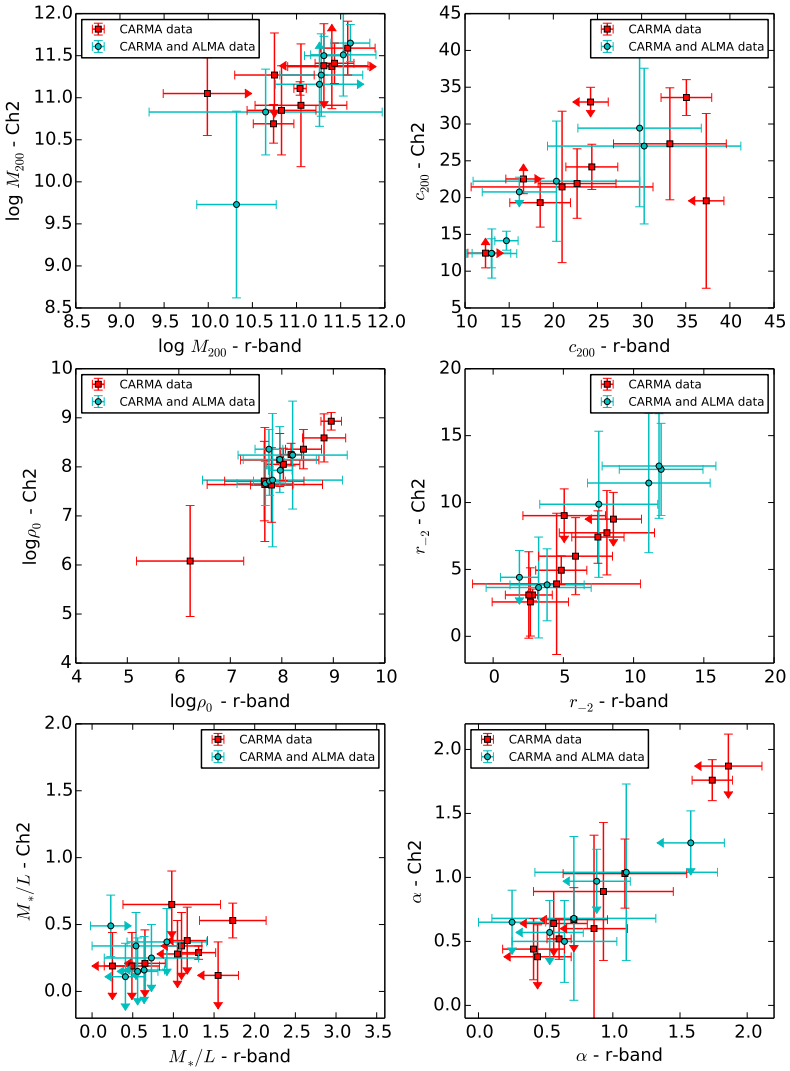

Figure 5.4: Comparison of the gNFW parameters for mass models constructed using different bands to trace the stellar component and different molecular gas datasets to trace the total matter distribution. The gNFW parameters are the virial mass ($\log M_{200}$), concentration (c_{200}), stellar mass-to-light ratio (M_*/L), density parameter ($\log \rho_0$), scale radius (r_s) and inner slope (α). The modeling is based on the CO kinematics, which is deduced from CARMA dataset (red circles) or a combination of CARMA and ALMA data (cyan circles), with the stellar mass assumed to be proportional to the luminosity in either r-band data (horizontal axis) or IRAC channel-2 (denoted "Ch2") data (vertical axis). The parameters were fit for variable disks (i.e., M_*/L was not fixed). The arrows indicate the upper and lower limits (the length of the arrow is only for visual purpose and is not related to any physical quantity). The plots show that all parameters except M_*/L are robust with respect to the choice of r-band or Ch2 data.

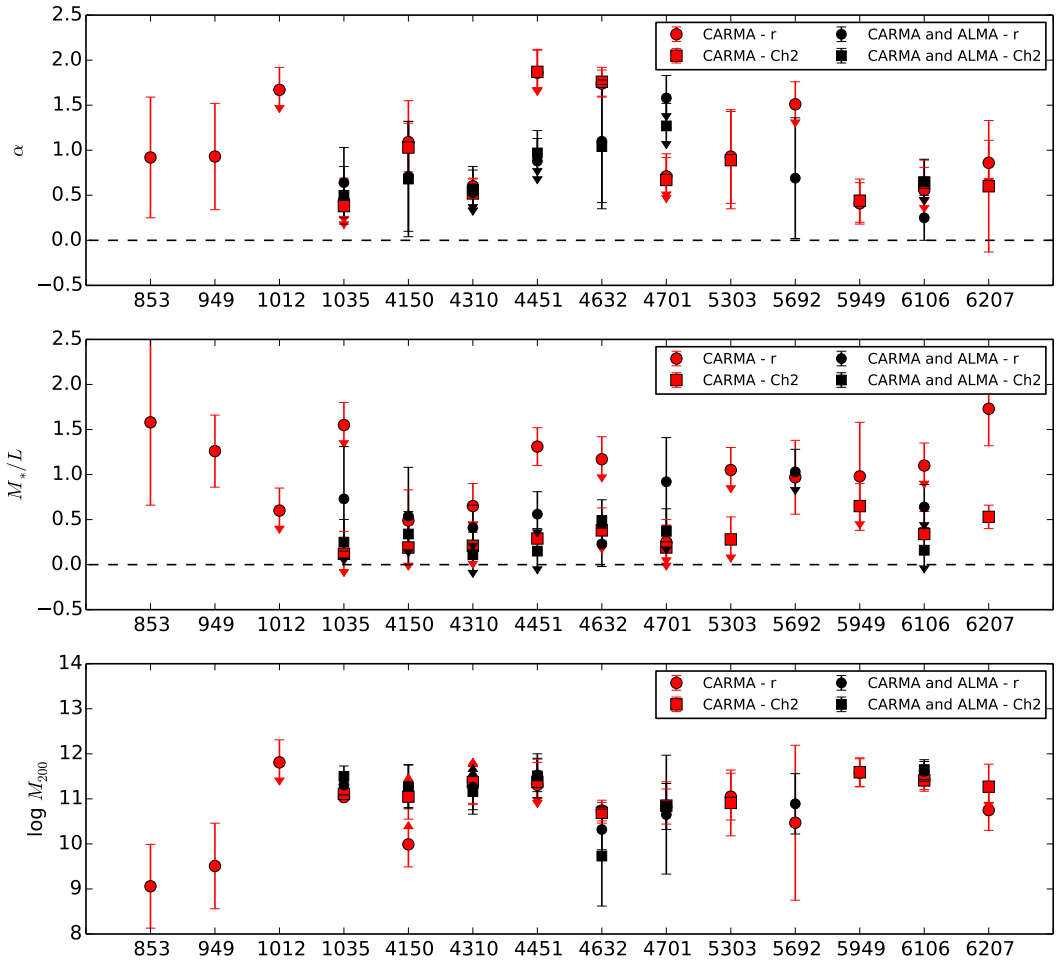

Figure 5.5: Values of the inner power-law slope α (top), stellar mass-to-light ratios (middle) and virial mass ($\log M_{200}$) of each galaxy in the sample to the gNFW function. The parameters were obtained using either r-band data (black markers) or IRAC channel-2 ("Ch2") data (red markers) for the stellar mass. The arrows indicate the upper and lower limits (the length of the arrow is only for visual purpose and is not related to any physical quantity).

than Ch2 data. In other words, the results of the combination of ALMA and CARMA data with better resolution confirm the results of CARMA alone. With the full Hα data sample (11 additional galaxies), we are more likely to obtain a statistically significant correlation of the DM inner slope with other quantities, particularly the mass, of the galaxies, if such correlations exist, in order to confirm the validity of mechanisms such as baryonic feedback in flattening the cusp in the density profile of dark-matter-dominated galaxies.

Acknowledgments

We would like to especially thank Melvyn Wright for the ALMA data reduction. Support for CARMA construction was derived from the states of California, Illinois, and Maryland, the James S. McDonnell Foundation, the Gordon and Betty Moore Foundation, the Kenneth T. and Eileen L. Norris Foundation, the University of Chicago, the Associates of the California Institute of Technology, and the National Science Foundation. The CARMA development and operations were supported by the National Science Foundation under a cooperative agreement, and by the CARMA partner universities. This work is based [in part] on observations made with the Spitzer Space Telescope, which is operated by the Jet Propulsion Laboratory, California Institute of Technology under a contract with NASA. Support for this work was partially from the NSF grant No. 1140031. This paper makes use of the following ALMA data: ADS/JAO.ALMA#2013.1.00616.S. ALMA is a partnership of ESO (representing its member states), NSF (USA) and NINS (Japan), together with NRC (Canada), NSC and ASIAA (Taiwan), and KASI (Republic of Korea), in cooperation with the Republic of Chile. The Joint ALMA Observatory is operated by ESO, AUI/NRAO and NAOJ. The National Radio Astronomy Observatory is a facility of the National Science Foundation operated under cooperative agreement by Associated Universities, Inc.

Chapter 6

Summary and Conclusions

We report the detection of CO molecular gas in 14 nearby dwarf galaxies, including 6 galaxies that were previously detected in CO in single-dish measurements. We also present the upper limits for another 12 dwarf galaxies that we did not detect, 2 of which were detected in the published single-dish measurements in the literature, which we believe we did not detect because of weather conditions and lack of sufficient observing time. Most of the detections are late-type spiral galaxies. We compare the CO flux with the mid- and far-IR flux from the WISE catalog and observe a correlation that the mid-IR flux may be a better indication than the far-IR flux of whether a galaxy contains sufficient CO for detection at the level of instrument sensitivity of CARMA, but not necessarily a better indicator of how much CO there is in the target. This correlation might prove to be useful in future studies to help choosing other CO targets for observation. We also observe a weak correlation among the molecular content, dynamical mass, r-band luminosity and size of the galaxies.

Using the intensity and velocity maps of the 14 CO-detected galaxies, we derive the CO rotation curves. Then, combined with the stellar rotation curves from optical and near-IR imaging data, we apply mass modeling and infer the dark matter profiles. The full Hα sample will also be provided in future studies, with a comparison between CO and Hα velocity fields and rotation curves of these galaxies.

Using high-spectral-resolution CO observations from CARMA and ALMA and the kinematic modeling code DiskFit, we model the velocity fields of 14 nearby dwarf galaxies. The molecular gas is generally limited to the central 30 arcsec of each galaxy, corresponding to a radial extent of 1-3 kpc. All targets can be reasonably fit with an axisymmetric model with radial flow. Large uncertainties were obtained for galaxies with low SNR, patchy distributions and/or holes in the gas distribution near the center of the galaxy. In general, the CO rotation curves are consistent with the Hα rotation curves of the same galaxies. The radial (noncircular) are generally small, mostly below 10 km s^{-1}.

We verify the consistency between two fitting programs: DiskFit (Spekkens, K. & Sellwood, J.A. (2007)) and RingFit (Simon, J.D. et al. (2003)). We observe that DiskFit provides more flexibility: (i) all physical parameters can be fit in the programs instead of being fixed input values; (ii) both axisymmetric and non-axisymmetric models can be used (although in

our case, the axisymmetric model with radial flow produces sensible rotation curves without invoking a bar structure or lop-sided flow). We note that the inflexibility of RingFit was an intentional choice, with the reasoning that the geometry of a galaxy can be measured more accurately from high-SNR images than from low-SNR velocity fields of an irregular gas distribution. Hence, the flexibility is not necessarily an advantage of DiskFit, as shown in a few cases when some or all geometric parameters must be fixed to obtain a reasonable rotation curve.

Using the CO rotation curves and an MCMC fitting algorithm, we model the velocity profiles with a generalized NFW function and determine the inner power-law slope of the density profile. The results of CARMA data show that the inner power-law slope varies over a large range from below 0.38 to 1.76, with the average $\alpha = 0.64 \pm 0.49$, which is consistent with the results of Adams, J.J. et al. (2014) ($0.30 \leq \alpha \leq 0.88$ and average $\alpha = 0.58 \pm 0.24$ or $\alpha = 0.67 \pm 0.10$ based on the gas or star dynamics model, respectively). With the additional ALMA data for eight galaxies in the sample, and if we exclude NGC 1012 which has a bad fit to the gNFW model, the average slope of our sample decreases to 0.45 ± 0.16. In comparison, the average α values calculated by previous studies include: 0.73 ± 0.44 (Simon, J.D. et al. (2005), 5 galaxies), 0.29 ± 0.07 (Oh, S.-H. et al. (2011), 7 galaxies), and 0.32 ± 0.24 (Oh, S.-H. et al. (2015), 26 galaxies). Thus, there is a difference in results due to our methodologies: $\alpha \sim 0.6$ (our study, Simon, J.D. et al. (2005) and Adams, J.J. et al. (2014)) versus $\alpha \sim 0.3$ (Oh, S.-H. et al. (2011) and Oh, S.-H. et al. (2015)).

On one hand, we have selected a sample of well-behaved galaxies, and our method to analyze them is unbiased with respect to cored vs. cuspy profiles. Among our galaxies, 5 have cuspier profiles ($\alpha \geq 0.7$, with NGC 4632 being especially cuspy), and 9 have shallower profiles, which show that dwarf galaxies similar in size (dynamical mass $\sim 10^9 M_\odot$) can have notably different density profiles in the central region. On the other hand, the methodology in Oh, S.-H. et al. (2011) and Oh, S.-H. et al. (2015) may be biased towards shallower slopes: the density profile slopes are calculated using only data within the so-called break radius (up to 1 kpc), which may be subject to low resolution in the data and systematic errors. Furthermore, many galaxies in Oh, S.-H. et al. (2011) and Oh, S.-H. et al. (2015), as typical of low-mass galaxies, have significant kinematic disturbances that may make the density profiles unreliable. Nonetheless, the lower masses of these samples compared to our sample offer a valuable range to search for the correlations with galaxy properties.

In feedback models, the energy of supernova pushes dark matter away from the central region and consequently decrease the DM slope from the NFW profile value. Hence, if baryonic feedback indeed causes the flattening of the cusp, we would expect that the DM slope increases in galaxies with lower mass than ours. However, the THINGS and LITTLE THINGS samples, which have lower mass than ours, have smaller slopes, and as shown in the results (4.4.2) and Figure 4.10, the inner DM profile slope increases with the galaxy dynamical mass and virial mass when we look at different samples (our sample, Adams, J.J. et al. (2014), Oh, S.-H. et al. (2011) and Oh, S.-H. et al. (2015)) collectively, although we note that the correlation of α and M_{200} only exists when we use the Ch2 fitting results, whereas that of α and M_{dyn} only exists with the r-band results. Simulation results in the

literature predict no trend between the DM slope and the mass in the range of $10^7 - 10^{11} M_\odot$ (Chan, T. K. et al. (2015)), which includes the range of galaxies in our samples, or only a slight trend (Governato, F. et al. (2012)), but the simulation in Governato, F. et al. (2012) contains few galaxies so the correlation may not be statistically significant. In addition, the lack of a trend between the slope and the stellar mass in the mass range from Oh, S.-H. et al. (2011) and Oh, S.-H. et al. (2015) to ours ($M_* \sim 10^{6.5} - 10^{10} M_\odot$) suggests against the effect of baryonic feedbacks. Thus, the results from our CO data in combination with the literatures indicate that baryonic feedback models alone cannot explain the observed DM density profiles. With our measurements, we are constraining the mass range over which baryonic feedback might be effective in altering the DM profile: if feedback is the cause of the shallow DM slopes, it must be similarly effective over $M_* \sim 10^{6.5} - 10^{10} M_\odot$ if it is the origin of the shallow DM slopes. We expect that the full Hα sample will help us determine the certainty of this trend.

Bibliography

Adams, J.J., Simon, J.D., Fabricius, M.H., et al. 2014, Astrophysical Journal, 789
Akritas, M.G., Murphy, S. A., & LaValley, M.P. 1995, Journal of the American Statistical Association, 90
Andreani, P., Casoli, F., & Gerin, M. 1995, Astronomy and Astrophysics, 300
Arraki, K. S., Klypin, A., More, S., & Trujillo-Gomez, S. 2014, Monthly Notices of the Royal Astronomical Society, 438
Begeman, K.G. 1989, Astronomy and Astrophysics, 223
Begeman, K.G., Broeils, A.H., & Sanders, R. H. 1991, Monthly Notices of the Royal Astronomical Society, 249, 523
Bolatto, A.D., Simon, J.D., Leroy, A.K., & Blitz, L. 2002, Astrophysical Journal, 565
Borriello, A., & Salucci, P. 2001, Monthly Notices of the Royal Astronomical Society, 323
Boylan-Kolchin, M., Bullock, J.S., & Kaplinghat, M. 2012, Monthly Notices of the Royal Astronomical Society, 422
Cappellari, M. 2002, Monthly Notices of the Royal Astronomical Society, 333
Chan, T. K., Keres, D., Onorbe, J., et al. 2015, Monthly Notices of the Royal Astronomical Society, 454
Chen, S.-R., Schive, H.-Y., & Chiueh, T. 2017, Monthly Notices of the Royal Astronomical Society, 468
Clowe, D., Gonzalez, A., & Markevich, M. 2003, Astrophysical Journal, 604
Dame, T. 1993, AIP Conference Proceedings, 278
de Blok, W. J. G. 2010, Advances in Astronomy
de Blok, W. J. G., & Bosma, A. 2002, Astronomy and Astrophysics, 385
de Blok, W. J. G., & McGaugh, S. S. 1997, Monthly Notices of the Royal Astronomical Society, 290
de Blok, W. J. G., McGaugh, S. S., Bosma, A., & Rubin, V. C. 2001a, Astrophysical Journal, 552
de Blok, W. J. G., McGaugh, S. S., & Rubin, V. C. 2001b, Astronomical Journal, 122
de Blok, W. J. G., McGaugh, S. S., & van der Hulst, J.M. 1996, Monthly Notices of the Royal Astronomical Society, 283
Di Cintio, A., Brook, C.B., Macciò, A.V., et al. 2014, Monthly Notices of the Royal Astronomical Society, 437
El-Zant, A., Shlosman, I., & Hoffman, Y. 2001, Astrophysical Journal, 560

Flores, R.A., & Primack, J.R. 1994, Astrophysical Journal, 427
Foot, R. 2015, Physical Review D, 91
Foreman-Mackey, D., Hogg, D.W., Lang, D., & Goodman, J. 2013, Instrumentation and Methods for Astrophysics (astro-ph.IM), arXiv:1202.3665
Gentile, G., Salucci, P., Klein, U., Vergani, D., & Kalberla, P. 2004, Monthly Notices of the Royal Astronomical Society, 351
Governato, F., Brook, C., Mayer, L., et al. 2010, Nature, 463
Governato, F., Zolotov, A., Pontzen, A., et al. 2012, Monthly Notices of the Royal Astronomical Society, 422
Helsel, D. 2005
Hernquist, L. 1990, Astrophysical Journal, 356
Jarosik, N., Bennett, C. L., Dunkley, J., et al. 2011, Astrophysical Journal Supplement, 192
Jarrett, T. H., Cohen, M., Masci, F., et al. 2011, Astrophysical Journal, 735
Kaplinghat, M. 2005, Physical Review D, 72
Karachentsev, I. D., Makarov, D. I., Sharina, M. E., et al. 2003, Astronomy and Astrophysics, 398
Kato, K., Masao, M., & Ogiya, G. 2015, IAU General Assembly
Klypin, A., Kravtsov, A.V., Bullock, J.S., & Primack, J.R. 2001, Astrophysical Journal, 554
Klypin, A., Kravtsov, A.V., Valenzuela, O., & Prada, F. 1999, Astrophysical Journal, 522
Kuzio de Naray, R., Arsenault, C.A., Spekkens, K., et al. 2012, Monthly Notices of the Royal Astronomical Society, 427
Kuzio de Naray, R., McGaugh, S. S., & de Blok, W. J. G. 2008, Astrophysical Journal, 676
Kuzio de Naray, R., McGaugh, S. S., de Blok, W. J. G., & Bosma, A. 2006, Astrophysical Journal, 165
Lees, J. F., Knapp, G. R., Rupen, M. P., & Phillips, T. G. 1991, Astrophysical Journal, 379
Leroy, A.K., Bolatto, A.D., Simon, J.D., & Blitz, L. 2005, Astrophysical Journal, 625
Leroy, A.K., Walter, F., Bigiel, F., et al. 2009, Astronomical Journal, 137
Macciò, A.V., Stinson, G., Brook, C. B., et al. 2012, Astrophysical Journal, 744
Markevitch, M., Gonzalez, A.H., Clowe, D., et al. 2003, Astrophysical Journal, 606
Mateo, M. L. 1998, Annual Review of Astronomy and Astrophysics, 36
Matthews, L. D., Gao, Y., Uson, J. M., & Combes, F. 2005, Astronomical Journal, 129
Matuszewski, M., Chang, D., Crabill, R.M., et al. 2010, Proceedings of the SPIE, 7735
McGaugh, S. S., Rubin, V. C., & de Blok, W. J. G. 2001, Astronomical Journal, 122
Moore, B. 1994, Nature, 370
Navarro, J. F., Frenk, C. S., & White, S. D. M. 1996, Astrophysical Journal, 462
Newman, A. B., Treu, T., Ellis, R. S., & Sand, D. J. 2013a, Astrophysical Journal, 765
Newman, A. B., Treu, T., Ellis, R. S., et al. 2013b, Astrophysical Journal, 765
Obreschkow, D., & Rawlings, S. 2009, Monthly Notices of the Royal Astronomical Society, 394
Oh, S.-H., de Blok, W. J. G., Brinks, E., Walter, F., & Kennicutt, R. C., Jr. 2011, Astronomical Journal, 141
Oh, S.-H., Hunter, D.A., Brinks, E., et al. 2015, Astronomical Journal, 149

Ott, J., Stilp, A. M., Warren, S. R., et al. 2012, Astronomy and Astrophysics, 144
Pawlowski, M.S., Famaey, B., Jerjen, H., et al. 2014, Monthly Notices of the Royal Astronomical Society, 442
Peter, A.H. G., Rocha, M., Bullock, J.S., & Kaplinghat, M. 2013, Monthly Notices of the Royal Astronomical Society, 430
Pontzen, A., & Governato, F. 2012, Monthly Notices of the Royal Astronomical Society, 421
Reese, A.S., William, T.B., Sellwood, J.A., Barnes, E.I., & Powell, B.A. 2007, Astronomical Journal, 133
Rocha, M., Peter, A.H.G., Bullock, J.S., et al. 2013, Monthly Notices of the Royal Astronomical Society, 430
Rubin, V. C., Thonnard, N., & Ford, W. K., Jr. 1978, Astrophysical Journal, 225
Sage, L.J. 1993, Astronomy and Astrophysics, 100
Sauty, S., Casoli, F., Boselli, A., et al. 2003, Astronomy and Astrophysics, 411
Schoenmakers, R.H.M., Franx, M., & de Zeeuw, P.T. 1997, Monthly Notices of the Royal Astronomical Society, 292
Sellwood, J.A., & Sanchez, R.Z. 2010, Monthly Notices of the Royal Astronomical Society, 404
Silk, J. 2017, Astrophysical Journal Letters, 839
Simon, J.D., Bolatto, A.D., Leroy, A.K., & Blitz, L. 2003, Astrophysical Journal, 596
—. 2005, Astrophysical Journal, 621
Spekkens, K., & Sellwood, J.A. 2007, Astrophysical Journal, 664
Strong, A.W., & Mattox, J.R. 1996, Astronomy and Astrophysics, 308
Swaters, R.A., Madore, B.F., van den Bosch, F.C., & Balcells, M. 2003a, Astrophysical Journal, 583
Swaters, R.A., van Albada, T.S., van der Hulst, J.M., & Sancisi, R. 2002, Astronomy and Astrophysics, 390
Swaters, R.A., Verheijen, M.A.W., Bershady, M.A., & Andersen, D.R. 2003b, Astrophysical Journal, 587
Tenorio-Tagle, G. 1979, Astronomy and Astrophysics, 71
Tonini, C., Lapi, A., & Salucci, P. 2006, Astrophysical Journal, 649
Trujillo-Gomez, S., Klypin, A., Colin, P., et al. 2015, Monthly Notices of the Royal Astronomical Society, 446
van den Bosch, F.C., & Swaters, R.A. 2001, Monthly Notices of the Royal Astronomical Society, 325
Vogelsberger, M., Zavala, J., Cyr-Racine, F.-Y., et al. 2016, Monthly Notices of the Royal Astronomical Society, 460
Walter, F., Brinks, E., de Blok, W. J. G., et al. 2008, Astronomical Journal, 136
Weinberg, M.D., & Katz, N. 2007a, Monthly Notices of the Royal Astronomical Society, 375
—. 2007b, Monthly Notices of the Royal Astronomical Society, 375
Welch, G.A., & Sage, L.J. 2003, Astrophysical Journal, 584
Wright, E., Eisenhardt, P., Mainzer, A., et al. 2010, Astronomical Journal, 140
Young, J. S., Xie, S., Tacconi, L., et al. 1995, Astrophysical Journal, 98